EFFECTS OF NEUTRON IRRADIATION ON THE MICROSTRUCTURE AND MECHANICAL PROPERTIES OF THE HEAT AFFECTED ZONE OF STAINLESS STEEL WELDS

THÈSE N^O 3326 (2005)

PRÉSENTÉE À LA FACULTÉ SCIENCES DE BASE

CRPP Association Euratom

SECTION DE PHYSIQUE

ÉCOLE POLYTECHNIQUE FÉDÉRALE DE LAUSANNE

POUR L'OBTENTION DU GRADE DE DOCTEUR ÈS SCIENCES

PAR

Raluca STOENESCU

ingénieur mécanicien diplômé de l'Université polytechnique de Bucarest, Roumanie
et de nationalité roumaine

acceptée sur proposition du jury:

Dr N. Baluc, directrice de thèse
Dr D. Gavillet, rapporteur
Prof. A. Mortensen, rapporteur
Prof. M. Q. Tran, rapporteur
Dr. B. van der Schaaf, rapporteur

Lausanne, EPFL
2005

Abstract

The effects of neutron irradiation on austenitic stainless steels, usually used for the manufacturing of internal elements of nuclear reactors (e.g. the core shrouds), are the alteration of the microchemistry and the microstructure, and, as a consequence, of the mechanical properties. The present study is aimed at extending knowledge upon the impact of neutron-irradiation on the heat affected zone (HAZ) of welded materials, which was influenced by the thermal cycles upon fusion welding.

Two types of austenitic stainless steels welds, AISI 304 and AISI 347, referred to as test materials, have been produced by FRAMATOME ANP (Germany) using a welding procedure that was a compromise between the conditions applied to real reactor components and the restrictions concerning dimensions and the allowable deformation imposed by this research project. The welded test materials have been irradiated with neutrons in a High Flux Reactor in Petten (The Netherlands) at a temperature of around 573 K (approximate operating temperature of light water reactors) to 0.3 dpa and 1 dpa. A welded AISI 304 type austenitic stainless steel, so-called in-service material, originating from a decommissioned light water reactor in Mol (Belgium) which had operated for 25 years and having accumulated different dose levels, to a maximum of 0.3 dpa, was also studied.

The effect of neutron irradiation on the HAZ was evaluated by studying the microstructure and mechanical properties before and after irradiation. The characterisation of the microstructure was made by optical microscopy, scanning electron microscopy and transmission electron microscopy (TEM). The mechanical properties were determined by performing microhardness measurements and tensile testing. Tensile tests were conducted on small flat specimens at two deformation temperatures: room temperature and about 573 K.

For the unirradiated and very low dose irradiated materials, optical microscopy observations showed that the grain size is larger in the HAZ as compared to the base material (BM) due to the high temperatures reached during welding. The HAZ extends over around 600 μm on both sides of the weld. TEM observations showed that the HAZ contains a higher dislocation density than the BM due to the thermal cycles upon welding. The HAZ also contains small ferrite islands dispersed in the austenite matrix.

Concerning the irradiated materials, TEM observations have shown that the austenitic matrix contains a large number of irradiation-induced defects. These defects are black dots, too small to be identified in TEM, and Frank loops, which can be either of vacancy or of interstitial type. In the in-service material the irradiation-induced defect density was found to be higher in the HAZ as compared to the BM. The higher defect density in the HAZ may be due to the higher grain size in the HAZ as compared to the BM, leaving less sinks (e.g. grain boundaries) for irradiation-induced defects annihilation. No irradiation-induced defects have been observed by TEM in the bcc ferritic interphase, which confirms that the irradiation-induced defects accumulate at a smaller rate in bcc materials than in fcc ones.

Following tensile testing at room temperature the microstructure of unirradiated materials contains mainly twins. Following tensile testing at high temperature, the microstructure appears composed of dislocation cells. These results are independent on the specimen position from the fusion line. In the case of irradiated materials the

deformation microstructure contains mainly stacking faults and twins. It seems to present no significant dependence on the material type, the irradiation dose and the test temperature.

Tensile tests performed on all irradiated materials revealed an increase in the yield strength (radiation hardening) and a decrease of the uniform elongation (loss of ductility), at both deformation temperatures. Radiation hardening presents lower values in the HAZ as compared to the BM. The loss of ductility is higher in the HAZ as compared to the BM. Radiation hardening was analysed using the dispersed obstacle hardening model. It was found that the measured radiation hardening cannot be explained solely by the presence of the irradiation-induced defects observed in TEM. Smaller irradiation-induced features (not resolvable in TEM) apparently also contribute to radiation hardening.

In conclusion, the HAZ presents a resistance to neutron-irradiation that is similar to the one of the BM, in terms of accumulation of irradiation-induced defects (black dots and Frank loops) and changes in mechanical properties (hardening and loss of ductility). The degradation of the mechanical properties of the HAZ clearly results from irradiation and not from welding. It seems that the threshold dose for peculiar deterioration of the HAZ, in terms of apparition of cracks or microcracks, was not reached in the present study.

Résumé

Les effets d'une irradiation neutronique sur les aciers austénitiques, habituellement utilisés pour la fabrication des composants internes des réacteurs nucléaires (telle l'enveloppe entourant le coeur), comprennent généralement une altération de la composition chimique à l'échelle microscopique ainsi que des modifications de la microstructure et, par voie de conséquence, des propriétés mécaniques. Cette étude a pour but d'étendre les connaissances actuelles dans le domaine des effets d'irradiation neutronique sur la zone de matériau entourant des joints en acier austénitique, fabriqués par un procédé de soudage par fusion, zone affectée par les hautes températures et cycles thermiques reliés à l'opération de soudage et habituellement dénommée 'zone affectée par la chaleur'.

Deux types de joints composés d'acier austénitique, soit l'AISI 304 soit l'AISI 347 (matériaux tests), ont été fabriqués par la compagnie FRAMATOME ANP (Allemagne) en utilisant une technique de soudage constituant un compromis entre les conditions réelles appliquées aux composants des réacteurs et les restrictions imposées par cette étude quant à la taille des pièces à fabriquer et la déformation maximale engendrée par le soudage. Les matériaux tests ont ensuite été irradiés avec des neutrons au sein d'un réacteur expérimental à flux élevé localisé à Petten (Hollande), à environ 573 K (température approximative d'opération des réacteurs à eau légère) et deux différentes doses atteignant respectivement 0.3 et 1 dpa. Par ailleurs, un joint fait d'acier austénitique de type 304 (matériau de service), provenant de la désaffectation d'un réacteur expérimental à eau légère situé à Mol (Belgique), ayant fonctionné durant 25 ans et accumulé une dose maximale de 0.3 dpa, a également été l'objet de cette étude.

Les effets d'irradiation neutronique sur les différentes zones affectées par la chaleur, provenant des différents joints décrits ci-dessus, ont été évalués en étudiant la microstructure et les propriétés mécaniques, avant et après irradiation. La microstructure a été caractérisée par le biais d'observations en microscopie optique et en microscopie électronique à balayage et en transmission. Les propriétés mécaniques ont été caractérisées en effectuant des mesures de microdureté et des essais de déformation en traction. Ces derniers ont été réalisés à température ambiante ainsi qu'à 573 K, en utilisant des petits échantillons plats de traction.

Concernant les matériaux non irradiés et très faiblement irradiés, les observations en microscopie optique ont montré que, quel que soit le matériau, la zone affectée par la chaleur s'étend sur une distance d'environ 600 microns de part et d'autre des joints et que la taille des grains est plus élevée dans la zone affectée par la chaleur que dans le matériau de base, en raison des températures élevées atteintes durant l'opération de soudage. Les observations en microscopie électronique en transmission ont montré que la densité de dislocations est plus élevée dans la zone affectée par la chaleur que dans le matériau de base, en raison des cycles thermiques effectués durant l'opération de soudage. La zone affectée par la chaleur contient également une certaine fraction volumique d'îlots ferritiques de structure cubique centrée, dispersés dans la matrice austénitique de structure cubique à faces centrées.

Concernant les matériaux irradiés, les observations en microscopie électronique en transmission ont montré que la matrice austénitique contient un grand nombre de défauts. Ces défauts sont des spots d'intensité ('black dots'), non identifiables en microscopie électronique en transmission car étant trop petits, et des boucles de dislocation du type boucles de Frank, ces dernières pouvant être de nature lacunaire ou interstitielle. La densité de défauts produits par l'irradiation est généralement plus élevée dans la zone affectée par la chaleur que dans le matériau de base. Ce phénomène résulte sans doute du fait que, la zone affectée par la chaleur étant composée de grains de taille plus grande que le matériau de base, elle contient donc moins de joints de grains pouvant opérer comme puits d'annihilation pour les défauts créés par l'irradiation. Aucun défaut dû à l'irradiation n'a été observé au sein des îlots de ferrite, le taux d'accumulation des défauts d'irradiation étant bien moindre dans les structures cubiques centrées que dans les structures cubiques à faces centrées.

Après déformation en traction à température ambiante, la microstructure des matériaux non irradiés contient principalement des macles. Après déformation à 573 K, la microstructure apparaît composée de cellules de dislocations. Ces résultats sont indépendants de la position de l'échantillon analysé par rapport à la ligne de fusion. La microstructure de déformation des matériaux irradiés comprend des macles et des fautes d'empilement et semble indépendante du type du matériau, de la dose accumulée et de la température de déformation.

Dans tous les cas, il a été observé que l'irradiation neutronique engendre un durcissement important des matériaux étudiés, qui augmente avec la dose accumulée, ainsi qu'une perte de ductilité. Le durcissement est moins important dans la zone affectée par la chaleur que dans le matériau de base. La perte de ductilité semble moins importante dans la zone affectée par la chaleur que dans le matériau de base. Le phénomène de durcissement fut analysé sur la base du modèle de durcissement par une distribution d'obstacles dispersés. Il a été conclu que le durcissement mis en évidence dans cette étude ne peut être expliqué par la seule présence des défauts d'irradiation observés en microscopie électronique en transmission. Il semble qu'une quantité non négligeable de très petits défauts créés par l'irradiation neutronique, dont la taille n'est pas résolvable en microscopie électronique en transmission, contribue également au phénomène de durcissement des aciers austénitiques sous irradiation neutronique.

En conclusion, la zone affectée par la chaleur présente une résistance à l'irradiation neutronique similaire à celle du matériau de base, en termes de dégâts d'irradiation ('black dots', boucles de dislocation de type Frank) et d'effets sur les propriétés mécaniques (durcissement, perte de ductilité). La dégradation des propriétés mécaniques de la 'zone affectée par la chaleur' résulte visiblement de l'irradiation neutronique et non pas de l'opération de soudage. Il semblerait que la dose critique à partir de laquelle on observe habituellement une dégradation particulière de la 'zone affectée par la chaleur, en termes d'apparition de fissures ou microfissures, n'ait pas été atteinte dans le cadre de cette étude.

CONTENTS

CHAPTER 4   DISCUSSION

Introduction

Nuclear power provides a steady energy at low prices. Because of their advanced design and sophisticated containment structures, the nuclear power plants have a low impact on environment and they produce the largest amount of electricity in relation to a minimal environmental impact. The safety of nuclear power plants is permanently under investigation in order to avoid failure of plants components.

For the fabrication of some internal components such as core shrouds of light water reactors, welded austenitic stainless steels are used. The core shrouds of the nuclear reactors are subjected to radiation, heat, as the operating temperature is 288°C, stresses, and corrosive environment. The failure of the welded reactor components, usually made of AISI 304, AISI 304L, and/or AISI 347 types of austenitic stainless steels, has been observed in the past several years. Examinations of core shrouds have revealed the presence of circumferential cracks in the heat affected zone of the welds. Although the behaviour of austenitic stainless steels as base materials has been thoroughly investigated, studies of weld metals and heat affected zones are scarce, in this context.

It is known that welding induces residual stresses in the material, which can be as high as the yield strength of the material. In fusion welding, a region of the heat affected zone is heated within the carbide precipitation temperature range, so that intergranular carbide precipitation occurs. As a consequence of welding, the grains are enriched in chromium and depleted in nickel.

The basic effect of irradiation on materials is the alteration of the microchemistry, the microstructure and, as a consequence, of the mechanical properties. Irradiation induces depletion in chromium, manganese, and molybdenum at the grain boundaries and enrichment in nickel and silicon. It also produces structure defects and defect clusters in the grain matrix and therefore alters the dislocation loop density and dislocation mobility, leading to radiation-induced hardening. The irradiation-induced changes in microstructure can also lead to localised stress relaxation.

The goal of this study is to better understand the effects of welding cycles and neutron irradiation on the microstructure and mechanical properties of heat affected zones of two types of austenitic stainless steels. This work is part of a European project, INTERWELD, which will be described in the next paragraph.

This thesis is organised in four chapters:

- The first chapter reviews the literature data on welded and irradiated austenitic stainless steels.

- The second chapter describes the materials, the irradiation conditions and the experimental methods used in the present investigation.

- The microstructure and mechanical properties of the heat affected zones and base materials, before and after irradiation are reported in the third chapter.

- Finally, in the fourth chapter the obtained results are discussed and compared with the literature data. A correlation between the microstructure and the mechanical properties, before and after neutron irradiation, is made.

The INTERWELD Project

Overview of the project

The present study is part of a European project, namely INTERWELD (Irradiation effects on the microstructure, mechanical properties and residual stresses in the heat affected zones of austenitic stainless steel welds). The aim of the project is to better understand the irradiation-induced changes in the heat affected zones of welded austenitic stainless steels relevant for boiling water reactor components that show intergranular cracking. This main objective can be achieved by determining relations between the development of weld residual stresses, microstructure, microchemical and mechanical properties. The project is realised between six different partners, with different contributions.

Test welds from AISI 304 and AISI 347 stainless steels have been realised by FRAMATOME ANP, Germany. Two plates of each material were joined together by fusion welding using gas tungsten arc welding process for the root pass and manual shielded arc welding process for the subsequent passes, $2 – 5$ passes (see § 2.1.1.1). The chosen welding procedure was a compromise between the conditions applied to real boiling water reactor components and the restrictions concerning the dimensions and the allowable deformation given by the research project. The welded test materials have been irradiated with neutrons in NRG Petten, the Netherlands to 0.3 dpa and 1 dpa at a temperature of 300°C. An AISI 304 type austenitic stainless steel, so-called in-service material, originating from a decommissioned water reactor in Mol, Belgium, was provided by SCK-CEN. The reactor was in operation for 25 years at a temperature of 300°C and the studied material had accumulated different dose levels, with a maximum of 0.3 dpa (see § 2.1.2).

In order to study the effects of the welding process and the neutron irradiation-induced changes, the materials have been studied before and after irradiation by means of:
- small specimen tensile testing (PSI, Switzerland)
- microstructure observations (PSI, Switzerland, CIEMAT, Spain)
- sensitisation degree (FRAMATOME ANP, Germany)
- slow strain rate tensile tests (CIEMAT and FRAMATOME ANP for the test weld materials and in SCK-CEN for the in-service material)
- weld residual stresses measurements (PSI, FRAMATOME ANP, JRC, the Netherlands)

Motivation of the project

Internal components and structure elements of boiling water reactors, such as core shrouds, show stress corrosion cracking after several years of plant operation. The replacement of the defect shrouds is feasible, but certainly at a high cost level from both replacement operation and prolonged outage. Avoiding the initiation and propagation of cracks in the shrouds is thus an activity that serves the economy of

the existing plants. At the same time the design and manufacturing of core shrouds for new reactors will benefit from the insight into crack formation and growth.

A core shroud is a welded austenitic stainless steel cylinder located inside the reactor pressure vessel that directs cooling water around the nuclear fuel. It is well known that the irradiation-assisted stress corrosion cracking phenomenon (IASCC) can occur in the welded structures of reactor pressure vessels [1 – 4]. Most of the core shroud cracking incidents have been observed in the heat affected zones of the welded structure.

IASCC describes a phenomenon in which a combination of irradiation, stresses and corrosive environment contributes to the material degradation. IASCC depends on both material characteristics and water chemistry, and it was observed to occur above doses between 0.7 dpa (in boiling water reactors oxygenated water conditions) and 7 dpa (for boiling water reactors hydrogen water chemistry and pressurised water reactor conditions) [5]. Radiation-induced segregation, radiation-induced microstructure and radiation hardening contribute to the IASCC mechanism. The specific irradiation-induced microstructural and microchemical changes that promote IASCC are still largely unknown.

The objective of INTERWELD project is to better understand the neutron radiation induced changes in the heat affected zones of welded components that promote intergranular cracking. The evolution of weld residual stresses, microstructure, microchemistry and mechanical properties under irradiation and the stress corrosion cracking behaviour of the materials have been investigated.

Experimental results of the project

Residual stress measurements

The residual stresses induced by the welding process have been measured on the unirradiated and irradiated materials, using destructive (the ring-core technique) and non-destructive (neutron and X-ray diffraction) methods. Unirradiated welded plates were examined by FRAMATOME ANP using the ring-core technique to determine the depth profiles of the local weld residual stresses and the X-ray diffraction method. At the PSI the neutron diffraction technique has been applied, using the POLDI (Pulse Over-Lap Diffraction) facility. A neutron diffraction method was also applied at JRC to determine the residual stresses in the unirradiated and irradiated test weld materials.

Both destructive and non-destructive measurements performed by FRAMATOME ANP showed the existence of residual stresses due to welding in both AISI 304 and AISI 347. The level of residual stresses in the HAZ is higher in AISI 304 as compared to AISI 347 [6].

Two plates of unirradiated AISI 304 and AISI 347 have been analysed using the POLDI facility at the PSI. The residual stresses measured in the case of AISI 304 are presented in Figure 1 and the residual stresses for AISI 347 in Figure 2. The residual stresses mainly concentrate in the longitudinal direction, as it can be deduced from Figure 1. In the centre of the weld stresses as high as 350 MPa were measured at

the PSI for AISI 304 and about 200 MPa for AISI 347, in a much smaller plate. Comparison of measurements realised on different plate sizes of the same material indicates clearly that stress relaxation occurs during the cutting of the plate, as observed in Figure 2. Based on the neutron diffraction measurements it can be concluded that the welding process has generated a residual stress field characterized by tensile longitudinal stresses in and around the weld, balanced by compressive stresses further away from the weld. Cutting induces relaxation of the weld residual stresses, as it was observed in the case of AISI 347. Because small specimens were used in the present study, it can be assumed that they were free of residual stresses.
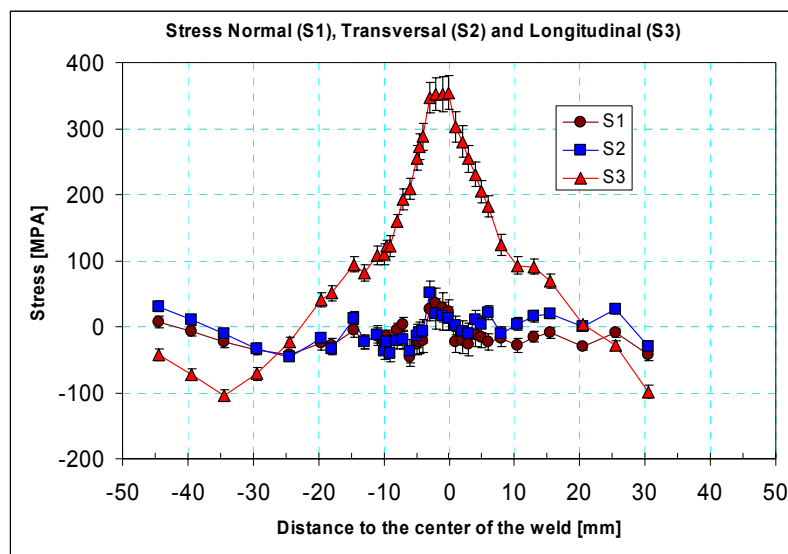

Figure 1. Mid thickness stresses variations along a line perpendicular to the weld in the unirradiated AISI 304, as measured at the PSI [6].
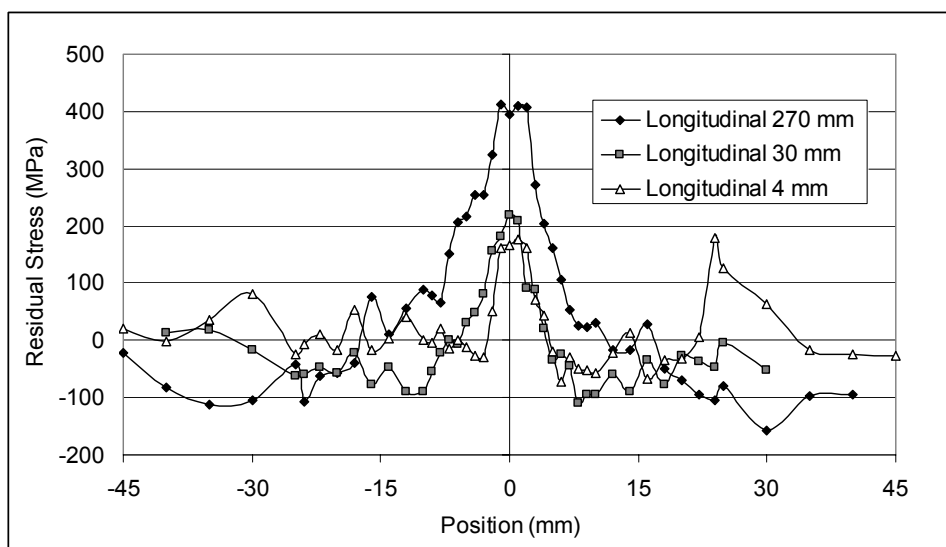

Figure 2. Stresses variations in the unirradiated AISI 347 test material, as measured at the JRC for different plate sizes [6].

Residual stress measurements have been performed by neutron diffraction at the PSI on the in-service material, on both low dose (Block A) and high dose (Block B) components. No significant residual strains or stresses were measured in the in-service material for both low dose and high dose conditions. Due to the lack of reference material (as-welded, unirradiated) it can not be concluded if the welded metal has been produced without any internal stress or if the neutron irradiation has induced stress relaxation in the welded materials. The cutting geometry of the specimens for neutron diffraction measurements could also influence the values of the residual stresses, as pointed out in Figure 2.

Determination of the sensitisation degree

The sensitisation degree of the unirradiated welded AISI 304 and AISI 347 was determined using the Double Loop Electrochemical Potentiokinetic Reactivation (DP – EPR) method at FRAMATOME ANP. DP – EPR measurements were carried out on specimens in the as-welded condition and on specimens heat treated after welding. The post welding heat treatment consisted in heating at 580°C for 4 hours, followed by furnace cooling, for AISI 347 and heating at 450°C for 4 hours, followed by furnace cooling, for AISI 304. Metallographic observations of the samples after the EPR tests do not indicate any specific grain boundary attack, for both materials, with or without post weld heat treatment. Only some minor, but not systematical, grain boundaries attack has been observed at the fusion line in the post welding heat treated AISI 347.

Auger electron spectroscopy was performed by CIEMAT on the AISI 304 and AISI 347 unirradiated as-welded specimens to determine the grain boundary microchemistry. In order to promote intergranular fracture, necessary for the grain boundary segregation studies, the samples were charged with hydrogen at 70°C for about 72 hours and fractured by tensile testing inside the Auger vacuum chamber. No significant differences in the average of alloying element concentrations (iron, chromium, nickel) were observed in the ductile areas, for both tested materials.

Slow strain rate tensile tests

In order to evaluate the susceptibility of the material to stress corrosion cracking, Slow Strain Rate Tensile Tests (SSRT) have been performed on both unirradiated and irradiated test weld materials at CIEMAT [6]. FRAMATOME ANP performed SSRT tests only on the unirradiated test weld materials. The in-service material has been characterised in terms of stress corrosion cracking behaviour by performing SSRT tests in a simulated boiling water reactor environment at SCK-CEN.

<u>Test weld materials</u>

Flat tensile samples of 1 mm thickness and 16 mm gauge length were fabricated from the welded plates of both materials. The gauge length of the tensile specimen contained the heat affected zone of the welded plate. The tests have been carried out on both unirradiated and irradiated test weld materials at 290ºC and 90 MPa, in pure water with an inlet conductivity less than 0.1 mS/cm and containing 200 ppb of

dissolved oxygen, using a flow rate of 10 l/h and a strain rate of 3.5 x 10^{-7} s^{-1}. In addition, SSRT tests were performed at the same temperature in argon gas. Comparison of results in water and in inert gas permits the assessment of the effect of environment on the IASCC susceptibility of the material. The tensile parameters have been determined from the SSRT curves recorded during the tests. The fracture surface of each specimen has been studied by scanning electron microscopy.

In spite of the welding process, no chromium carbides precipitation at the grain boundary was observed in the test weld materials. If no chromium depletion occurs in the material, no intergranular cracking is expected during testing in an oxygenated environment. According to the criteria commonly used to evaluate the behaviour of austenitic stainless steels (based on the percentage of intergranular fracture and the SSRT parameters), unirradiated and welded AISI 304 and AISI 347 do not show intergranular stress corrosion cracking in both the high temperature water with 200 ppb dissolved oxygen and the inert gas.

The SSRT curves of welded and 0.3 dpa irradiated AISI 304 and AISI 347 revealed that neutron irradiation produces in both materials a significant increase in the yield strength and ultimate tensile stress and a reduction of the total elongation. No intergranular fracture was observed in any of the irradiated material.

The report on SSRT tests on the 1 dpa irradiated materials is not yet available.

FRAMATOME ANP performed SSRT tests on small flat tensile specimens, with dimensions similar to those used at CIEMAT, on both AISI 304 and AISI 347 unirradiated test welds, with or without post weld stress relief heat treatment. The SSRT tests were performed in an oxygenated high temperature water, at 290°C, containing 200 ppb dissolved oxygen.

Only slight differences between the stress-strain curves of the tested specimens have been observed. The fractographic examinations showed predominantly ductile fracture surfaces. A small part of the fracture surface showed transgranular features. According to the literature [6] transgranular cracking is considered as an experimental artefact of SSRT tests. No feature of intergranular stress corrosion cracking was observed for the examined materials and conditions. This correlates well with the unsensitised microstructure revealed by the EPR tests.

<u>In-service material</u>

Small specimens (gauge length 12 mm, diameter 2.4 mm) containing the weld metal and the heat affected zone were prepared from both available welded in-service block materials (see § 2.1.2). Because the use of small specimens cannot guarantee that all the zones of the weld are contained inside the gauge, larger samples (gauge length 25 mm, diameter 3.6 mm), containing the weld metal, the heat affected zone and the base material, were also used for the confirmation of the results. One large specimen for each dose level was tested.

The samples were subjected to SSRT tests in a hot-cell autoclave installation with a high temperature, high pressure water circulation loop containing 200 ppb and 8 ppm dissolved oxygen. The large tensile specimens were tested in a 8 ppm dissolved oxygen water. The tensile tests were performed at a strain rate of 3 x 10^{-7} s^{-1}.

The highest dose specimens show significant irradiation induced hardening. Cracking was found strongly dependent on the test environment and occurred only at high

oxygen levels (8 ppm) for all small and large samples, irrespective on the dose and specimen location in the weld. The specimens tested in water with 8 ppm dissolved oxygen exhibit larger strength values as compared to the specimens tested in low oxygen water. It is unclear if this is due to the sampling of the material (small specimens) or to a corrosion effect (hardening by corrosion generated hydrogen).

The frequency of intergranular cracking does not depend on the sample location, although there was an apparent decrease of the frequency of intergranular stress corrosion cracking after irradiation. The location of the rupture with respect to the fusion line is actually determined by a balance between thermal sensitisation (being stronger far away from the fusion line and in the inner part of the thermal shield) and irradiation-induced hardening (which is stronger close to the fusion line, moving the rupture location in the case of medium sensitised samples).

CHAPTER 1

LITERATURE SURVEY

In this chapter nuclear fission reaction, nuclear power plants, austenitic stainless steels, welding consideration and irradiation-induced effects in austenitic stainless steel are successively reviewed, with emphasis on the irradiation-induced changes in microstructure and mechanical properties.

1.1 Nuclear fission energy concept

1.1.1 Nuclear fission reaction

Nuclear fission was discovered in 1938 by Otto Hahn and Fritz Strassmann while attempting to produce elements heavier than uranium, by bombarding uranium with neutrons [7, 8]. Later, in 1942, Enrico Fermi produced the first controlled self-sustaining fission reaction.

The fission reaction consists in splitting apart atoms. Only few natural elements are fissionable with slow neutrons (uranium-235, uranium-233 or thorium-232). Artificial heavy elements like plutonium-239 can also undergo fission under bombardment with slow neutrons. When a neutron interacts with a fissionable nucleus, the nucleus absorbs the neutron, becomes instable, and splits immediately (Figure 1.1 [9]). The result of the fission reaction is two lighter atoms, few neutrons, and a certain amount of energy. The resulting neutrons travel further and interact with other fissionable atoms, starting a chain reaction and causing a big amount of energy release in the form of gamma radiation and kinetic energy. The release of energy can be very quick, as in an atomic bomb, or controlled, the energy being captured and used for utilitarian proposes.
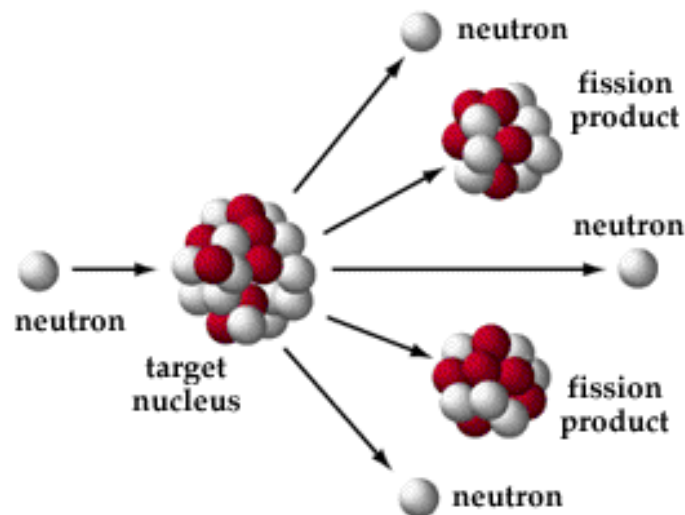

Figure 1.1. The in-chain fission reaction [9].

1.1.2 Nuclear power plants

Nuclear power plants use the energy generated by nuclear fission in a contained environment to heat up a coolant medium. This heated coolant can be used to power generators to produce electricity. The basic parts of a reactor are the core, a moderator, the control rods, a coolant, a pressure vessel and a biological shielding. The fuel (usually U^{235} enriched uranium oxide) is pressed in small pellets that are inserted into thin tubes, usually made of zirconium alloy (zircalloy) or stainless steel, to form fuel rods. The control rods are made from neutron absorbing materials like B_4C or (Cd, In, Ag). They are used to control the number of neutrons needed to sustain the chain reaction. When inserted in between the fuel rods they slow down or stop the chain reaction; pulled out, they allow speeding up the reaction again. The core of the reactor contains the nuclear fuel, the control rods and structural elements, usually made of stainless steel, that separate and contain the fuel and control rods and maintain the core geometry.

In the reactor core the uranium isotope splits (fissions) producing heat in a continuous process called a chain reaction. A coolant is used for heat removal and moderation (slowing down the neutrons). Usually light water with a very well controlled chemistry is used but liquid metal, gas or heavy water can also be used. The pressure vessel is a safety hull holding the inner pressure in the core and assuring a full containment of the nuclear fuel. Finally a biological shield (usually concrete) is used to shield the radiation field of the reactor.

Most commercial nuclear reactors use light water as coolant. The moderation is obtained by adding well controlled amounts of neutron absorber elements in the water. These reactors are called light water reactors (LWR) and they are of two types: pressurised water reactors (PWR) and boiling water reactors (BWR). PWRs operate at high pressure (about 160 bars) and temperatures (315°C). The heat is removed from the reactor by water flowing in a closed pressurised loop. The typical operating pressure for BWRs is about 70 bars, at which pressure the water boils at about 285°C. The water chemistry is very complex and slightly differs from a reactor to another one. The exact water chemistry has a great influence on the material behaviour in the reactor core. In Figure 1.2 [10] a schematic of a BWR is shown. As the fuel rods are a large source of heat, they heat the water and turn it into steam. The steam drives a steam turbine that spins a generator to produce power.

In the present study, we focused on one of the internal components of a BWR, namely the core shrouds. A core shroud is a welded austenitic stainless steel cylinder that surrounds the reactor core (see Figure 1.2). The feed water for the reactor is introduced between the reactor vessel wall and the shroud. The shroud separates the feeding water from the cooling water that flows up through the reactor core. The shroud supports the top guide that provides lateral support for the fuel assemblies and maintains core geometry during operational transients and postulated accidents to permit insertion of the control rods. It also provides the volume needed to ensure safe shutdown and rapid cooling of the core in possible accident conditions.
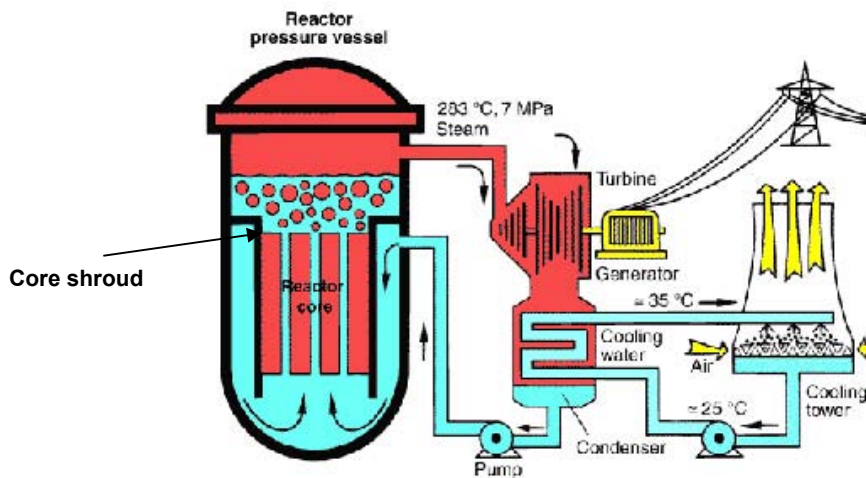
Figure 1.2. The boiling water reactor system [10].

1.2 Austenitic stainless steels

A stainless steel is essentially a low carbon steel which contains a minimum of 12 wt. % chromium. Depending on their crystalline structure stainless steels are classified as: austenitic, ferritic, martensitic, and duplex [11 – 13].

Austenitic stainless steels have, as their name says, an austenitic structure. Austenite is obtained down to the ambient temperature by adding austenising alloying elements such as nickel, manganese and nitrogen.

Austenitic stainless steels are the most commonly used materials in the chemical, petrochemical, power and nuclear industry, because of their excellent resistance to general corrosion, adequate high temperature mechanical properties, good fabricability and weldability.

They have high ductility, low yield strength and relatively high ultimate tensile strength, when compared to typical high carbon steels. They have a face centred cubic (fcc) crystal structure that provides numerous slip planes for dislocation movement and, combined with a low level of interstitial elements, gives these materials their good ductility.

However, they are susceptible to localized corrosion attacks such as pitting, stress corrosion cracking (SCC) and intergranular corrosion (IGC). SCC forms deep cracks inside the material. It is caused by the presence of chlorides in the process fluid or heating water/steam at temperatures above 50°C, when the material is subjected to tensile stresses. Significant amounts of nickel and molybdenum reduce this risk. The presence of chromium greatly improves the corrosion resistance of austenitic stainless steels through the formation of a very thin stable oxide film on the surface.

By heating these types of steels in the temperature range between 500 and 850°C, chromium carbides ($C_{23}C_6$) form. These carbides tend to nucleate preferably at the austenite grain boundaries, resulting in chromium depletion in the regions adjacent to the grain boundaries, thus affecting the mechanical properties of the steels.

1.3 Effects of welding

Welding is a widely used process for joining materials. General information on welding can be found in numerous text books or on internet [14 – 17]. Austenitic stainless steels are generally regarded as good weldable materials, with considerable tolerance for variations in welding conditions. Generally, the behaviour of a welded joint is required to be either the same or better than the one of the base material it joins. However, in practice, this objective is never achieved since the welding process itself introduces features such as slag and other inclusions, dendritic structure, residual stresses, secondary phases, defects and/or phase transformations, which degrade the corrosion, physical and mechanical properties of the welded joint, as compared to the wrought base material [18].

The SCC behaviour of the weld metal is expected to be different from that of the base material because the weld metal is actually a casting with high temperature delta ferrite retained in it, thus making it microstructurally and microchemically heterogeneous. Residual stresses are also present in the weld metal and the density of metallurgical defects such as vacancies and dislocations can be much higher than in the base material.

The presence of delta ferrite can appreciably alter both the resistance to SCC and the crack morphology of the weld metal. The resistance to SCC of the weld metal depends on the delta ferrite content, its distribution and the solidification mode.

High temperature delta ferrite is normally retained down to room temperature in the weld metal of austenitic stainless steels to prevent hot cracking. Adjusting the composition of the filler metal may help to control the amount of delta ferrite retained in the weld metal.

During the welding process, the weld thermal cycles and weld segregation may have the following effects on the surrounding material [19]:

- The peak temperatures reached in the heat-affected zone (HAZ) can be much higher than the A_{c3} temperature (the temperature at which the transformation of ferrite to austenite is completed during heating, around 723ºC). The heating rates are very high, and the times spent at high temperature are only of the order of a few seconds.
- The temperature gradient in the HAZ is very steep.
- During solidification of the weld metal, the alloying and impurity elements tend to segregate extensively in the interdendritic or intercellular regions under rapid cooling. The pickup of elements like oxygen by the molten weld pool leads to the entrapment of oxide inclusions in the solidified weld metal. These inclusions can serve as heterogeneous nucleation sites and can substantially influence the kinetics of subsequent solid state transformations. Accordingly, the weld metal transformation behaviour is quite different from that of the base

material, even if the nominal chemical composition has not been significantly changed by the welding process.

- Welding is usually carried out in several passes, and this can result in the superimposition of several different heating and cooling cycles, each of these cycles having the characteristics pointed above.

- Solidification of the weld metal is accompanied by shrinkage, and the anisothermal conditions already emphasised cause deformation. The thermal cycles are therefore acting on the metal that is simultaneously subjected to mechanical stresses at the same time.

In summary, as during fusion welding the weldment is locally heated, the temperature distribution in the weldment is not uniform and changes take place as welding progresses. The weld metal and the HAZ are subjected to a temperature substantially higher than the unaffected base material. As the molten pool solidifies and shrinks, it begins to exert stresses on the surrounding weld metal and HAZ areas. When it first solidifies, this metal is hot, relatively weak, and can exert little stress. As it cools down to ambient temperature the shrinkage of the weld metal exerts increasing stresses on the surrounding areas, which eventually reach the yield strength of the base material.

1.4 Effects of irradiation on materials

1.4.1 Radiation damage

The interaction of impinging particles with matter is a complex phenomenon that can be divided into a primary stage and a secondary stage [20 – 23]. The primary stage relates to the displacement of electrons (ionization), the displacement of atoms from their lattice site, the excitation of atoms and electrons without displacement and the transmutation of nuclei. Irradiation with energetic charged particles and gamma-rays always produces primary ionization and, depending on the irradiation conditions, usually produces primary atomic displacements. In the case of neutron irradiation, the primary process consists of atomic displacements, while ionization appears only as a secondary process. Nuclear transmutations can be produced by any of these types of radiation, but occur to an appreciable extent of impinging particles at energies above 10 MeV only when certain materials of high capture cross sections are irradiated with neutrons. Secondary effects of the interaction of radiation with matter consist of further excitation and disruption of the structure by the electrons and atoms that have been knocked on.

A fast atom moving through the matter at high energies is slowed down by numerous collisions. The collisions which the moving atom undergoes can be divided in elastic and inelastic ones. In an elastic collision the moving atom interacts with an atom of the target material, resulting in an energetic lattice atom and an irradiating particle with less energy. In an inelastic collision there is loss of energy because of the electronic excitation. Due to all these energy changes, a region of material around the track of the irradiation particles or the knocked-on atoms will be heated to a high

temperature. The region of excitation expands rapidly, and at the same time there is a drastic decrease of temperature. This phenomenon is called a thermal spike.

If the energy transferred from the irradiating particle to the lattice atom is greater than the threshold displacement energy of the later (about 25 eV in metals, according to Seitz, 1949), the atom is displaced from its lattice site. The lattice atom kicked directly by the incident particle is called the primary knock-on atom (PKA). Each displacement event leads to the formation of a Frenkel pair composed of a vacant lattice site (vacancy) and a self-interstitial atom. Nuclear transmutation of the PKA atom may also occur, resulting in the formation of impurities (hydrogen, helium or heavier elements). Depending on the type and energy of the irradiating particle, this process leads to a series of atomic displacements until the energy of the particle or the knocked atoms drop below the threshold displacement energy, or until the particle leaves the solid. In this way a so-called atomic displacement cascade takes place, resulting in a large number of displaced atoms. The atomic displacement cascades engender highly disordered regions with high energy density, which are characterised by a nucleus formed of vacancies, surrounded by a cloud of interstitials.

To calculate the number of Frenkel pairs generated by a PKA, Kinchin and Pease [24] developed the following model:

$$N_d = \begin{cases} 0, & E \prec T_d \\ 1, & T_d \prec E \prec 2 \cdot T_d \\ \dfrac{E}{2 \cdot T_d}, & E \succ 2 \cdot T_d \end{cases} \qquad (1.1)$$

where N_d is the number of Frenkel pairs generated by a PKA, T_d is the displacement energy and E is the energy of the PKA.

In other words, for PKA energies greater than the displacement energy, the atom will be displaced permanently from its lattice site, while the atoms receiving an energy smaller than their displacement energy will return to their lattice sites.

Norgett, Robinson and Torrens took into consideration the energy lost by electron excitation, Q, not capable to produce displacements, and they modified the Kinchin and Pease model [25]:

$$N_d = \frac{k \cdot (E - Q)}{2 \cdot T_d} = \frac{k \cdot E_d}{2 \cdot T_d} \qquad (1.2)$$

where E_d is the damage energy (the energy available for producing displacement), and k is the displacement efficiency ($k \cong 0.8$).

By introducing the above values in equation 1.2, one obtains the number of Frenkel pairs N_d, generated by a PKA of energy E_d:

$$N_d = \frac{0.8 \cdot E_d}{2 \cdot T_d} \qquad (1.3)$$

The NRT model [25] is generally accepted as the international standard for quantifying the number of atomic displacements per atom or dpa in irradiated materials. This unit has been established as the preferred fundamental measure of material response to irradiation exposure level, and has been accepted for a wide variety of irradiation particle types: heavy ions, protons, neutrons and electrons. The amount of radiation energy deposited in a material is defined as the accumulated dose.

During the cascade formation, and/or after it is formed, processes such as vacancy–interstitial recombination, interstitial/vacancy agglomeration, and interstitial/vacancy evaporation may occur. The cascade evolution can be described as the following: during the collisional phase of the cascade (10^{-13} s), a high concentration of defects is formed. During the cooling phase and the thermal spike (10^{-11} s) most of the defects are annihilated, leaving isolated defects and defect clusters. Short range diffusion of the mobile interstitials and vacancies within the cascade results in further recombination and clustering. Thermally activated diffusion results in long-range diffusion of the surviving, mobile defects. It can be concluded that the evolution of microstructure and microchemistry depends on the fraction of each type of defects that survive to the cascade and migrate into the lattice (freely migrating defects), as shown in Figure 1.3 [27].

The number of freely migrating defects (FMDs) depends on the irradiation particle type and energy, the temperature, the dose, and the dose rate [26]. For PKA high energies, the fraction of defects that survive the cascade quench is decreased because of the recombination that occurs in the thermal spike region. Neutrons and heavy ions produce high energy PKAs that yield in localised regions where many displacements occur, producing a high concentration of Frenkel pairs. Protons usually create PKAs of lower energy, resulting in smaller displacement spikes. Electrons create single, isolated Frenkel pairs. High energy neutrons and protons may lead to the production of impurities via nuclear transmutation reactions.

At low irradiation temperatures no thermal diffusion occurs. The number of FMDs is then equal to the number of displaced atoms that survive the cascade quench. With increasing the temperature, the number of surviving defects is smaller because of the defect recombination and defect annihilation at sinks: dislocations, grain boundaries, precipitates etc. Figure 1.4 shows a comparison of the experimental temperature dependence of the surviving defect fraction in neutron irradiated copper with results of molecular dynamics simulations [26].
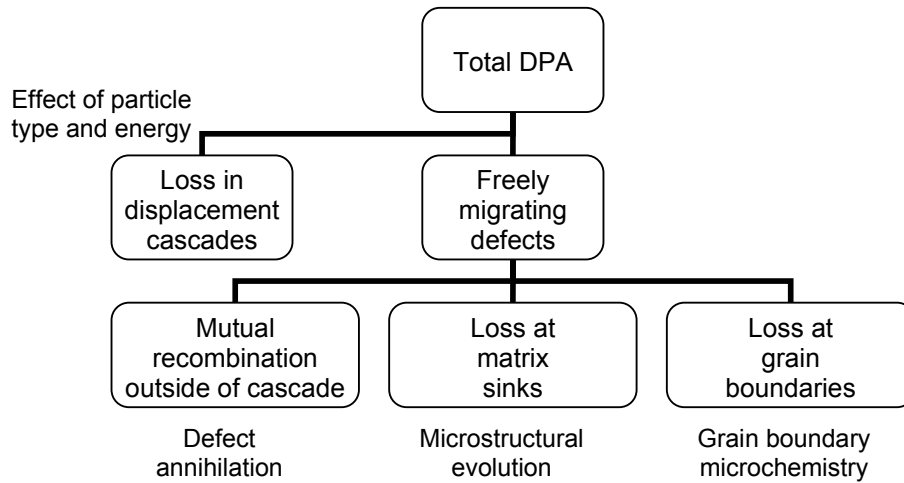
Figure 1.3. The evolution of microstructure and microchemistry due to the atoms displaced by the cascade event [27].
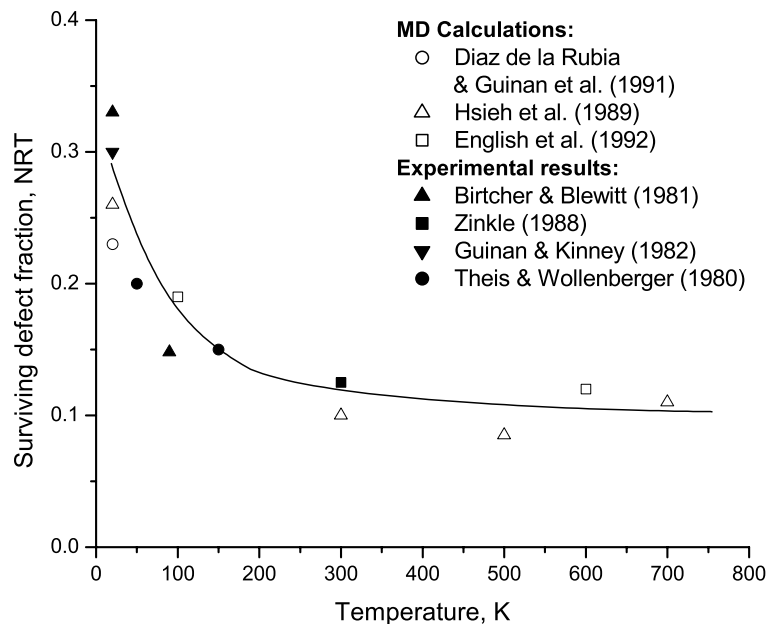

Figure 1.4. Temperature-dependence of the fraction of defects surviving the cascade quench and correlated recombination in copper irradiated with neutrons under cascade conditions [26].

1.4.2 Irradiation-induced microstructure

Although the specific damage microstructure depends on the particularities of the stainless steel type and on the irradiation conditions, typical irradiation-induced microstructural features in austenitic stainless steels are [28 – 35]:

- Black dots: very small defect clusters, smaller than 2 nm in diameter, which can not be identified in transmission electron microscopy.

- Frank loops: they are defined as faulted, interstitial or vacancy type dislocation loops. Once nucleated they grow by net self-interstitial or vacancy absorption. This growth may continue until they become unstable and unfault into perfect loops or until they interact with perfect dislocations to be incorporated directly.

- Perfect loops: they are essentially dislocation lines that are in the shape of a closed loop. They move by gliding in the slip plane in which they reside. Perfect loops can also form by the interaction of Frank loops with the dislocation network, which causes the faulted loops to "unfault" and become perfect loops. Large loops can climb and glide into lower energy configuration or annihilate with neighbouring dislocations segments of opposite type (recovery).

- Cavities (bubbles and/or voids): bubbles form by trapping gas (He) in a vacancy cluster. Helium is produced by endothermic reactions between neutrons and all the major constituents of stainless steels. Once nucleated, the bubbles grow by a combination of He and net vacancy absorption to maintain a mechanical equilibrium between their internal pressure and the sintering stress. It is believed that beyond a certain critical radius, He bubbles become unstable and grow as voids by net vacancy absorption without the need to maintain mechanical equilibrium.

- Precipitates (metal carbides): a variety of second phases may form as a result from thermally-induced precipitation and radiation-induced segregation. These include MC, M_6C and $M_{23}C_6$ carbides, Ni_3Si, Fe_2Mo (Laves), and $Ti_6Ni_{16}Si_7$ phases. Precipitation depends strongly on the material composition and irradiation environment, and it is believed to occur at temperatures higher than 400°C.

Anyway, as previously mentioned, the population of defects is strongly influenced by the type and energy of the impinging particles, the irradiation temperature, the accumulated dose and the dose rate.

At low neutron irradiation temperature (50 – 300°C) and doses around 10 dpa, the irradiation-induced defects in austenitic stainless steels are small, faulted loops of interstitial type. At temperatures above 300°C, the microstructure contains larger dislocation loops, networks of dislocations, cavities, and various types of precipitates. Helium bubbles have been observed for doses between 7 and 56 dpa, at temperatures between 300 and 330°C. Figure 1.5 shows the type of irradiation-induced defects observed in 300-series stainless steels as a function of the irradiation dose and temperature [27]. The dislocation microstructure in the low temperature regime, characteristic of the irradiation conditions in LWRs and BWRs, is dominated by "black dots" (about 2 – 3 nm in diameter) and faulted loops, lying in the {111} planes, with a mean diameter of 7 nm.

At a certain given temperature, the interstitials may be highly mobile and able to form loops, while the vacancies are less mobile. Interstitial loops increase in size with dose, as a higher number of interstitials are absorbed than vacancies. With increasing dose, vacancy clusters can form. If vacancies and interstitials are absorbed by interstitial loops at the same rate, growth of existing loops ceases. The saturation is achieved for a quite small dose ($\sim 3 - 4$ dpa). In Figure 1.6 the density and mean size of interstitial loops in irradiated 304 and 347 stainless steels is reported as a function of dose [27].

Certain alloying or impurity elements can refine the dislocation microstructure resulting from low-temperature irradiations. Phosphorus, titanium and niobium increase the interstitial loop density and decrease the loop size. In conjunction with carbon, these effects are enhanced to a greater extent. Silicon promotes loop nucleation in alloys without molybdenum (as molybdenum traps silicon atoms and prevents them from binding with interstitials).
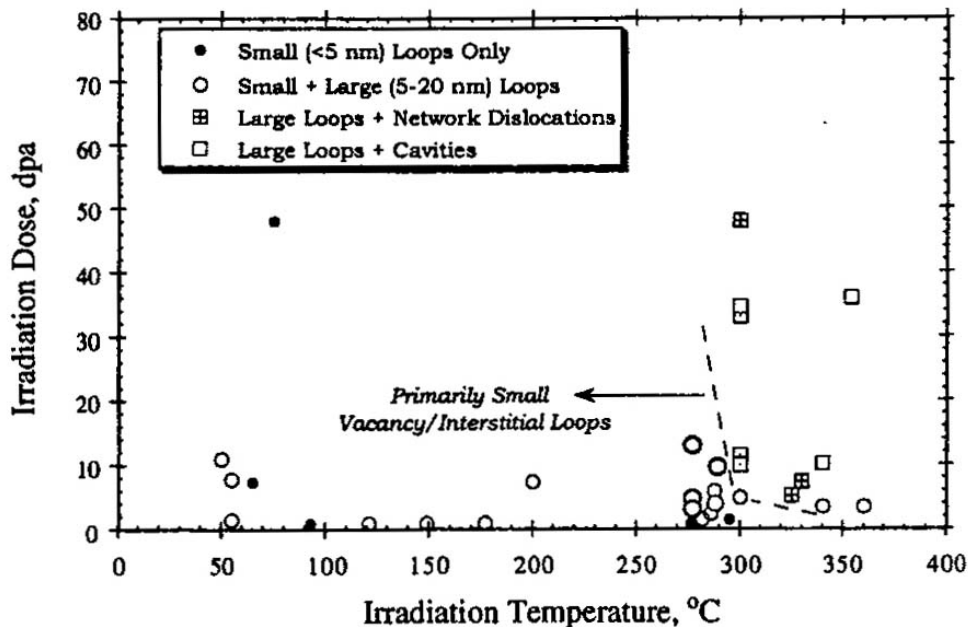
Figure 1.5. The neutron irradiation defect structure in 300-series stainless steels as a function of irradiation dose and temperature [27].
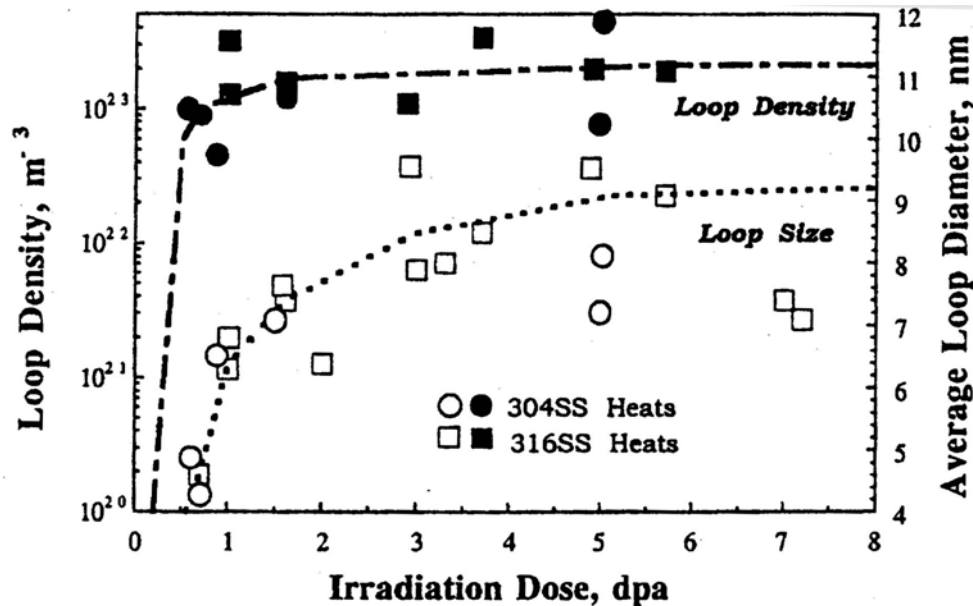
Figure 1.6. The density and mean size of interstitial loops in neutron irradiated 304 and 316 stainless steels as a function of dose [27].

1.4.3 Irradiation-induced microchemistry

In metals and alloys subjected to irradiation, the diffusion of irradiation-induced point defects to sinks (grain boundaries, dislocations, and free surfaces) can lead to a gradual depletion or enrichment of alloy components in the vicinity of sinks. This phenomenon is known as radiation-induced segregation (RIS) [27, 36].

Two mechanisms are responsible for the changes in local concentration: the inverse Kirkendall segregation effect and the interstitial association segregation (Figure 1.7) [27]. Both phenomena may occur concurrently, but one mechanism will dominate for a specific alloy composition.

The interstitial association segregation means that the self-interstitial atoms generated by irradiation create a local deformation of the lattice when small-size elements (minor alloying elements or impurity atoms like sulphur, phosphorus or silicon) are attracted to sinks. The oversized solutes are then depleted at grain boundaries.

The Kirkendall segregation effect is characterized by a net flux of vacancies across a marker plane resulting from the creation of a composition gradient in a metal having a uniform vacancy distribution. The inverse Kirkendall effect is characterized by a net flux of solute and solvent atoms across a marker plane, resulting from the formation of a gradient of vacancies in a metal having a homogeneous composition. Depletion or segregation at sinks of major alloying elements depends on the relative diffusion coefficients of vacancies and interstitials.

For binary alloys, Wiedersich et al. [37] have derived the following relation to explain the redistribution of alloying elements near the sinks:

$$\nabla C_A = \frac{D_I^B \cdot D_I^A}{\alpha \cdot \left(D_I^B \cdot D_A^{IRR} + D_I^A \cdot D_B^{IRR} \right)} \cdot \left(\frac{D_A^V}{D_B^V} - \frac{D_A^I}{D_B^I} \right) \cdot \nabla C_V \qquad (1.4)$$

where $D_A^{V,I}, D_B^{V,I}$ are the partial diffusion coefficients of a vacancy (V) or an interstitial (I) diffusing via A or B atom exchanges, D_A^{IRR}, D_B^{IRR} are the total irradiation-enhanced diffusion coefficients for A and B atoms, and α is a thermodynamic factor.

When the second term between brackets is positive, then the A atoms diffuse via an interstitial mechanism, and the A component will enrich at the sinks. When this term is negative, the component A will deplete at the sinks.
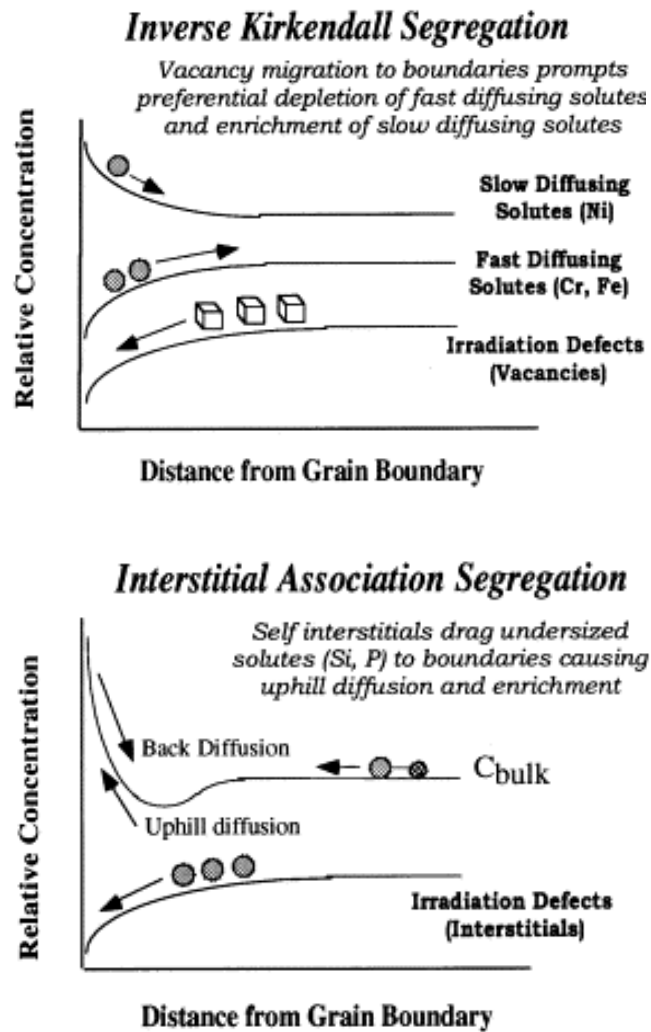
Figure 1.7. Defect flow and sink composition dependence on the mechanism of radiation-induced segregation [27].

Slow diffusion elements like nickel, silicon, and phosphorous are believed to migrate mainly by interstitial mechanisms and are enriched near sinks, while some other elements such as chromium, manganese, and molybdenum exchange more rapidly with vacancies and are consequently depleted near sinks. Iron can either deplete or enrich, depending on the magnitude of the diffusion coefficient relative to the other solutes. Other undersized solutes, such as sulphur, carbon, nitrogen, boron, should also segregate, but this was not established yet. Helium produced at high temperatures by nuclear transmutation can also segregate near or at the grain boundaries, at high temperatures.

As vacancies and interstitials are produced as Frenkel pairs, the flux of each species to the grain boundaries is similar in magnitude. Irradiation variables such as the temperature, the dose, and the dose rate are the primary factors influencing the RIS. Figure 1.8 shows the influence of irradiation temperature and dose rate on the occurrence of RIS phenomenon for different types of irradiation particles. At low temperatures, slow vacancy migration and emission lead to high probability of recombination of the point defects, preventing RIS to occur. At high temperatures the RIS is eliminated because of the high mobility of the defects, which recombine by back diffusion. The segregation level reaches a maximum at intermediate temperatures. For a given dose, higher dose rates lead to a greater recombination of defects, hence to lower segregation. At higher temperatures higher dose rates are needed to oppose the effect of back diffusion. At lower temperatures, where the vacancy mobility is restricted and recombination is high, lower dose rates are more effective in causing RIS.
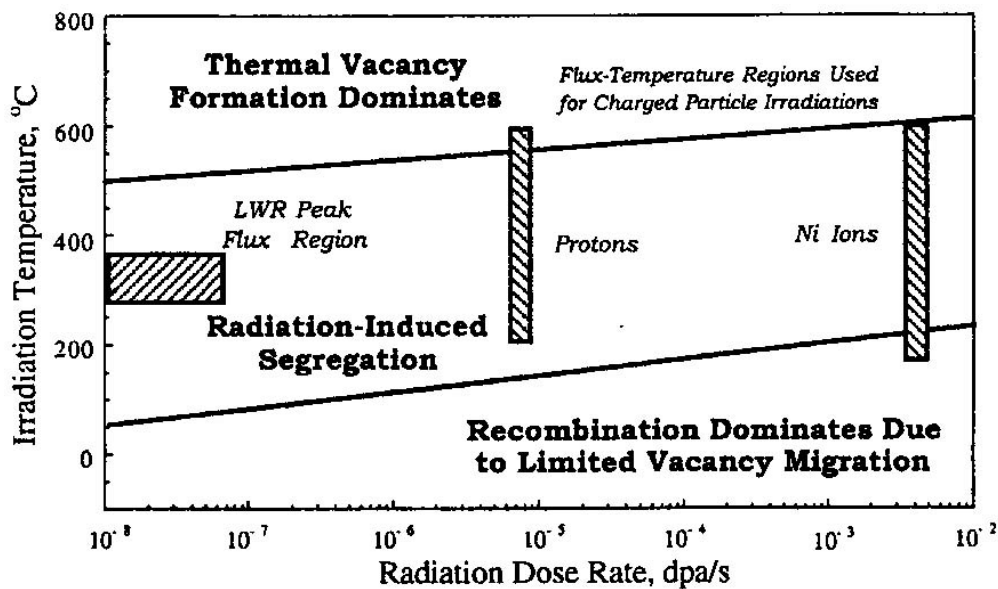

Figure 1.8. Effects of irradiation temperature and dose rate on the occurrence of RIS in austenitic stainless steels, for different types of particles [27].

Quantitative analyses of the segregation profiles of constituents in steels near the grain boundaries have been reported. As composition variations at grain boundaries take place in a narrow range of few nanometres, experimental methods with high resolution are required. This can be achieved by using a high-resolution field-

emission-gun transmission electron microscope (FEGTEM) equipped with an energy dispersed X-ray spectroscope. Experimental measurements revealed depletion in chromium, concurrently with enrichment in nickel and iron (Figure 1.9), at grain boundaries. It has been observed that at 300°C chromium and iron are depleted by 5 to 10 wt% with respect to the bulk concentration, whereas nickel is enriched up to about 30 wt% with respect to the bulk concentration, depending on the irradiation temperature and the accumulated dose.
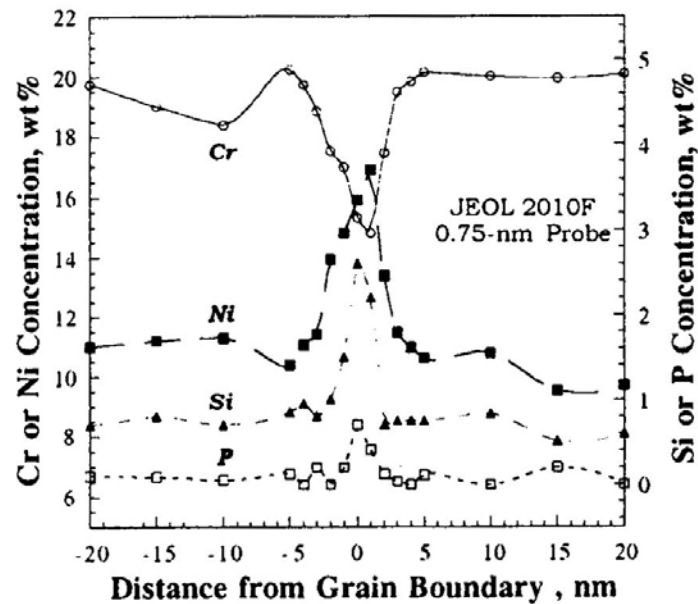

Figure 1.9. Composition profiles measured across a grain boundary in a neutron irradiated 300-series stainless steel [27].

Silicon and Phosphorus are the most common minor elements found to be enriched at grain boundaries in neutron-irradiated stainless steels. Molybdenum shows significant depletion, by more than 50%, after irradiation to about 3 dpa. Manganese is a difficult element to measure quantitatively in neutron-irradiated stainless steels, but, nevertheless, it seems to present depletion at sinks.

1.4.4 Irradiation-induced mechanical properties

It is well known and accepted that the changes in mechanical properties of neutron-irradiated austenitic stainless steels are the direct result of the damage microstructure [29, 32, 38 – 40]. Mechanical properties of interest include tensile strength, work hardening, ductility, fracture toughness, creep and fatigue resistance. Numerous studies show an increase in the yield strength and a decrease of the uniform elongation in tensile tests, as the irradiation dose is increased. The ultimate tensile strength also increases, but to a lower extent. The data show that the largest yield stress is obtained for irradiation and test temperatures of about 573 K. The dose to achieve this peak value generally decreases with increasing irradiation/test

temperature and reaches a minimum for irradiation and test temperatures in the vicinity of 573 K.

The irradiation-induced change in yield strength is usually assumed to be due to the formation of faulted interstitial loops, since they are the dominant microstructural strengtheners present in materials irradiated in PWR and BWR conditions. The hardening can be then estimated from the number density and the mean size of the loops, using the dispersed barrier hardening model, first developed for neutron-irradiated materials by Seeger (1958) [28, 41, 42]. In this model, the hardening is expressed as the increase in the yield stress that is required to move a dislocation through a field of obstacles of strength α, with an average distance between obstacles, l:

$$\Delta\sigma_y = \alpha \cdot G \cdot \frac{b}{l} \qquad\qquad\qquad (1.5)$$

where G is the shear modulus, and b is the Burgers vector of the moving dislocation.

In the case of a random array of obstacles (clusters, dislocation loops) of diameter d and density N, $l = (N \cdot d)^{-1/2}$, and Eq. (1.5) becomes:

$$\Delta\sigma_y = \alpha \cdot G \cdot b \cdot \sqrt{N \cdot d} \qquad\qquad\qquad (1.6)$$

It was established that voids and large precipitates act like Orowan (perfectly hard) barriers; Frank loops and small MC precipitates have intermediate barrier strengths; small bubbles, small dislocation loops, small clusters and network dislocations have relatively small strengths.

Using the average dependence on dose and temperature of the size and defect density and the equation (1.6), one may conclude the following:

- At low irradiation/test temperature ($\sim$ 373 K), the hardening is dominated by black dot damage/small loops at low doses and networks of dislocations at higher doses. The absence of a bubble or void microstructure below 623 K suggests that the loop hardening accounts for the peak in yield stress at 573 K.
- At intermediate temperatures ($\sim$ 673 K), voids and bubbles make a significant contribution to hardening. At low doses the loop hardening dominates, while at high doses both void hardening and dislocation hardening are significant. Bubbles make a relatively small contribution to the total yield strength.
- At high irradiation temperatures ($\sim$ 873 K), loop hardening and bubble hardening make relatively small contributions. Hardening is dominated by networks of dislocations and, to lesser extent by voids, until high doses are achieved.

Figure 1.10 shows the yield strength variation with dose for various types of austenitic stainless steels [43] irradiated either with high energy protons or neutrons at various temperatures. The yield strength increases with increasing dose, showing a tendency to saturation from about 4 dpa, at values 4 to 6 times higher than the unirradiated value.
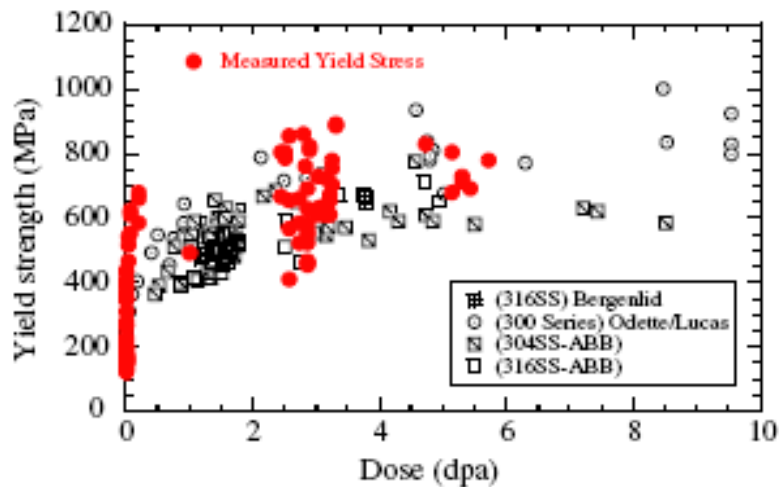
Figure 1.10. Yield strength variation with irradiation dose [43] (the red points are the measured values in [43] and the black ones the data found in the literature from the same authors).

Hardening of austenitic stainless steels is accompanied by a loss of work hardening and uniform elongation. This is generally attributed to the nature of interactions between mobile dislocations and the irradiation-induced microstructure. In unirradiated materials the interaction of dislocations with obstacles (other dislocations, precipitates) leads to dislocation blocking and the formation of debris and, in some austenitic structures, to plasticity-induced martensite formation; both of these lead to substantial work hardening of the materials. However, the interaction of dislocations with the irradiation-induced obstacles can lead to the elimination of the barriers by themselves, or can decrease their effectiveness as barriers, inducing a loss of work hardening. The increased flow localization that results from increasing shearable defects may produce a limited number of defect-free slip bands (dislocation channelling). The increased slip band spacing reduces the macroscopic displacements to a fixed dimension, and hence the ductility.

It was observed that the uniform elongation decreases significantly with increasing dose, and reaches a minimum for a dose that decreases with decreasing irradiation temperature down to about 573 K. Below 573 K the degradation in the uniform elongation appears to vary more slowly with the dose.

The deformation mechanism of irradiated and subsequently deformed austenitic stainless steels was studied by means of transmission electron microscopy. Twinning was found to be the dominant deformation mode at room temperature [29, 30, 32, 39, 44], while at a higher temperature of about 573 K, dislocation channeling was observed [30, 32, 39, 44]. Twinning in the specimens deformed at temperatures below 573 K was suggested to be due to strain rate effects (at low strain rates) and the presence of staking faults in the loops. The stacking faults favor the nucleation of twins when they interact with gliding dislocations. The critical stress for twining decreases with increasing loop size, while the critical stress for glide increases simultaneously. The temperature dependence of the operating mechanism is explained by the increase in staking fault energy with the temperature.

The degradation in ductility and the change in fracture mode also lead to a decrease in the fracture toughness. The data on fracture toughness of irradiated austenitic stainless steels are limited, however.

1.4.5 Irradiation-assisted stress corrosion cracking

After many years of service, the internal components and structural parts of BWRs and PWRs may exhibit irradiation-assisted stress corrosion cracking [45, 46]. This phenomenon occurs in stainless steels subjected to a significant flux of neutron irradiation in the reactor coolant environment. The environment is typically oxygenated or hydrogenated water at about 290°C. As stress corrosion cracking requires a combination of irradiation, stresses, and corrosive environment, the failure mechanism is commonly referred to as irradiation-assisted stress corrosion cracking (IASCC). The effect of neutron fluence and equivalent dose on the susceptibility to IASCC of type 304 stainless steels in reactor environments is illustrated in Figure 1.11 [27].
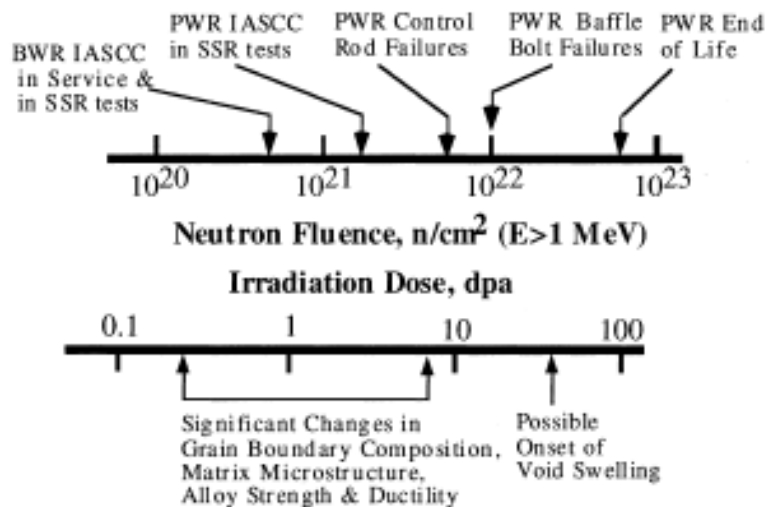
Figure 1.11. Neutron fluence and equivalent dose effects on the IASCC susceptibility of type 304 stainless steels irradiated in PWR or BWR conditions [27].

Two factors influencing the susceptibility to IASCC are the evolution of the microstructure with time, caused by fast neutrons, and the influence of ionizing radiation on the environmental chemistry. Displacements of atoms from their lattice site lead to changes in the grain boundaries composition if the temperature is high enough for allowing diffusion of point defects to sinks.

During the irradiation, the degree of segregation of alloying elements increases with dose, along with changes in dislocation microstructure, hardness and cracking susceptibility, as shown in Figure 1.12 [47]. With increasing dose, the cracking susceptibility increases at approximately the same rate as the degree of Cr depletion,

Ni and Si enrichment at the grain boundaries. Phosphorus segregation is more complex, reaching a maximum level at an intermediate dose and then returning to the bulk level.

The threshold dose for the appearance of intergranular cracking is stress dependent, increasing with decreasing stress. The extent of intergranular cracking increases with dose, but the increase is highly sensitive to the oxygen concentration in the water, high oxygen concentrations lead to almost complete intergranular fracture after a few dpa, under high stresses.

Although the specific irradiation-induced microstructural and microchemical changes that promote IASCC susceptibility are still largely unknown, it is believed that radiation-induced Cr depletion at grain boundaries is primarily responsible. Data suggest that the onset of intergranular cracking corresponds to the achievement of (minimum) concentration of Cr (around 13 wt. %) over a minimum distance from the grain boundary of about 5 nm.
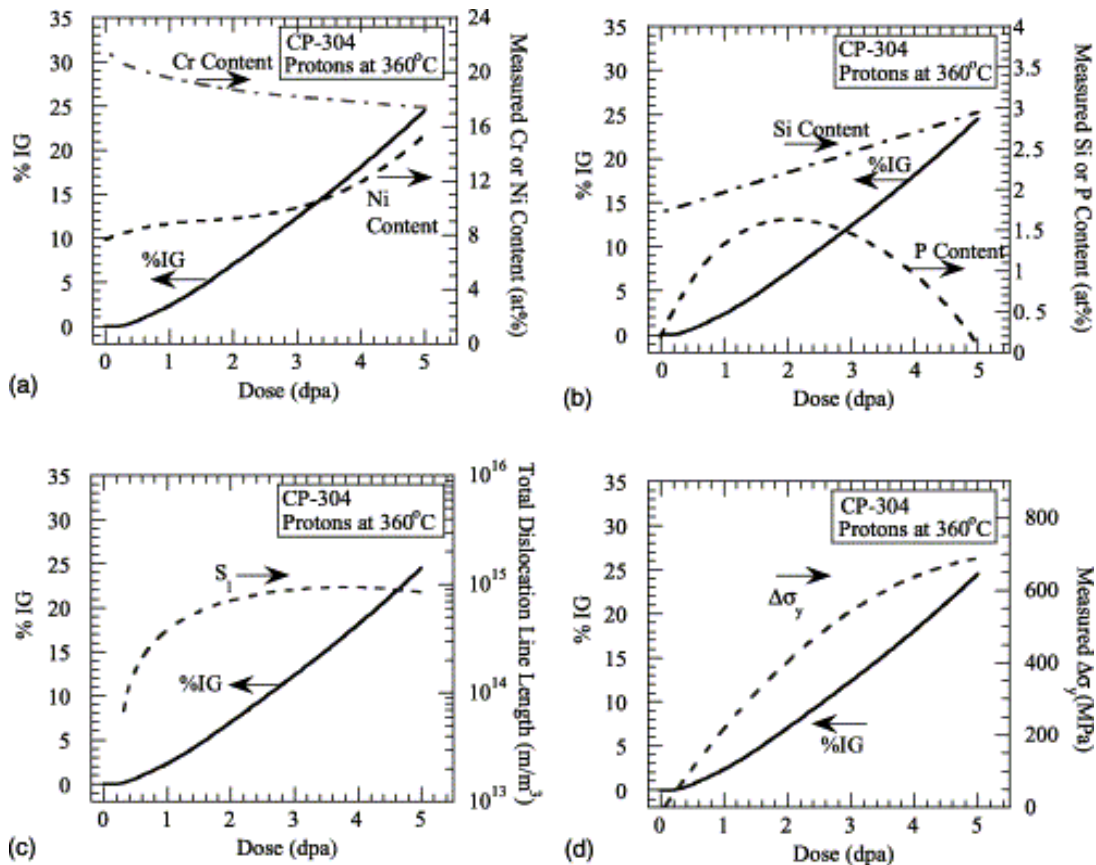
Figure 1.12. Dose dependence of the crack susceptibility (%IG) and (a) contents of major alloying elements, (b) contents of minor alloying elements, (c) total dislocation line length, and (d) hardening for the CP-304 stainless steel proton irradiated at 360°C [47].

CHAPTER 2

EXPERIMENTAL PROCEDURE

This chapter includes a description of the two test materials, AISI 304 and AISI 347, the welding procedure and the neutron irradiation conditions, as well as details on the in-service material, of the AISI 304 type.

The various characterisation tools used in the present study, optical microscopy, Vickers microhardness measurements, tensile mechanical testing, scanning electron microscopy, transmission electron microscopy, are also described, together with the corresponding sample preparation procedures.

2.1 Materials

2.1.1 The test materials

Austenitic stainless steels of the type AISI 304 (according to the American Iron & Steel Institute Standard) are usually used for the construction of core shrouds of boiling water reactors. In the present study, besides the AISI 304, the AISI 347 stainless steel was also used. The chemical composition of these two steels is listed in Table 2.1.

Table 2.1. Chemical composition of the base test materials, in wt.%.

Material	C	Si	Mn	P	S	Cr	Ni	Nb	Fe
AISI347	0.03	0.46	1.22	0.034	0.005	17.69	10.34	0.49	bal.
AISI304	0.042	0.31	1.63	0.03	0.01	18.36	9.5	–	bal.

The AISI 347 was chosen for the present study because it is stabilized with niobium. Niobium possesses a high affinity to carbon and very stable carbides such as NbC or Nb_4C_3 may form. At 1050°C carbon is "stably" linked to niobium and residual amounts of ferrite and sigma phase are dissolved in austenite. By subsequent rapid cooling (quenching) this state is maintained down to the ambient temperature. This effect is used in stainless steels and in weld metals to arrest the carbon in the form of niobium carbides, thereby improving the resistance to intergranular corrosion.

A heat treatment was applied to both materials: heating at 1050°C, followed by water quenching. During this heat treatment, the $M_{23}C_6$ carbides, the sigma phase and the delta ferrite are completely dissolved and a homogeneous, fully austenitic structure is produced.

2.1.1.1 The welding process

Two plates from each material, with the dimensions of 2500 mm x 200 mm x 12 mm, were joined together by fusion welding at FRAMATOME ANP, Germany. The following welding processes have been used: gas tungsten arc welding for the root pass and manual shielded metal arc welding for the subsequent passes.

The melting temperature necessary to weld materials in the gas tungsten arc welding (GTAW) process is obtained by producing an arc between a tungsten alloy electrode and the work piece. Weld pool temperatures can approach 2500ºC. An inert gas (argon, helium, or a mixture of helium and argon) sustains the arc and protects the molten metal from atmospheric contamination.

In the shielded metal arc welding process (SMAW), an arc is generated between a flux covered consumable electrode and the work piece. The process uses the decomposition of the flux covering to generate a shielding gas and to provide fluxing elements to protect the molten weld metal droplets and the weld pool. The arc is initiated by momentarily touching the base material with the electrode. The resulting arc melts both the base metal and the tip of the welding electrode. The molten electrode metal/flux is transferred across the arc (by arc forces) to the base metal pool, where it becomes the weld deposit covered by the protective, less-dense slag from the electrode covering.

The chosen welding procedure was a compromise between the conditions applied to real boiling water reactor components and the restrictions concerning the dimensions and the allowable deformation imposed in the present research project. The welding process parameters are listed in Table 2.2 and the chemical composition of the filler metals in Table 2.3 [6]. The welding geometry was chosen as a double–V shape, in order to optimise the welding related distortion and specimen sampling for laboratory experiments (Figure 2.1).
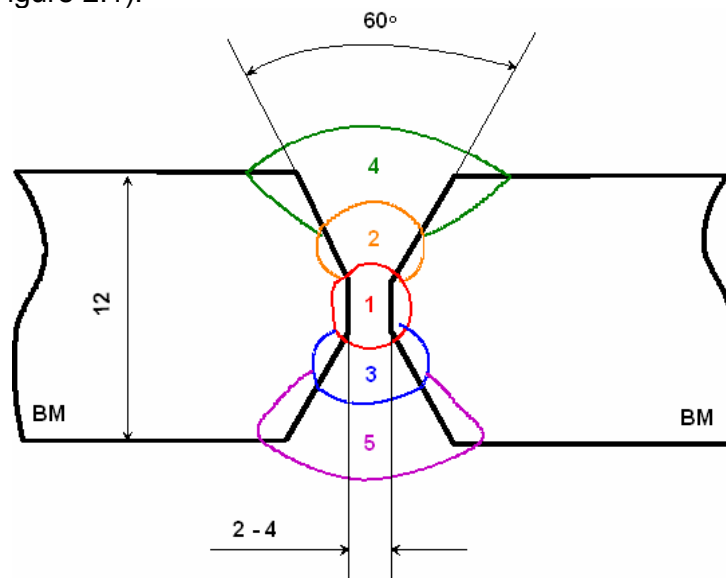

Figure 2.1. Welding passes sequence (all dimensions are in mm; BM = base material).

Table 2.2. Welding process parameters.

Pass no.	Filler metal	Shielding gas, l/min	Welding current, A	Interpass temperature, °C
1	Böhler SAS 2IG	11	140	20
2-3	Oerlikon Inox F347	–	105	<100
4-5	Oerlikon Inox F347	–	130	<100

Table 2.3. Chemical composition of the filler materials, in wt. %.

Material	C	Si	Mn	P	S	Cr	Ni,	Nb	4)
1)	0.035	0.5	1.4	–	–	19.4	9.5	+	11-12
2)	0.014	0.99	0.68	0.014	0.014	18.6	9.8	0.42	13
3)	0.017	0.95	0.63	0.015	0.015	18.8	9.8	0.44	13

1) Böhler SAS 2-IG ER 347, diameter 2.0 mm.
2) Oerlikon Inox F347, diameter 3.25 mm, for passes 2 and 3.
3) Oerlikon Inox F347, diameter 4.0 mm, for passes 4 and 5.
4) Delta-Ferrite content, calculated according to DeLong diagram.

2.1.1.2 Irradiation experiments

Tensile specimens and disks for transmission electron microscopy observations (see § 2.2) from the heat-affected zones of AISI 304 and AISI 347 test weld materials have been neutron irradiated in the Nuclear Research and Consultancy Group (NRG), Petten, The Netherlands, using a High Flux Reactor (HFR) in which all irradiation parameters (temperature, neutron energy, fluence) can be well controlled [6]. The irradiation temperature was 290°C, with a maximum target deviation of ± 10°C. Analyses of the heat transfer of the welded coupons were done to limit the thermal gradient to 20°C maximum in order not to affect the weld residual stresses. The temperature distribution within the specimen holder was monitored by 24 thermocouples. For cooling a mixture of argon and neon gases was used. To evaluate the pre-design and post-irradiation process concerning nuclear and thermal

data different computing codes were used. The main parameters of the evaluation included the thermal (Co) and fast (E > 1 MeV) neutron fluences derived and the accumulated damage (number of dpa). Two different doses were accumulated, namely 0.3 dpa and 1 dpa, for both AISI 304 and AISI 347.

2.1.2 The in-service material

The so-called in-service material refers to the thermal shield of a decommissioned experimental pressurised water reactor (PWR), the BR-3, located at the Belgian Nuclear Research Centre, SCK•CEN, in Mol, Belgium.

The thermal shield (Figure 2.2) has been irradiated during 11 reactor cycles between 1962 and 1987. During that period the reactor has experienced 5'000 effective full power days at 40 MW_{th} (electric power of 11.5 MW), with a coolant temperature in the range of 260 – 300°C [6]. As the BR-3 reactor was an experimental PWR, its operating temperature and power were quite lower than those of the new generation of PWRs. Therefore, the exposure conditions of the thermal shield material are comparable to the current exposure conditions in boiling water reactors (BWRs), where the coolant temperature is about 290°C, whereas it is 320°C and higher in the new PWRs.

The material used for the thermal shield was a stainless steel of the type 304, with the following chemical composition: 0.08% C, 0.75% Si, 2% Mn, 0.045% P, 0.03% S, 18.0% Cr, 8.0% Ni, and Fe for the balance (in wt. %).

Two sample blocks of the thermal shield were kept apart following the decommissioning of the reactor. Both are plates of approximately 500 mm x 500 mm with a weld running trough the centre. The first part (termed Block A, or low dose material) was taken from the top part of the thermal shield, at 975 mm above the mid plane (Figure 2.2). The second part (termed Block B, or high dose material) was taken at 23 mm above the mid plane. Both plates have the same thermal history but have accumulated different irradiation doses. In addition, the accumulated dose of the in-service material decreases from the inner side of the reactor to the outer side. The dose variations are listed in Table 2.4, for both Block A (low dose material) and Block B (high dose material).

Table 2.4. Accumulated doses in the inner and outer regions of the Block A and Block B in-service material.

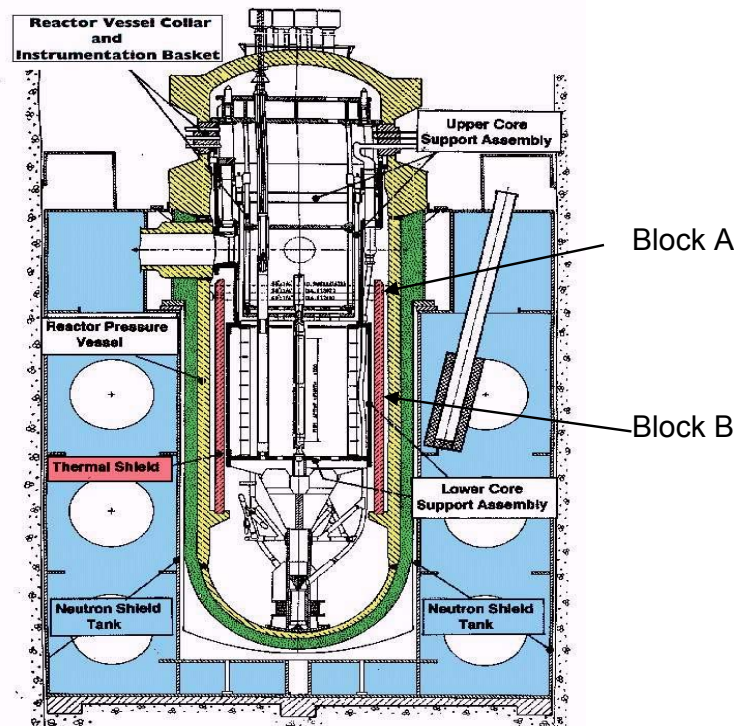|	Block A		Block B	
	inner	outer	inner	outer
Flux, $n \cdot cm^{-2} \cdot s^{-1}$	$1 \cdot 10^8$	–	$8 \cdot 10^{11}$	$2 \cdot 10^{11}$
Dose, $n \cdot cm^{-2}$	$9 \cdot 10^{16}$	$0.9 \cdot 10^{16}$	$2.4 \cdot 10^{20}$	$0.9 \cdot 10^{20}$
Dose, dpa	$1.3 \cdot 10^{-4}$	$1.3 \cdot 10^{-5}$	0.35	0.12

Figure 2.2. Sketch of the experimental PWR BR-3.

2.2 Tensile mechanical testing

Tensile tests were performed on unirradiated and irradiated materials, at two different deformation temperatures: 293 K (room temperature) and 573 K.

2.2.1 Tensile test specimens

Because of the small extension of the heat-affected zone, tensile tests were performed in the frame of small specimen technology, using specimens with the PIREX geometry (Figure 2.3). The PIREX geometry has been validated by comparing the obtained results to those obtained using specimens with the DIN geometry (3 mm in diameter) [48]. The analyses showed that the measured yield strength, ultimate tensile strength and uniform strain are the same for both geometries. The total plastic strain at fracture was found to be slightly affected by the small specimen geometry, as expected. However, this is not of great importance, as the goal of this work is to compare the results obtained for irradiated specimens to those obtained for the unirradiated ones.
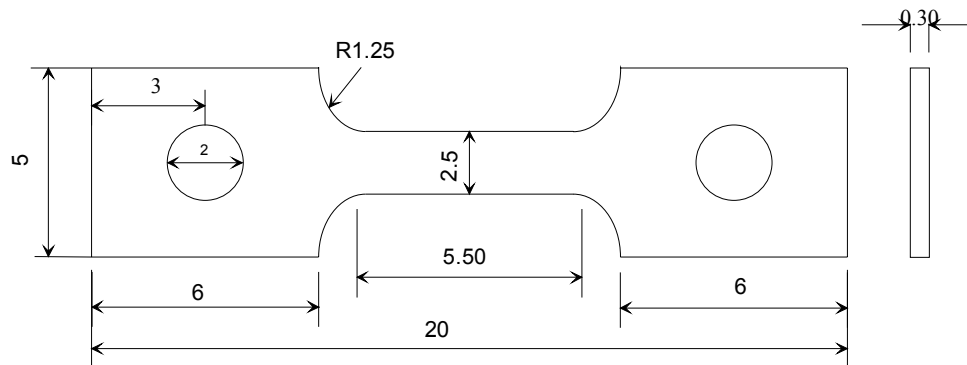
*Figure 2.3. The PIREX tensile specimen geometry
(dimensions are expressed in mm).*

2.2.1.1 The test weld materials tensile specimens

Tensile specimens were cut out by spark erosion from the heat-affected zones of the AISI 304 and AISI 347 test welds, parallel to the fusion line, as shown in Figure 2.4. In the case of the unirradiated materials, 5 tensile specimens were cut out at different distances from the fusion line, at about 0, 400, 800, 1200, 1600 μm away. In addition, specimens were also cut out from the base material, far away from the fusion line, and from the weld metal, for microstructure and mechanical properties comparison purposes.In the case of specimens to be irradiated, four tensile specimens were cut out in NRG Petten, at different distances from the fusion line (according to Figure 2.5), and introduced for irradiation in the HFR.

The electric spark erosion (EDM – Electrical Discharge Machining) is characterised by individual electric discharges (spark, pulses) occurring between an electrode and the work piece inside a dielectric (e.g. deionised water). The spark is controlled and localised so that it only affects the surface of the material. The EDM wire cutting uses a metallic wire to cut a programmed contour inside the work piece.

Tensile tests were performed on both mechanically polished and unpolished specimens. In the case of polished specimens the surfaces were mechanically polished up to 1'000 SiC grit paper to remove the layer resulting from spark erosion and trying to keep both surfaces as parallel as possible. The results obtained using unpolished specimens showed no significant difference compared to those obtained using polished ones. The tensile specimens prepared in Petten have been carefully mechanically polished before irradiation.
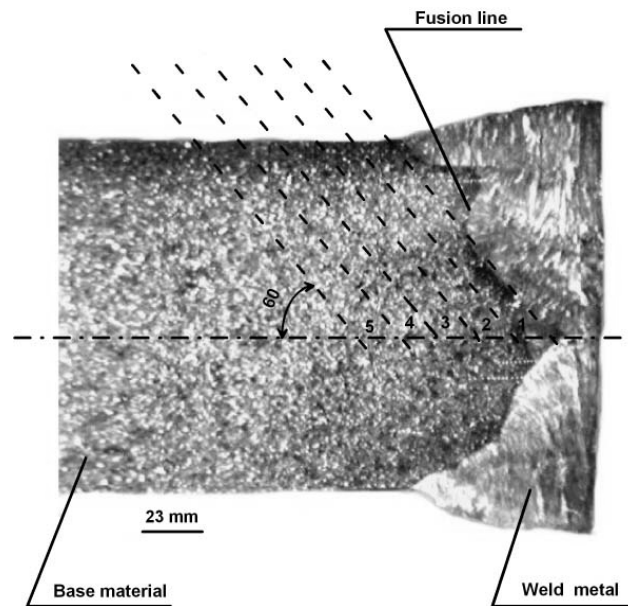
Figure 2.4. Indicative cutting plan of the specimens from the heat-affected zone (the thickness of the cut plates was actually 0.4 mm).
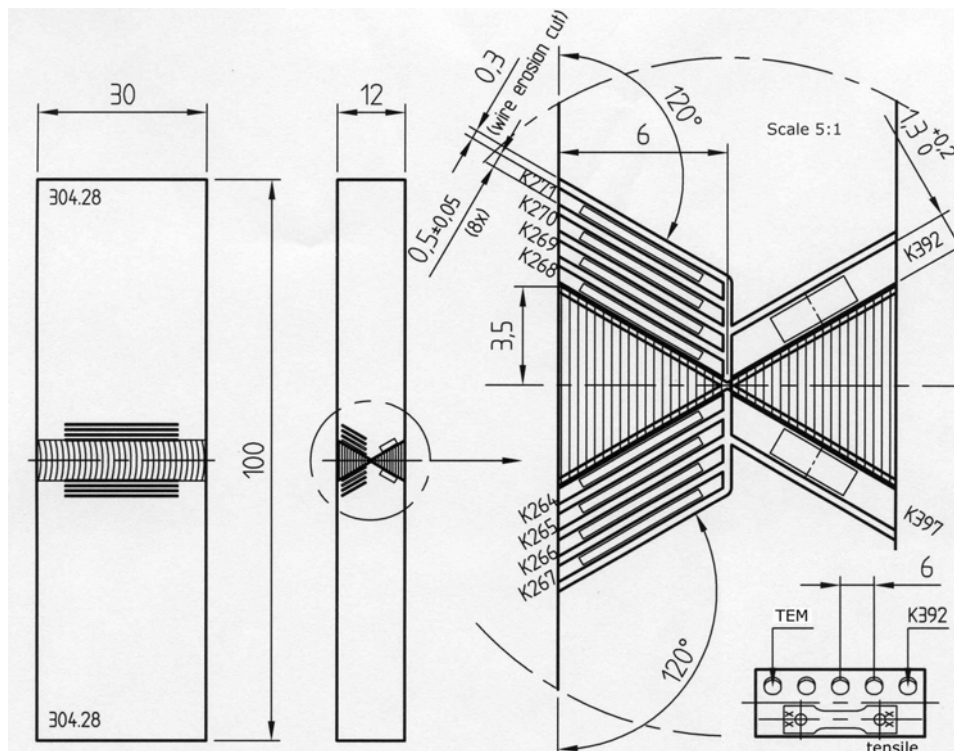
Figure 2.5. Cutting plan of the specimens from the heat affected zone destined to be irradiated in Petten (all the dimensions are in mm).

2.2.1.2 The in-service material tensile specimens

The weld geometry in the case of the in-service material is different from that of the test materials. Another cutting plan was necessary for preparing tensile specimens from the heat-affected zones and base materials of both blocks of the in-service material. 72 mm long plates were cut out parallel to the fusion line, according to Figures 2.6.a and b. Tensile specimens for mechanical testing, with the PIREX geometry, were prepared from these plates (Figure 2.6.c). The accumulated dose of the tensile specimens varies with the position of the specimen inside the plate, according to Table 2.4.

Because of the high dose rate of the in-service material, all the specimens were cut out inside a hot cell. The hot cells are providing a safe, remote handling of highly radioactive materials. A wire electro-erosion machine was installed inside the hot cell, and the specimen cutting was performed using manipulators (Figure 2.7).

The tensile specimens were not mechanically polished before testing, due to the high activity of the Block B material.
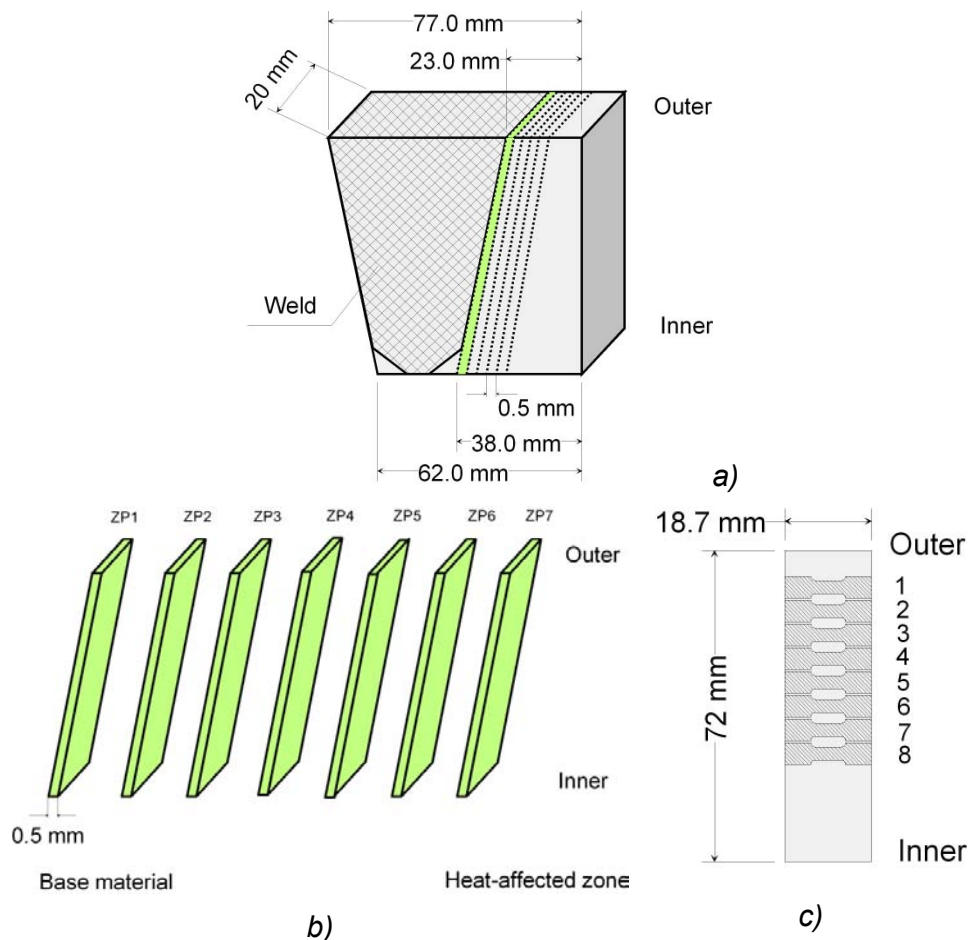
Figure 2.6. Cutting scheme of the in-service material, Block A and Block B. a) Cutting plan according to the weld geometry; b) numbering of the cut plates as a function of the distance from the fusion line; c) cutting of the tensile specimens inside one plate, and numbering as a function of the accumulated dose.

Figure 2.7. Electro-erosion cutting of tensile test specimens of the in-service material inside a hot cell using manipulators.

2.2.2 Testing machines

In the case of the unirradiated materials the tensile tests were performed in a SCHENCK RMC 100 deformation machine (Figure 2.8), with the following characteristics:
- 15 kN load cell
- double columns for a good stiffness
- heating furnace – up to 1000 K, coupled with a cooling system and a vacuum system to avoid oxidation of the samples
- the displacement speed is between 0.01 and 99.99 mm/min
- the deformation of the sample is measured with two linear variable differential transducer (LVDT) extensometers connected to the specimen holder by two ceramic rods
- the data are saved in ASCII format on the computer monitoring the test. The data are analysed with a software developed by Joel Bonneville and Philippe Spätig, EPFL.

For the irradiated materials, the tensile tests were performed in a ZWICK machine of the type Z 010 (Figure 2.9) shielded with a 5 cm lead wall, and adjusted for small specimen testing. The Zwick machine has the following characteristics:
- 2.5 kN and 10 kN load cells
- heating furnace – up to 1273 K, coupled with a cooling system, a quartz tube and a vacuum system
- the displacement speed can vary between 0.02 and 20 mm/min
- the deformation of the sample is measured by the displacement of the traverse
- the data are saved in ASCII format on the computer monitoring the test.

Because of the very high activity of the specimens irradiated in Petten it was necessary to install the ZWICK tensile machine inside a hot-cell.

Tensile tests were performed at two different temperatures: room temperature (in air) and 573 K (under vacuum or in an argon flow, in order to avoid the oxidation of the specimen). Various strain rates were used, ranging between $1.55 \times 10^{-4}\,s^{-1}$ and $8.7 \times 10^{-3}\,s^{-1}$. Most of the tests were conducted at a strain rate of $5 \times 10^{-4}\,s^{-1}$.

Values of the different tensile test parameters (yield strength, ultimate tensile strength, uniform elongation) were averaged from a minimum of ten measurements in the case of the unirradiated base materials. Due to the small amounts of available specimens in the case of heat-affected zones and irradiated materials, only one specimen was tested per condition.

The yield strength (YS) was measured at 0.2 % plastic strain. The ultimate tensile strength (UTS) corresponds to the maximum stress, where necking is expected to start. The uniform elongation (UE) was measured at the highest stress level, i.e. at the onset of the necking. The mean deviation value of the various parameters was calculated as the following:

$$D = \sqrt{\frac{(x_1 - m)^2 + (x_2 - m)^2 + \ldots\ldots + (x_n - m)^2}{n}} \qquad\qquad (2.1)$$

where m, the mean value, is the sum of all the measurements divided by the number of measurements, n.

Figure 2.8. The SCHENCK RMC 100 tensile testing machine.

Figure 2.9. The ZWICK Z010 tensile testing machine and the specimen grips.

2.3 Microhardness measurements

2.3.1 The test welded materials

Vickers Microhardness measurements were performed using a force of 1 N, applied during one second, with a loading slope of 0.05 N/s (HV 0.1). In the case of the AISI 347 material, the first microhardness measurement was done along the fusion line. For the AISI 304 material, the first microhardness measurement was done in the middle of the weld metal. Subsequent measurements were performed in the heat-affected zone towards the base material.

The images have been acquired with a high resolution digital camera and treated using the image analysis software IMAGIC for contrast optimization. The size of the indentation has been determined on the calibrated picture using the measurement capabilities of the image analysis software. The Vickers microhardness was calculated using the following formula:

$$HV = 1.89096 \cdot 10^5 \cdot \frac{F}{d^2} \tag{2.2}$$

where F is the applied force

and $d = \dfrac{d_1 + d_2}{2}$ (2.3)

where d_1 and d_2 are the diagonals of the indentation.

2.3.2 In-service material

Vickers microhardness measurements for the in-service material were performed using the same procedure as in the case of the unirradiated test weld materials.

2.4 Microscopic observations

2.4.1 Optical microscopy

Optical microscopy observations were performed on the unirradiated test weld materials and on the in-service material in order to determine the weld geometry and the extension of the heat-affected zone of the weld, by measuring the grain size distribution as a function of the distance from the fusion line.

2.4.1.1 Sample preparation

Samples from the unirradiated test weld materials AISI 304 and AISI 347 were prepared for metallographic observations. The samples were mounted into epoxy resin and polished with SiC papers of successively finer grades to obtain a mirror surface. The finer polishing steps were performed on a cloth using first a diamond paste of 1 μm and second an OPS (Struers GmbH) polishing suspension. The AISI 347 sample was etched by immersion for 2 minutes in a solution of 30 ml nitric acid, 40 ml hydrochloric acid and 40 ml distilled water, at room temperature. The AISI 304 sample was etched for 3.5 minutes using the V 2 A reagent, at 55ºC. An example of metallographic sample is shown in Figure 2.10.

The specimens used for the investigation of the microstructure of the in-service material have been cut out with an electro-erosion machine inside a hot cell, into small pieces of 28 mm x 10 mm x 3 mm. The preparation procedure was identical to the one used for the unirradiated test weld materials. The grain boundaries have been revealed by etching the specimens in a solution of 30 ml nitric acid, 40 ml hydrochloric acid and 40 ml distilled water, at room temperature, for 40 seconds.
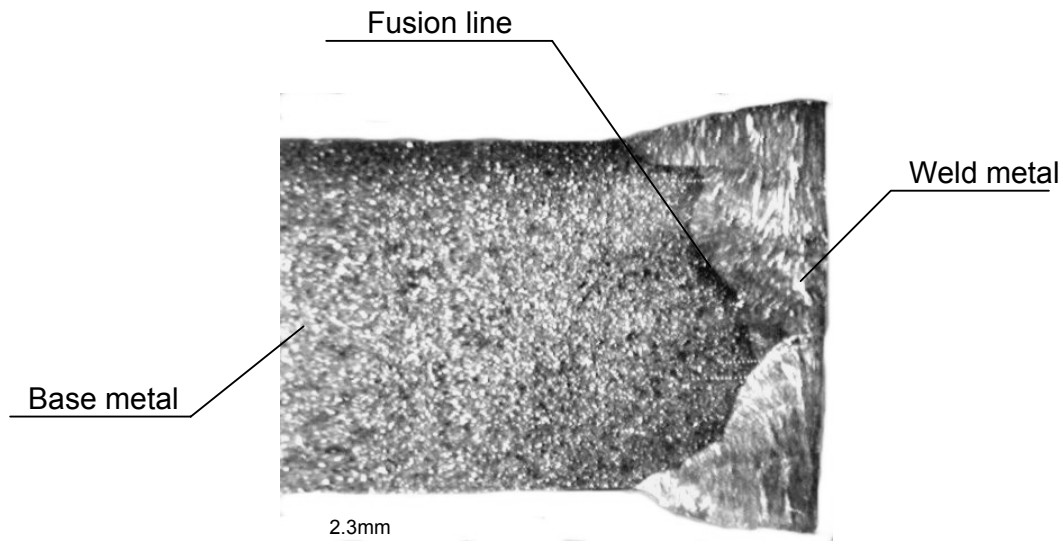
Figure 2.10. Metallographic sample, AISI 304.

2.4.1.2 Grain size measurements

The grain size of the unirradiated test weld materials was measured by the intersection method: a straight line, with a finite length *L*, is drawn on the micrograph and the number of intersections *N* between the line and the grain boundaries is counted. The grain size is then given by *N/L*.

The grain size of the in-service material was determined according to the ASTM E112 – 96[E1] standard, using the intercept procedure. This standard procedure consists in estimating the average grain size by counting the grain boundary intersections with circular test lines. The test pattern consisted of three concentric and equally spaced circles having a total circumference of 500 mm. This pattern was successively applied to at least five blindly selected and widely spaced fields, and the number of intersections per pattern for each of the tests was recorded separately. The selected magnification should yield 40 to 100 intersection counts per placement of the three circle test grid. The goal is to obtain a total of about 400 to 500 counts.

The number of grain boundary intersections per unit length of the test line is given by:

$$P_L = \frac{P_i}{L} \tag{2.4}$$

where P_i is the number of intersections counted in the field and L is the total test line length (500 mm).

The mean lineal intercept value for each field, *l*, is given by:

$$l = \frac{1}{P_L} \tag{2.5}$$

The ASTM grain size, *G*, was determined using:

$$G = \left(-6.643856 \cdot \log_{10} l\right) - 3.288 \qquad\qquad (2.6)$$

Finally, the average diameter of the grains was determined using the calculated ASTM grain sizes given in the tables of the corresponding standard.

2.4.1.3 Optical microscopes

Optical microscopy observations were made on the unirradiated test weld materials and the in-service material irradiated to low dose (Block A) using an optical microscope Zeiss Jenaphot 2000. For the in-service material irradiated to high dose (Block B), a shielded optical microscope Leica Telatom-4 in the PSI Hot Laboratory was used. The images were acquired with a high resolution digital camera and treated using the image analysis software IMAGIC for contrast optimization.

2.4.2 Scanning electron microscopy

2.4.2.1 Preparation of the samples

Scanning electron microscopy (SEM) observations of fracture surfaces, following tensile deformation, were performed on unirradiated samples from the test base materials. No special preparation was necessary, as the SEM observations were made on polished tensile specimens.

2.4.2.2 Scanning electron microscope

SEM investigations were performed using a Zeiss DSM 962 microscope, operating at 30 kV.

2.4.3 Transmission electron microscopy

Transmission electron microscopy (TEM) observations were performed on undeformed and deformed samples of base and weld metals and HAZs of the test welded materials and the in-service material, in both the unirradiated and the irradiated states. Different types of observation techniques were used to investigate the welding, deformation and/or irradiation-induced microstructure.

2.4.3.1 Preparation of the samples

In the case of the unirradiated materials, TEM samples were prepared by punching 3 mm discs from the various materials, at different distances away from the fusion

line. The discs were mechanically polished in order to reduce the thickness to approximately 100 μm. Then, the TEM samples were electrolytically thinned by jet polishing using a TENUPOL (STRUERS) device. An electrolytic solution was used, with the following composition: 10% perchloric acid, 15% ethylene glycol, and 75% methanol. The electro-polishing temperature was around 0°C and the voltage was around 20 V. In the case of the in-service material (Block A and B), in order to reduce the activity of the specimens, 1 mm TEM disks were punched out from the materials. As the TEM specimen holder is designated for 3 mm disks, the 1 mm disk had to be inserted into a 3 mm disk made of stainless steel for compatibility purposes. In the middle of the 3 mm disk, a 1 mm hole is punched and the 1 mm specimen is inserted and glued with an epoxy resin. The specimen obtained in this way is prepared further as a usual 3 mm TEM disk (see above).

TEM disks from the test weld materials have been prepared before irradiation in Petten, according to Figure 2.5. Due to the minimum size of specimens that can be irradiated in the HFR, the TEM disks were 1 mm in thickness and 3 mm in diameter. After irradiation, the specimens were cut with a wire saw inside a fume box at the PSI, in order to reduce the thickness to about 0.4 mm. The thin specimen has been further prepared according to the above procedure. Due to the very high thickness of the irradiated TEM specimens (1 mm), the exact position of the resulting specimen studied in TEM, with respect to the fusion line, could not be exactly determined.

2.4.3.2 Transmission electron microscope

TEM observations were performed using a JOEL 2010 type microscope, operating at 200 kV, equipped with a TV camera, a CCD camera, and a detector for energy dispersive spectrometry (EDS) measurements.

2.4.3.3 Observation techniques

TEM observations of the welding-induced microstructure and the deformation-induced microstructure were made using magnifications between 20'000 to 100'000 times, while observations of the irradiation-induced defects required higher magnifications.

The overview of the microstructure was obtained using conventional bright-field (BF) and dark-field (DF) imaging techniques. For the observation of the small irradiation-induced defects, DF or weak beam dark field (WBDF) imaging techniques were used.

A typical bright-field kinematical condition is shown in Figure 2.11.a [49]. In order to obtain good bright-field images, the specimen must be tilted slightly away from the Bragg condition, so that the image loses most of its dynamical features. Weak-beam images are dark-field images obtained using a weakly-excited beam, with the specimen tilted sufficiently away from the Bragg condition (Figure 2.11.b). The magnitude of the deviation parameter to the Ewald sphere s_g is then large. The deviation parameter characterises the diffraction condition and it represents the distance from the diffraction vector g to the Ewald sphere in a direction normal to the specimen (Figure 2.12). In weak-beam conditions the contrast arises from regions of

large lattice strain close to the core of the defects. For quantitative measurements it is necessary to image the defects with a value of the deviation parameter

$$\left| s_g \right| \geq 2 \cdot 10^{-1}\,\text{nm}^{-1} \qquad\qquad (2.7)$$

To achieve a minimum value for the deviation parameter, specific diffraction conditions are needed. The required value of n (the point where the Ewald sphere cuts the line of systematic reflections, according to Figure 2.12) for a given s_g and vice versa can be determined diffraction patterns, as illustrated in Figure 2.12, where the n value is slightly larger than 3. Using the theorem of intersecting chords, the following relation can be derived:

$$s_g = (n-1) \cdot \frac{g^2}{2 \cdot k} \qquad\qquad (2.8)$$

where $g = \dfrac{1}{d_{hkl}}$ is the magnitude of the reciprocal lattice vector g corresponding to the diffracting planes (hkl) with an interplanar spacing d_{hkl}

and $k = \dfrac{1}{\lambda}$ is the radius of the Ewald sphere, λ being the electron wavelength.

This condition is usually denoted ng(mg), where mg is at the Bragg condition, and the reflection ng is used to form the dark field image.

Figure 2.11. Two different types of diffraction condition used in diffraction-contrast imaging: a) kinematical bright field, b) weak-beam, g(3g).
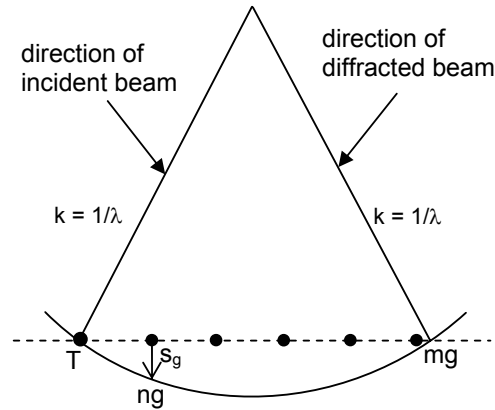
Figure 2.12. Determination of the deviation parameter s_g from the diffraction pattern.

2.4.3.4 Thickness measurements

Knowing the sample thickness is important for determining the defect size and density by means of transmission electron microscopy. The sample thickness can be determined by a variety of methods in TEM [50]. In the present study, the convergent beam electron diffraction (CBED) technique was used.

Historically, CBED is the oldest TEM diffraction technique. It was proposed by Kossel and Möllenstedt in 1939. CBED is a microanalytical technique that uses a convergent or focused beam of electrons to obtain diffraction patterns from small specimen regions. CBED patterns consist of diffraction disks (rather than diffraction spots) that are rich in detail and can be exploited to reveal various aspects of the specimen microstructure. The spatial resolution of the technique is related to the focussed incident probe size. Possible applications of CBED are:

- measurement of specimens thickness
- measurement of small (0.1%) changes in lattice parameter
- symmetry determination (point and space groups for crystallographic analyses of new phases, analyses of phase transformations
- low-order structure factor amplitude and phase determination
- Burgers vector determination

Figure 2.13 shows an experimental CBED pattern obtained close to a <011> zone axis with the operating diffraction vector g {220} in AISI 347 stainless steel. The broad dark bands result from diffraction by all planes of the (hkl) type. The variation of the intensity with thickness is known as "Pendellosung" or thickness fringe oscillations. The thinner lines (high order Laue zones, HOLZ, lines) show the trajectories of points along which the Bragg condition is satisfied for a higher order Laue zone (HOLZ) reflection with different indices.

The CBED method for measuring the specimen thickness is based on the following equation [51]:

$$\left(\frac{s_i}{n_i}\right)^2 + \left(\frac{1}{n_i}\right)^2 \cdot \left(\frac{1}{\xi_g}\right)^2 = \left(\frac{1}{t}\right)^2 \qquad\qquad (2.9)$$

where s_i is the excitation error at the ith minimum, t is the effective specimen thickness in the beam direction and ξ_g is the extinction distance.

In the experimental image, the distance s between the centre of the incident beam direction and the corresponding fringe in the (111) disk which, is at the Bragg condition, is measured. The excitation error s_i between the Bragg condition and all visible intensity fringes is also measured. With the obtained values, the dependence of $(s_i/n_i)^2$ against $(1/n_i)^2$ can be plotted (Figure 2.14). The plot gives $(1/t)^2$ at the intercept, and hence the thickness. The slope of the plot gives $(1/\xi_g)^2$. We note that i = 1 corresponds to the first minimum either inside or outside the Bragg condition. An important problem arises from how to determine the first value of n. For a sample thickness $t < \xi_g$ $n_1 = 1$; for $\xi_g < t < 2\xi_g$, $n_1 = 2$, and so on. Thus n_1 is the first integer larger than t/ξ_g. In practice, one uses several initial values till a good straight line fit is obtained for a reasonable value of ξ_g, as in Figure 2.14. From the graph in Figure 2.14, the thickness was found to be 110 nm for an extinction distance of 57 nm.
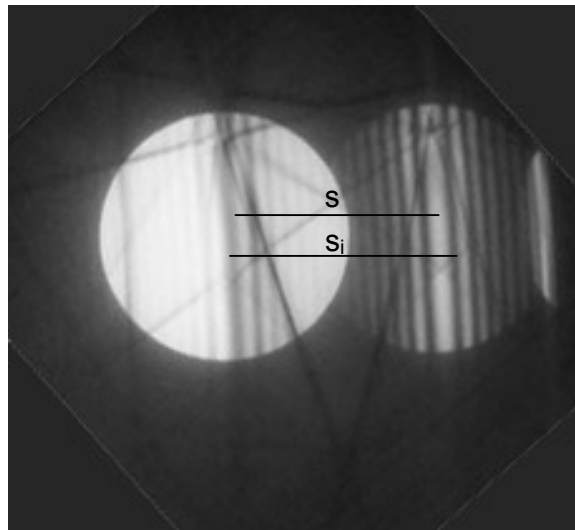
Figure 2.13. Experimental CBED image with the diffraction vector {220} close to a <011> plane.
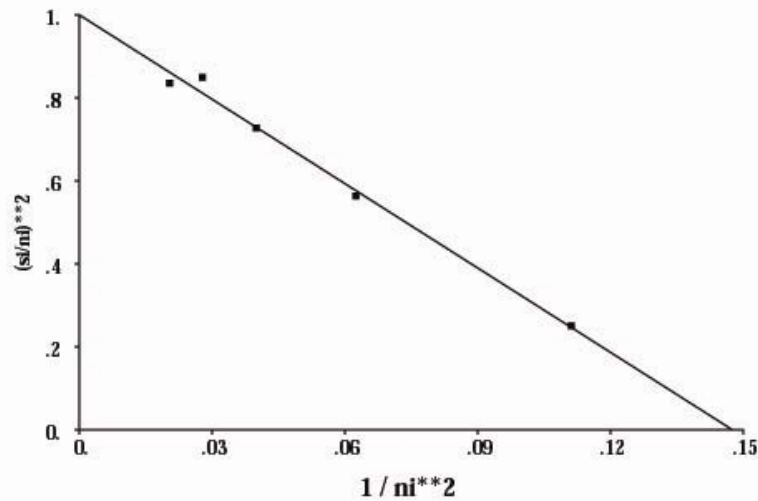
Figure 2.14. Graph of $(s_i/n_i)^2$ against $(1/n_i)^2$ for thickness determination for the experimental CBED image shown in Figure 2.13.

By using the CBED method, the specimen thickness can be determined with an uncertainty of $\pm$ 10 %, due to the excitation of other orders in the zero order Laue systematic row, which can produce subtle changes in the intensity distribution inside the disk at the Bragg condition.

2.4.3.5 Stacking fault energy measurement

The stacking fault energy is essential to any fundamental understanding of the evolution of the microstructure and deformation mechanisms. The stacking fault energy influences dislocation cross slip and climb, which are the dominant factors for work hardening and creep behaviour. The stacking fault energy also affects the susceptibility to stress corrosion cracking.

The most frequently used method to determine the stacking fault energy is the measurement of the extended dislocation nodes by transmission electron microscopy [52, 53]. The TEM resolution limit restricts this method to cases where $\gamma \leq 50$ mJ/m^2, except where one uses weak beam images.

In order to determine the stacking fault energy, WBDF images of dissociated dislocations lying in the foil plane were taken in TEM. In addition, the dislocation images of dissociated dislocations were simulated within the framework of linear anisotropic elasticity of infinite continuous medium [54], in order to determine the actual dissociation width from the apparent one measured on TEM images. The stacking fault energy was calculated in anisotropic elasticity, using the formula for equilibrium separation between two parallel dislocations [55], the ANCALC programme [56], and the actual separation distance between dissociated dislocations, as deduced from iterative comparison between experimental and simulated images.

The elastic constants necessary for these calculations were determined using the following formulae [57], and the obtained values are listed in Table 2.5:

$$c_{11} = 2 \cdot \mu + \lambda$$
$$c_{12} = \lambda \qquad\qquad\qquad (2.10)$$
$$c_{44} = \frac{c_{11} - c_{12}}{2}$$

where µ is the shear modulus and is calculated using:

$$\mu = \frac{E}{2 \cdot (1 + v)} \qquad\qquad\qquad (2.11)$$

where λ is the Lame constant, calculated with:

$$\lambda = \frac{v \cdot E}{(1 + v) \cdot (1 - 2 \cdot v)} \qquad\qquad\qquad (2.12)$$

where E is the elasticity modulus and v is the Poisson's ratio ($v = 0.30$).

Table 2.5. Calculated elastic constants at room temperature for AISI 304 and AISI 347.

Material	E [GPa]	λ [GPa]	µ [GPa]	c_{11} [GPa]	c_{12} [GPa]	c_{44} [GPa]
AISI 304	200	115.385	76.92	269.231	115.385	76.9231
AISI 347	193	111.346	74.23	259.808	111.346	74.2308

CHAPTER 3

EXPERIMENTAL RESULTS

In this chapter the detailed experimental results are described. They refer successively to optical microscopy observations, microhardness measurements, tensile mechanical testing, scanning electron microscopy observations and transmission electron microscopy observations of the various materials and specimens.

3.1 OPTICAL MICROSCOPY OBSERVATIONS

3.1.1 Unirradiated test materials

The weld geometry and the extension of the heat-affected zone of the weld were determined by measuring the grain size distribution as a function of the distance from the fusion line.

The microstructure of base metals (BM) of both the AISI 347 and the AISI 304, unaffected by the thermal cycles upon welding, is composed of grains that contain a lot of twins (Figure 3.1). Due to the heating during welding, in the corresponding heat affected zones (HAZ) the density of twins is smaller (Figure 3.2). The weld metals exhibit a two phase dendritic structure (austenite and ferrite), oriented perpendicular to the fusion line (Figure 3.2.). The results of grain size measurements are presented in Table 3.1.
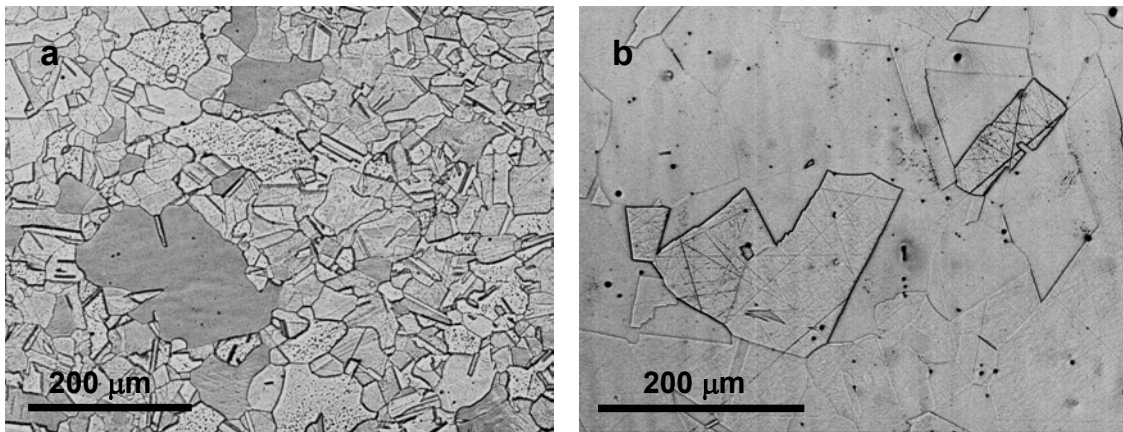
Figure 3.1. Optical microscopy images of a) AISI 347 and b) AISI 304 base metals.
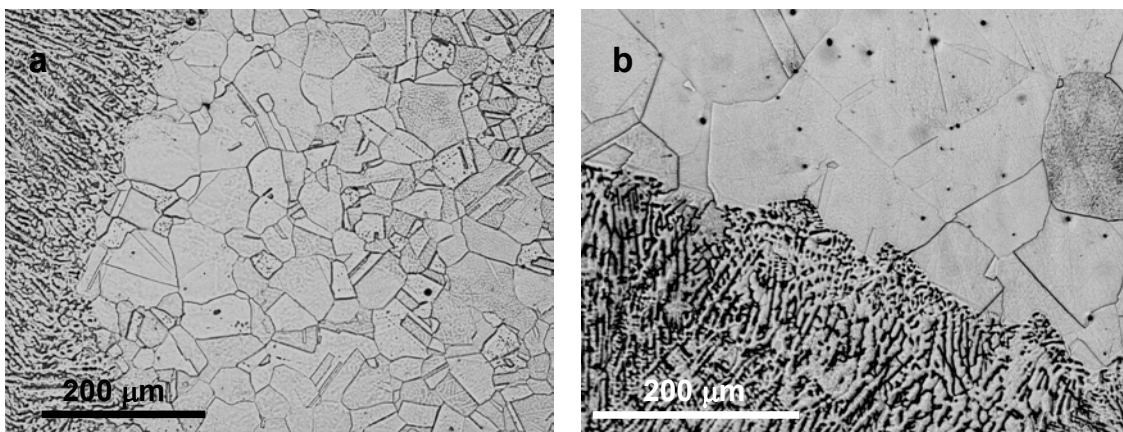
Figure 3.2. Optical microscopy images of a) AISI 347 and b) AISI 304 heat affected zones.

Table 3.1. Results of grain size measurements on the unirradiated test materials.

Measurement zone	AISI 347 [μm]	AISI 304 [μm]
HAZ	60	65
BM	40	50

The grain size presents a significant variation as a function of the distance from the fusion line. It appears much higher in the HAZ, about 60 – 65 μm, with respect to the BM (40 – 50 μm). No significant difference is observed between the grain sizes of the two materials. The width of the HAZ is approximately 600 μm in both materials.

3.1.2 In-service material

The microstructure of the low dose base material, far away from the fusion line, is typical of that of an austenitic stainless steel, with a lot of twins inside the grains and some precipitates (Figure 3.3.a). Thermal cycles upon welding influenced the grain size (Figure 3.3.b) in the HAZ, as compared to the BM. The measured grain size in the low dose in-service material, close to the fusion line, and far away from the fusion line, is listed in Table 3.2. The microstructure of the high dose in-service material (Block B) presents no significant difference in comparison to the low dose in-service material (Figure 3.4.a for the BM, and Figure 3.4.b for the HAZ). Results of grain size measurements on the high dose in-service material are presented in Table 3.2. The width of the HAZ couldn't be precisely determined.
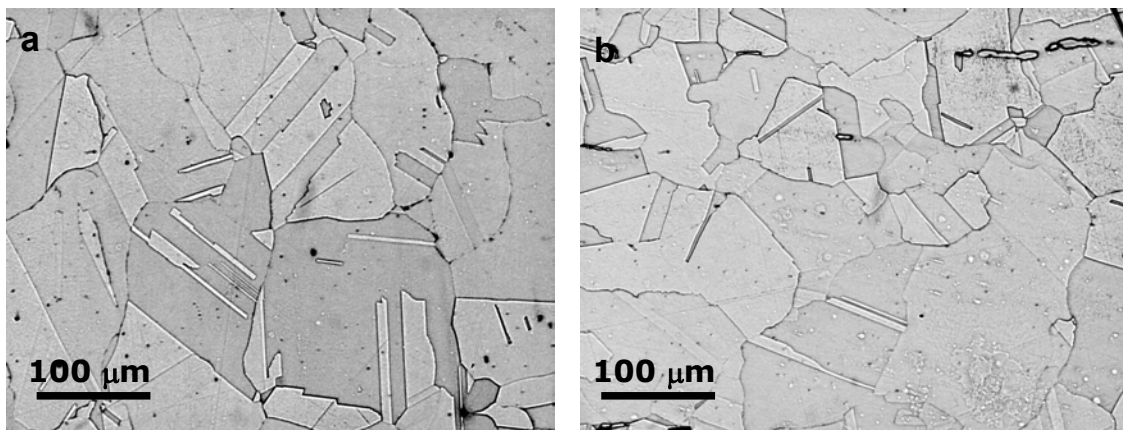
Figure 3.3. Low dose in-service material (Block A): a) base material; b) heat-affected zone.
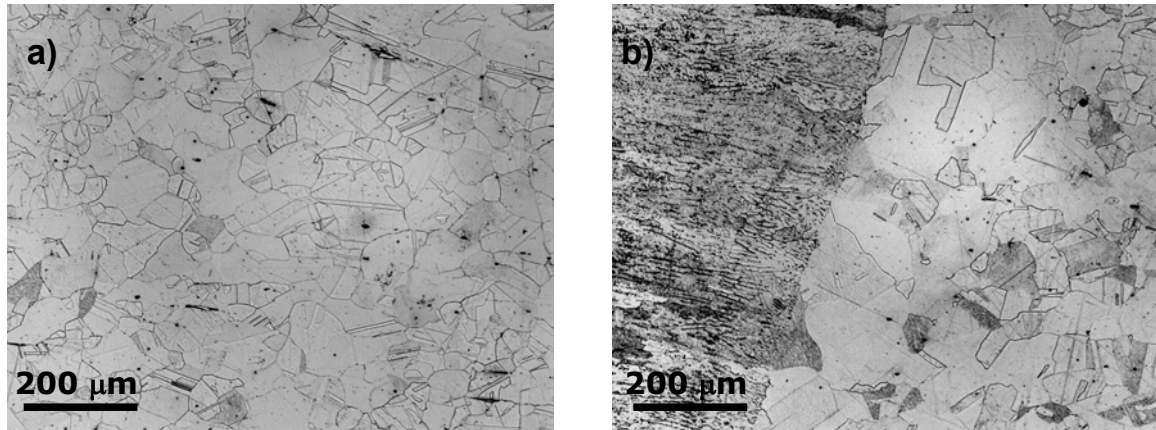
Figure 3.4. High dose in-service material (Block B): a) base material; b) heat-affected zone.

Table 3.2. Results of grain size measurements on the in-service material.

Block	Base metal [μm]	Heat-affected zone [μm]
Low dose (A)	106.8	151
High dose (B)	106.8	127

An increase in the grain size close to the fusion line can be observed, as compared to the values far away from the fusion line. The grain size in the HAZ of the high dose in-service material appears to be smaller in comparison to the low dose in-service material. The grain size far away from the fusion line is the same for both the low dose and high dose materials. The difference in the grain size measured in the heat affected zones of both materials could be due to the small width of the HAZ, yielding bad statistics, rather than to irradiation (the grain size in the base materials is the same for the two dose levels).

3.2 MECHANICAL PROPERTIES

3.2.1 Microhardness measurements

3.2.1.1 Unirradiated test materials

The microhardness variations are presented in Figure 3.5 for the AISI 347 and in Figure 3.6 for the AISI 304, as a function of the distance from the fusion line and from the middle of the weld, respectively. In both figures the three series of symbols refer to three series of in-line measurements. The size of the indentation is always smaller than the grain size.

It can be seen that the microhardness versus distance from the fusion line presents some variations because of the grain size evolution (it is slightly higher in the HAZ with respect to the BM, at least for AISI 304), but does not allow the determination of the width of the HAZs.
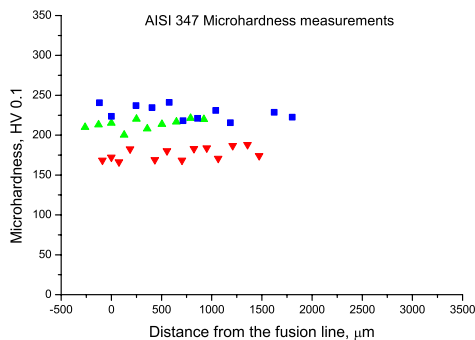
Figure 3.5. Microhardness HV 0.1 for the AISI 347 as a function of the distance from the fusion line.
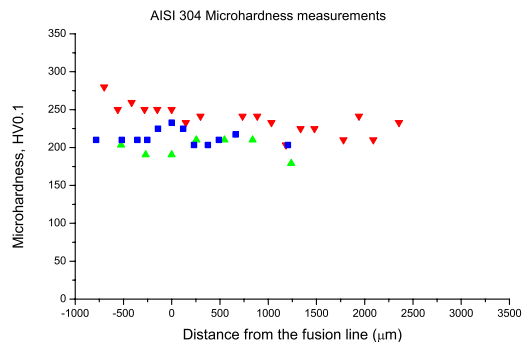
Figure 3.6. Microhardness HV 0.1 for the AISI 304 as a function of the distance from the weld centre.

3.2.1.2 In-service material

The microhardness values are listed in Table 3.3 for the low dose and high dose in-service blocks and reported as a function of the distance from the fusion line in Figure 3.7.

It can be seen in Table 3.3 and Figure 3.7 that there is no significant difference in the microhardness of the HAZ as compared to the values obtained for the BM and the weld metal (WM). However, the microhardness of the high dose material appears significantly higher than the one of the low dose material, whatever the region considered (BM, HAZ, and WM).

Table 3.3. Microhardness measurements on the in-service material.

Material	BM [HV0.1]	HAZ [HV0.1]	WM [HV0.1]
Low dose (Block A)	230	222	233
High dose (Block B)	256	256	265

a)   b)
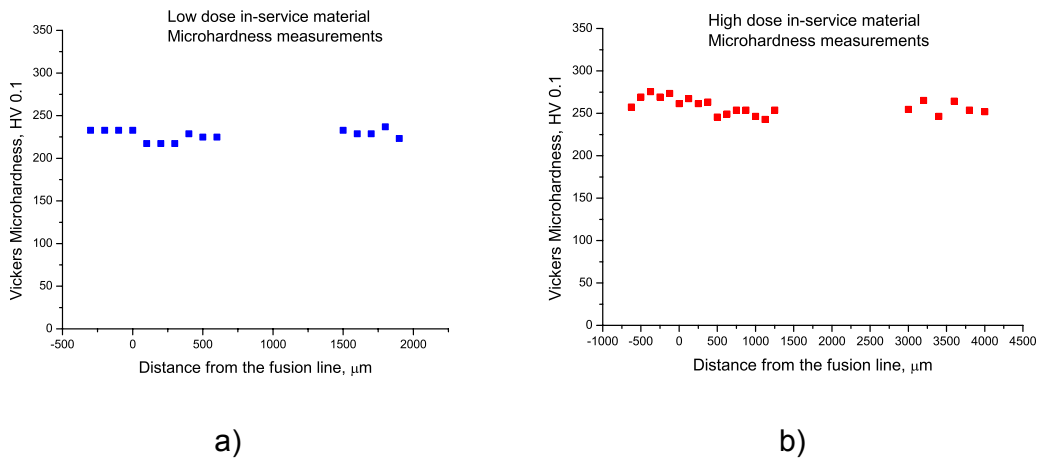
Figure 3.7. Microhardness HV-0.1 as a function of the distance from the fusion line for the in-service material: a) low dose (Block A), and b) high dose (Block B).

3.2.2 Tensile mechanical testing

Following the procedure described in Chapter 2, tensile tests were performed on base materials and heat-affected zones of the various materials, in both the unirradiated and irradiated states.

3.2.2.1 Unirradiated test materials

3.2.2.1.1 Base materials

A. Tensile stress-strain curves

As a reference, tensile specimens from the base materials were tested at room temperature and at around 573 K, using a strain rate of 5×10^{-4} s^{-1}.

Typical tensile true stress-true strain curves obtained at both deformation temperatures for the BMs are presented in Figure 3.8 for the AISI 304 and the AISI 347. Corresponding mechanical parameter values are reported in Table 3.4.

As it can be seen in Figure 3.8 and also in Table 3.4, the yield strength (YS), the uniform tensile strength (UTS) and the uniform elongation (UE) are decreasing with increasing temperature. The measured YS and UTS values are comparable to those found in the literature, for both materials. From the experimental results (as well as from the literature data), one observes that the YS of AISI 347 is higher than that of AISI 304, while the UTS and the UE of AISI 304 present larger values than those of AISI 347.

The mean deviation values are very high because of the small size of the specimens, the specimen preparation (mechanical polishing caused an alteration of the parallelism of main surfaces), and the specimen alignment in the deformation machine. For the first tests, the specimens were preloaded with a force of 10 N. Because of the large scatter in the results, the subsequent tests were performed without preloading, neither mechanical polishing of the surfaces.

a)   b)
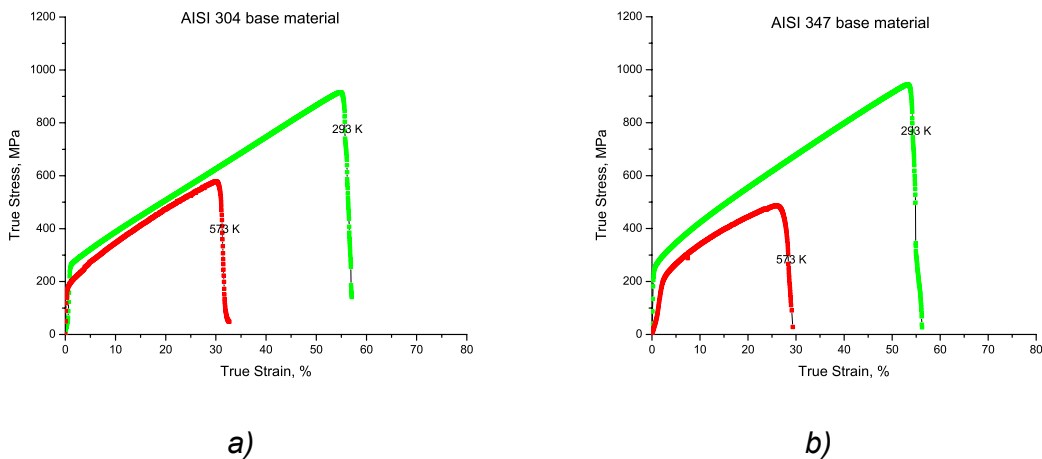
Figure 3.8. True stress – true strain dependence for (a) AISI 304 and (b) AISI 347 base materials, at the two different testing temperatures.

Table 3.4. Average tensile properties of the two base test materials.

Tensile properties		AISI 347		AISI 304	
	Material	*293K*	*573K*	*293K*	*573K*
YS [MPa]	True	244	214	215	160
	Eng	244	203	200	160
	Deviation	*± 10 %*	*± 20 %*	*± 15 %*	*± 20 %*
UTS [MPa]	True	890	420	935	618
	Eng	542	345	535	443
	Deviation	*± 10 %*	*± 25 %*	*± 15 %*	*± 25 %*
UE [%]	True	48	19	53	33
	Eng	62	21	73	39
	Deviation	*± 6 %*	*± 5 %*	*± 5 %*	*± 4 %*

YS = yield strength
UTS = uniform tensile strength
UE = uniform elongation

B. Strain rate dependence

Tensile tests on base materials were performed using four different strain rates, namely 8.7×10^{-3}, 7.4×10^{-4}, 1.55×10^{-4} and 5×10^{-4} s^{-1}, at both deformation temperatures. The strain rate dependence of the YS, UTS, and UE are reported in Figures 3.9, 3.10, and 3.11, respectively. No significant dependence of the mechanical properties on the strain rate was evidenced.

a)   b)
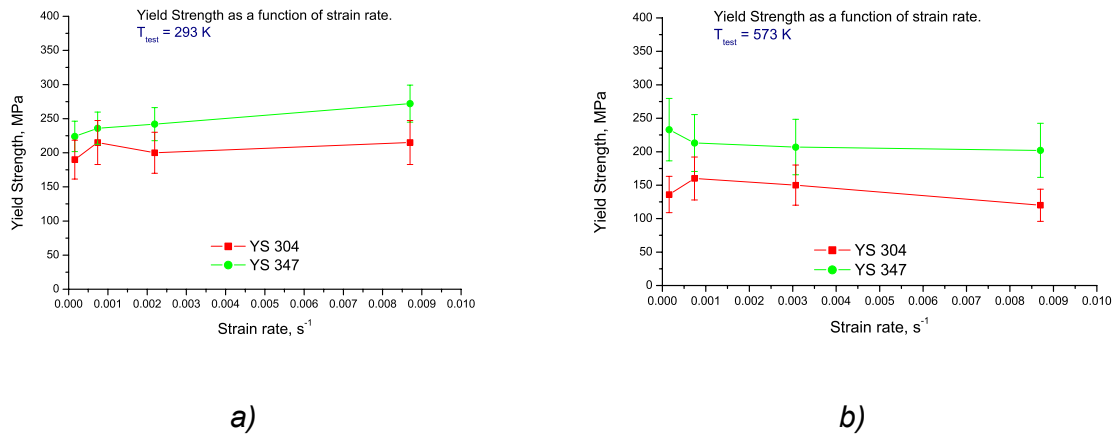
Figure 3.9. Strain rate dependence of the yield strength in the case of AISI 304 and AISI 347 base materials at a) 293 K and b) 573 K.

a)   b)
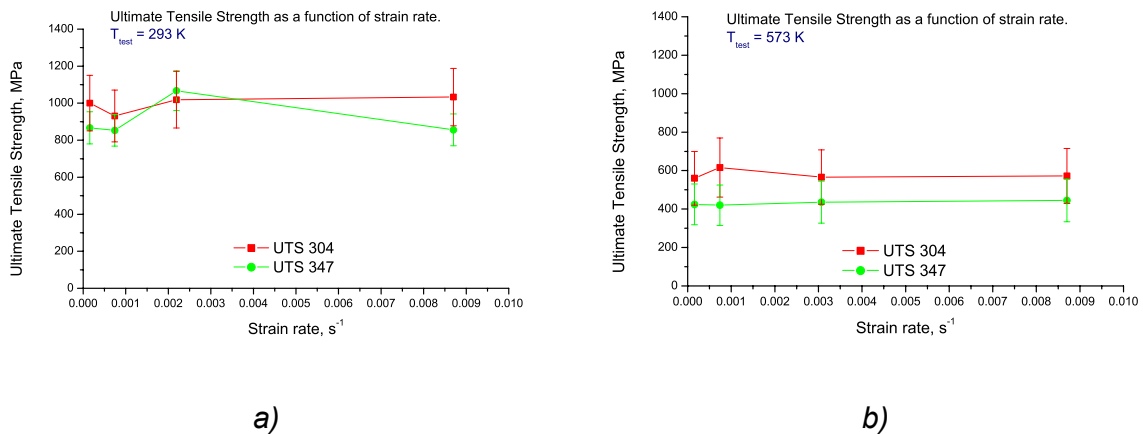
Figure 3.10. Strain rate dependence of the ultimate tensile strength in the case of AISI 304 and AISI 347 base materials at a) 293 K and b) 573 K.

59

a)   b)
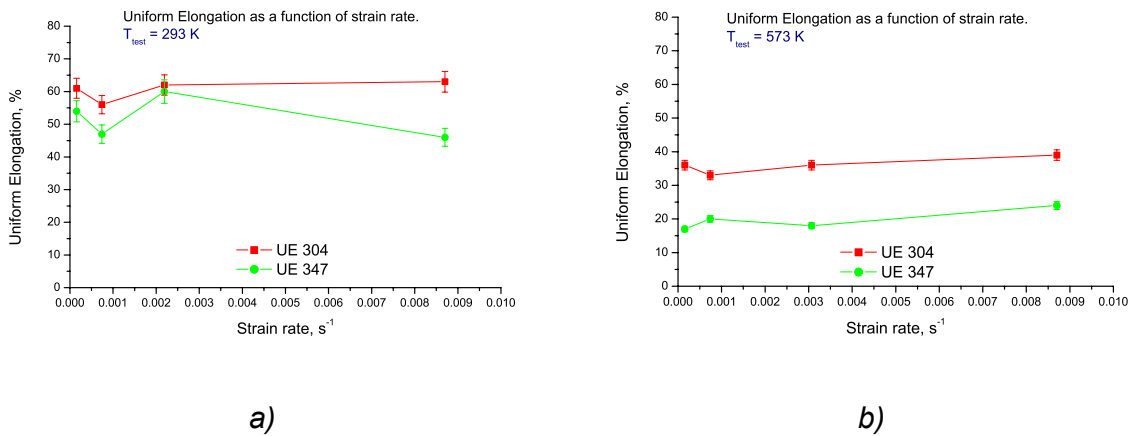
*Figure 3.11. Strain rate dependence of the uniform elongation in the case of AISI 304
and AISI 347 base materials at a) 293 K and b) 573 K.*

3.2.2.1.2 Heat-affected zones

A. Tensile stress-strain curves

Five tensile specimens with the PIREX geometry were cut out from the heat-affected
zone of each test weld material, according to the procedure described in
section 2.3.1.

Typical tensile true stress-true strain curves obtained at 293 K and 573 K for
AISI 304 and AISI 347 are presented in Figures 3.12 and 3.13, respectively. In these
figures the number 1 refers to the specimen closest to the fusion line, while the
number 5 refers to the specimen cut out relatively far away from the fusion line (see
Figure 2.4).

The yield strength, the ultimate tensile strength and the uniform elongation variations
with the distance from the fusion line, for both materials tested at 293 K and 573 K,
are reported in Figures 3.14, 3.15, and 3.16, respectively. Corresponding values are
also summarised in Table 3.5 for testing at room temperature and in Table 3.6 for
high temperature testing.

The YS of AISI 347 HAZ is comparable to that of AISI 304 HAZ at both testing
temperatures, while the UTS and the UE values of AISI 304 HAZ are in most cases
significantly larger than those of AISI 347 HAZ, at least at room temperature. At
573 K both sets of values obtained for AISI 304 HAZ appear comparable to those
obtained for AISI 347 HAZ. The YS of the HAZ presents a strong increase with
respect to that of the BM and that of the WM, for both materials, at both deformation
temperatures. At room temperature the UTS and UE present an increase as the
distance from the fusion line increases for both materials. The UTS and UE of the
HAZ present no significant variation with the distance from the fusion line at high
temperature testing, whatever the material considered.

a)   b)
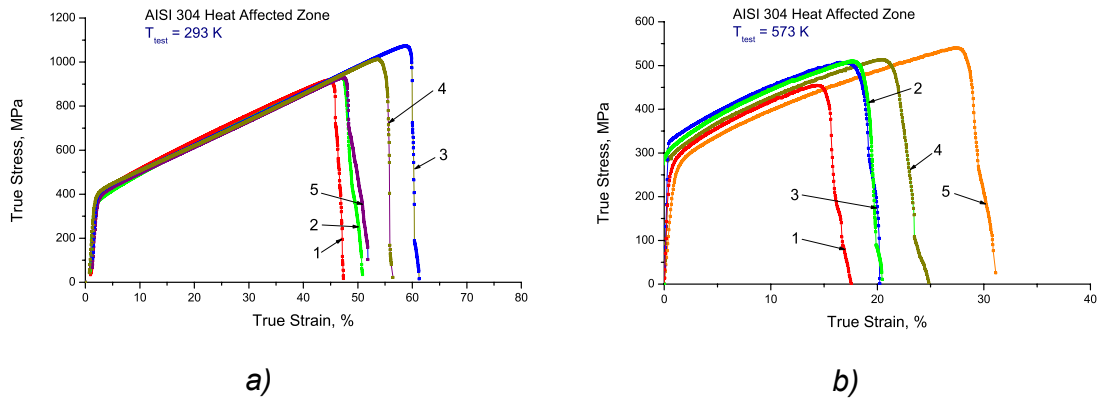
Figure 3.12. True stress – true strain dependence for AISI 304 HAZ at a) 293 K and b) 573 K (specimen 1: close to the fusion line, specimen 5: far away from the fusion line).
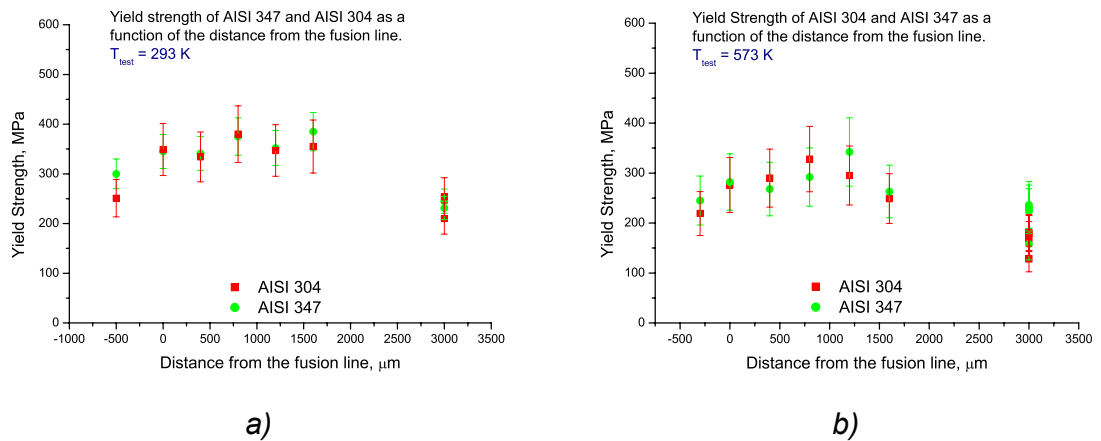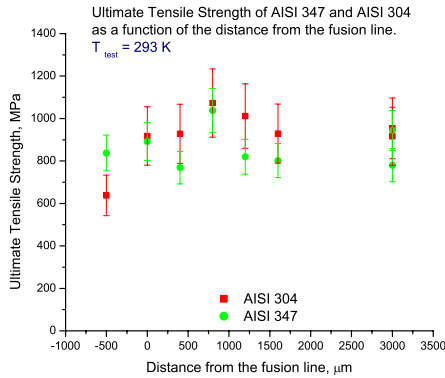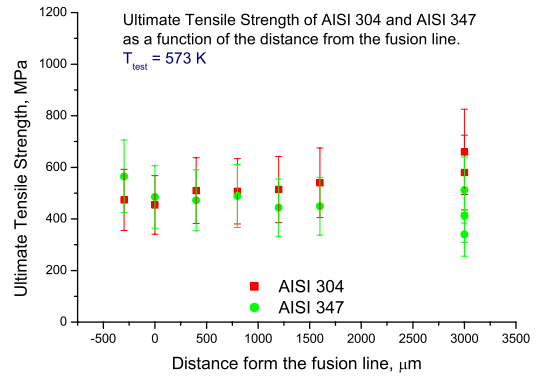

a)   b)
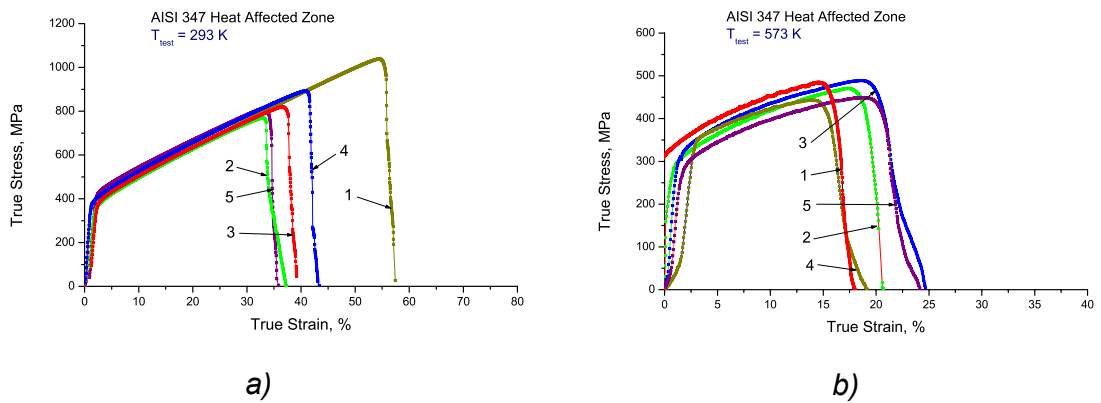
Figure 3.13. True stress – true strain dependence for AISI 347 HAZ at a) 293 K and b) 573 K (specimen 1: close to the fusion line, specimen 5: far away from the fusion line).

a)   b)

Figure 3.14. Yield strength of AISI 304 and AISI 347 as a function of the distance from the fusion line at a) 293 K and b) 573 K.

a)

b)

Figure 3.15. Ultimate tensile strength of AISI 304 and AISI 347 as a function of the distance from the fusion line at a) 293 K and b) 573 K.
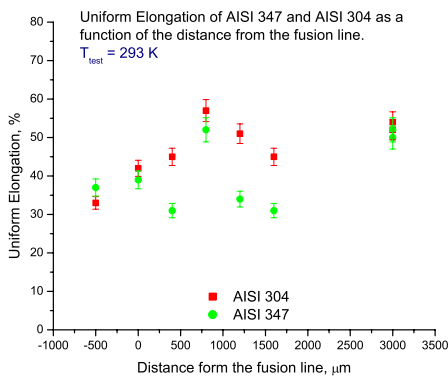
a)
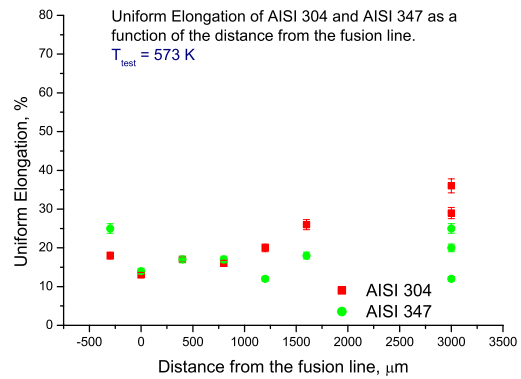
b)

Figure 3.16. Uniform elongation of AISI 304 and AISI 347 as a function of the distance from the fusion line at a) 293 K and b) 573 K.

Table 3.5. Tensile properties of the heat affected zones of AISI 347 and AISI 304 at 293 K.

| Material	Sample	YS [MPa]		UTS [MPa]		UE [%]	
		True	*Eng*	*True*	*Eng*	*True*	*Eng*
AISI 347	**WM**	300	300	838	567	37	46
	1	345	344	892	595	39	49
	2	341	332	769	555	31	37
	3	375	371	1038	605	52	70
	4	352	344	820	570	34	41
	5	385	375	802	577	31	38
AISI 304	**WM**	251	251	638	494	33	39
	1	349	344	918	591	42	54
	2	334	328	928	582	45	57
	3	380	371	1073	600	57	77
	4	347	340	1012	594	51	69
	5	355	343	929	581	45	58

YS = yield strength
UTS = uniform tensile strength
UE = uniform elongation
WM = weld metal
Specimen 1: close to the fusion line, specimen 5: far away from the fusion line.
The mean deviation values are of the same order of magnitude as in Table 3.4.

Table 3.6. Tensile properties of the heat affected zones of AISI 347 and AISI 304 at 573 K.

Material	Sample	YS [MPa]		UTS [MPa]		UE [%]	
		True	*Eng*	*True*	*Eng*	*True*	*Eng*
AISI 347	**WM**	245	245	565	438	25	28
	1	282	285	485	420	14	17
	2	268	255	472	397	17	18
	3	292	289	489	408	17	19
	4	342	329	444	387	12	13
	5	263	260	449	375	18	19
AISI 304	**WM**	219	218	474	397	18	20
	1	276	255	454	395	13	14
	2	290	288	510	428	17	18
	3	328	327	507	430	16	17
	4	295	294	514	420	20	22
	5	249	243	540	412	26	30

YS = yield strength
UTS = uniform tensile strength
UE = uniform elongation
WM = weld metal
Specimen 1: close to the fusion line, specimen 5: far away from the fusion line.
The mean deviation values are of the same order of magnitude as in Table 3.4.

B. Strain hardening

The typical strain hardening behaviour as a function of true strain is shown in Figure 3.17 in the case of AISI 304 HAZ tested at 293 K. The strain hardening was calculated as $\Delta\sigma/\Delta\varepsilon$ all along the true stress-true strain curve. The strain hardening appears almost constant in the plastic deformation region. Figure 3.18 presents the strain hardening dependence on the distance from the fusion line, at 293 K and 573 K, for both materials. It can be seen that the strain hardening in the HAZ is higher than in the BM and in the WM, for both materials and at both testing temperatures.
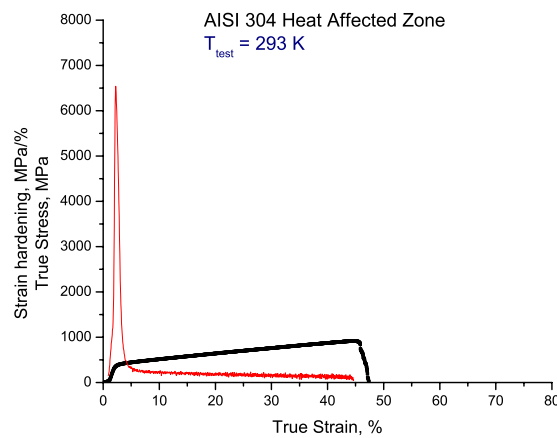
Figure 3.17. Strain hardening versus true strain for AISI 304 HAZ tested at 293 K.

a)   b)
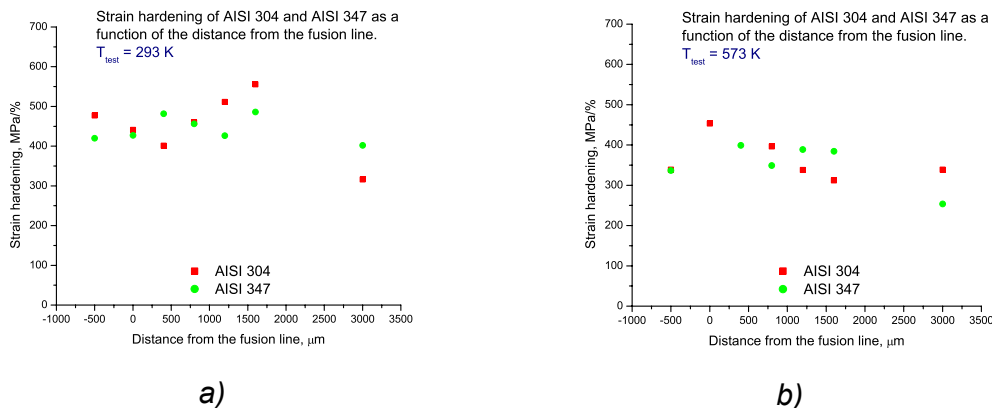
Figure 3.18. Strain hardening of AISI 304 and AISI 347 as a function of the distance from the fusion line at a) 293 K and b) 573 K.

3.2.2.2 Irradiated test materials

3.2.2.2.1 Test materials irradiated to 0.3 dpa

Series of four specimens, cut out at four different distances from the fusion line, were tested for both AISI 304 and AISI 347 materials. Typical tensile true stress–true strain curves obtained at 293 K and 573 K are reported in Figure 3.19 for AISI 304 and in Figure 3.20 for AISI 347. In these figures, the number 1 refers to the specimen that is the closest to the fusion line, while the number 4 refers to a specimen cut out relatively far away from the fusion line (see Figure 2.4). The values of YS, UTS, and UE, as deduced from the true stress–true strain tensile curves, are reported as a function of the distance from the fusion line in Figures 3.21, 3.22, and 3.23, respectively. The corresponding true and engineering values are also summarised in Table 3.7 for testing at room temperature and in Table 3.8 for the high temperature testing.

The YS of AISI 304 HAZ presents slightly larger values than that of AISI 347 HAZ, at both testing temperatures. The UTS and the UE values of AISI 304 show no systematic, interpretable difference with respect to those of AISI 347, at both testing temperatures. The stress and elongation values at high temperature are smaller than at room temperature. YS values appear slightly higher close to the fusion line than far away from the fusion line, at both testing temperatures, at least for AISI 304. Elongation values appear much lower close to the fusion line than far away from the fusion line, for both materials and at both testing temperatures.

The YS values in the case of AISI 304 tested at room temperature are varying from 682 MPa close to the fusion line to 613 MPa far away from the fusion line. AISI 347 presents a different behaviour, as the YS values are increasing from 508 MPa close to the fusion line to 574 MPa far away from the fusion line. The UTS of AISI 347 tested at room temperature, increases from 845 MPa close to the fusion line to 956 MPa far away from the fusion line. The UTS of AISI 304 tested at room temperature presents no important variation with the distance from the fusion line, ranging between 960 MPa at the fusion line to 922 MPa far away from the fusion line. The UE of AISI 304 tested at room temperature increases from 16 % close to the fusion line to 25 % far away from the fusion line. In the case of AISI 347 the increase in UE is less important, from 21 % close to the fusion line to 29 % far away from the fusion line.

At high temperature test the YS strength presents the same behaviour for both materials. For AISI 304 the YS decreases from 590 MPa to 488 MPa, as the distance from the fusion line increases. In the case of AISI 347, the variation is not so significant, decreasing from 479 MPa close to the fusion line to 446 MPa far away from the fusion line. The UTS of AISI 304 varies from 652 MPa close to the fusion line to 660 MPa far away from the fusion line, while the UTS of AISI 347 presents a larger variation, from 686 MPa close to the fusion line to 590 MPa far away. The UE of AISI 304 increases from 5 % close to the fusion line to 8 % far away from the fusion line, while the UE of AISI 347 presents no significant variation, ranging from 6 to 8 %.

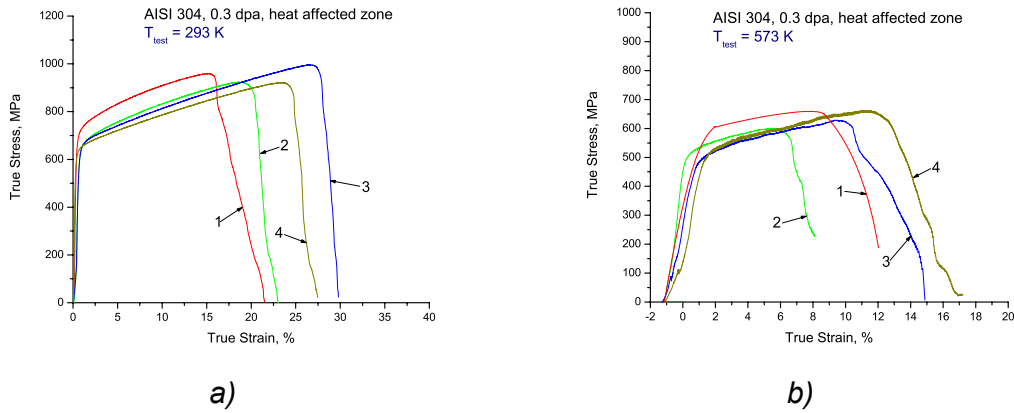a)   b)

Figure 3.19. True stress – true strain dependence for AISI 304 HAZ irradiated up to 0.3 dpa and tested at a) 293 K and b) 573 K (specimen 1: close to the fusion line, specimen 4: away from the fusion line).
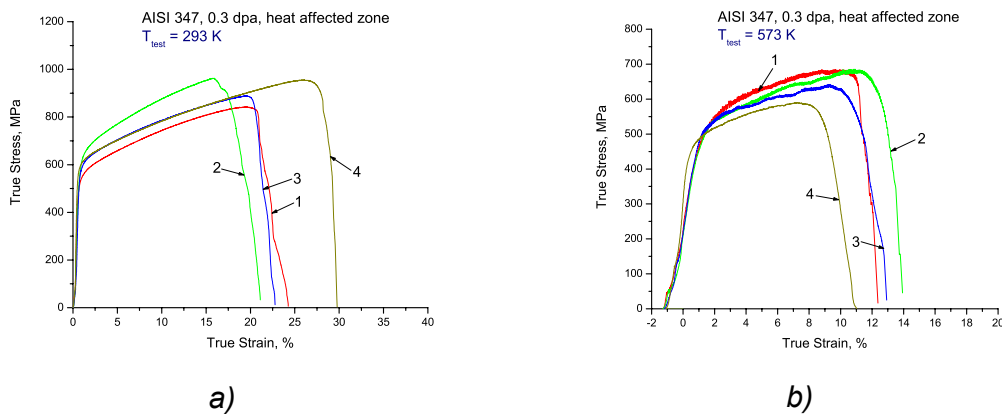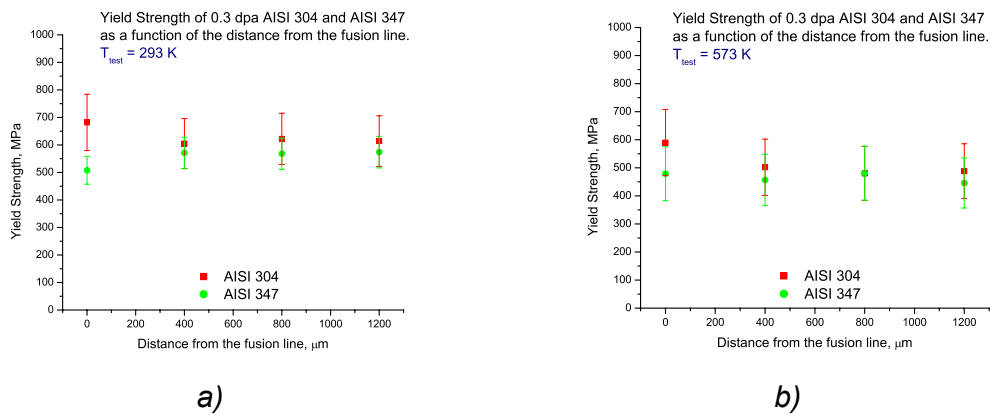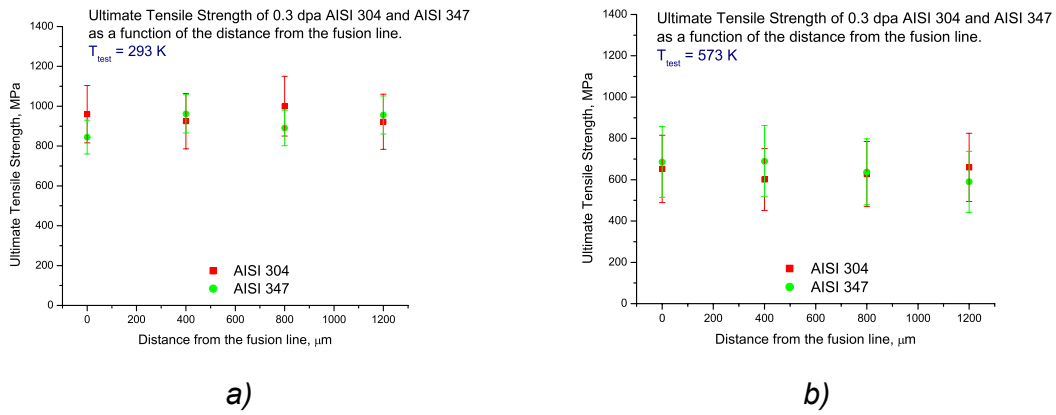

a)   b)

Figure 3.20. True stress – true strain dependence for AISI 347 HAZ irradiated up to 0.3 dpa and tested at a) 293 K and b) 573 K (specimen 1: close to the fusion line, specimen 4: away from the fusion line).

a)   b)

Figure 3.21. Yield strength of 0.3 dpa AISI 304 and AISI 347 as a function of the distance from the fusion line at a) 293 K and b) 573 K.

Figure 3.22. Ultimate tensile strength of 0.3 dpa AISI 304 and AISI 347 as a function of the distance from the fusion line at a) 293 K and b) 573 K.
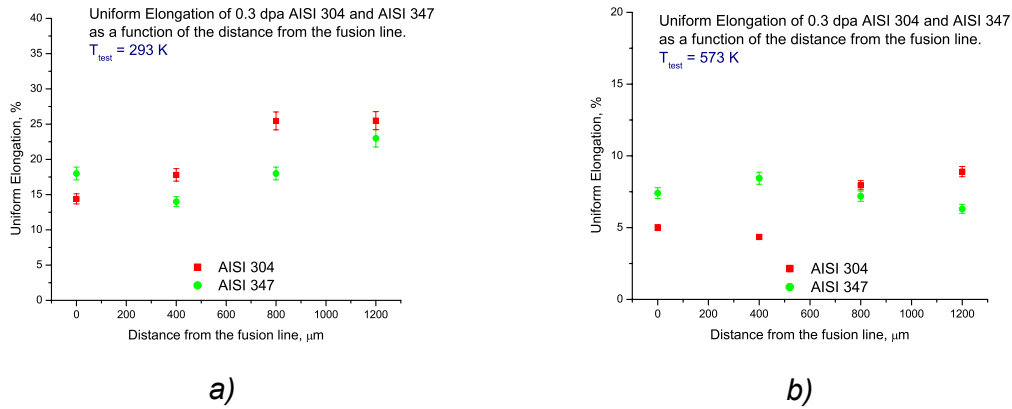
Figure 3.23. Uniform elongation of 0.3 dpa AISI 304 and AISI 347 as a function of the distance from the fusion line at a) 293 K and b) 573 K.

Table 3.7. Tensile properties at 293 K of the heat affected zones of AISI 347 and AISI 304 irradiated to 0.3 dpa.

Material	Sample	YS [MPa]		UTS [MPa]		UE [%]	
		True	*Eng*	*True*	*Eng*	*True*	*Eng*
AISI 347	1	508	502	845	700	21	23
	2	571	568	962	822	16	18
	3	568	565	890	735	21	23
	4	574	570	956	745	29	33
AISI 304	1	682	677	960	830	16	17
	2	605	600	925	770	21	23
	3	622	620	1000	780	29	33
	4	613	608	922	736	25	29

YS = yield strength
UTS = uniform tensile strength
UE = uniform elongation
Specimen 1: close to the fusion line, specimen 4: far away from the fusion line.
The mean deviation values are of the same order of magnitude as in Table 3.4.

Table 3.8. Tensile properties at 573 K of the heat affected zones of AISI 347 and AISI 304 irradiated to 0.3 dpa.

Material	Sample	YS [MPa]		UTS [MPa]		UE [%]	
		True	*Eng*	*True*	*Eng*	*True*	*Eng*
AISI 347	**1**	479	434	686	619	7	8
	2	457	442	689	617	8	9
	3	480	483	638	583	7	8
	4	446	446	590	550	6	7
AISI 304	**1**	590	587	652	610	5	6
	2	502	502	601	568	4	5
	3	480	470	628	572	7	8
	4	488	487	660	590	8	9

YS = yield strength
UTS = uniform tensile strength
UE = uniform elongation
Specimen 1: close to the fusion line, specimen 4: far away from the fusion line.
The mean deviation values are of the same order of magnitude as in Table 3.4.

3.2.2.2.2 Test materials irradiated to 1 dpa

Series of four specimens, cut out at four different distances from the fusion line, were tested for both AISI 304 and AISI 347 materials. Typical tensile true stress–true strain curves obtained at 293 K and 573 K are reported in Figure 3.24 for AISI 304 and in Figure 3.25 for AISI 347. In these figures, the number 1 refers to the specimen that is the closest to the fusion line, while the number 4 refers to a specimen cut out relatively far away from the fusion line (see Figure 2.4). The values of YS, UTS, and UE, as deduced from the true stress–true strain tensile curves, are reported as a function of the distance from the fusion line in Figures 3.26, 3.27, and 3.28, respectively. The corresponding true and engineering values are also summarised in Table 3.9 for testing at room temperature and in Table 3.10 for the high temperature testing.

The YS and UTS of AISI 304 HAZ present slightly larger values than those of AISI 347 HAZ, at both testing temperatures. The UE values of AISI 304 show smaller values with respect to those of AISI 347, at both testing temperatures. The stress and elongation values at high temperature are smaller than at room temperature. YS values appear slightly higher close to the fusion line than far away from the fusion line, at both testing temperatures, at least for AISI 304. There is no significant dependence of the UTS values on the distance from the fusion line for both materials and at both testing temperatures, with the exception of AISI 347 tested at 573 K, which presents slightly higher UTS values close to the fusion line with respect to those far away from the fusion line. Elongation values appear much lower close to the fusion line than far away from the fusion line, for both materials and at both testing temperatures.

The YS values in the case of AISI 304 tested at room temperature are varying from 683 MPa close to the fusion line to 619 MPa far away from the fusion line. AISI 347 presents a different behaviour, as the values are increasing from 645 MPa close to the fusion line to 775 MPa far away from the fusion line. The UTS of AISI 347 tested at room temperature, increases from 909 MPa close to the fusion line to 1024 MPa far away from the fusion line. The UTS of AISI 304 increases from 891 MPa close to the fusion line to about 900 MPa far away from the fusion line. The UE of AISI 304 tested at room temperature increases from 14 % close to the fusion line to 20 % far away from the fusion line. In the case of AISI 347 the UE increases from 13 % close to the fusion line to 19 % far away from the fusion line.

At high temperature the YS presents the same behaviour for both materials. For AISI 304 the YS increases from 460 MPa to 510 MPa, as the distance from the fusion line increases. In the case of AISI 347, the values increase from 481 MPa close to the fusion line to 519 MPa far away from the fusion line. The UTS for AISI 304 presents the same values for the specimen close to the fusion line and the one far away, 550 MPa, while the UTS of AISI 347 presents a larger variation, decreasing from 672 MPa close to the fusion line to 567 MPa far away. The UE of AISI 304 increases from 5 % close to the fusion line to 10 % far away from the fusion line, while the UE of AISI 347 decreases from 10 % close to the fusion line to about 6 % far away from the fusion line.

a)   *b)*
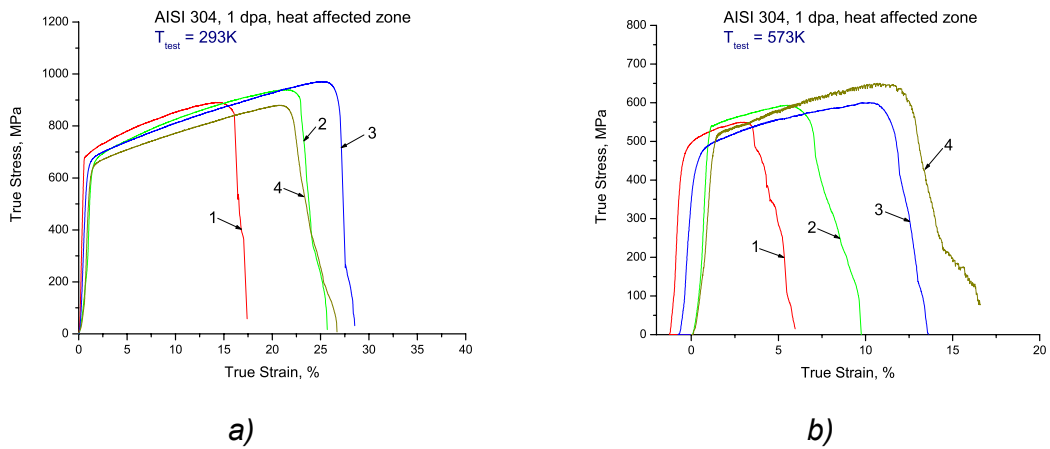
Figure 3.24. True stress – true strain dependence for AISI 304 HAZ irradiated up to 1 dpa and tested at a) 293 K and b) 573 K (specimen 1: close to the fusion line, specimen 4: away from the fusion line).
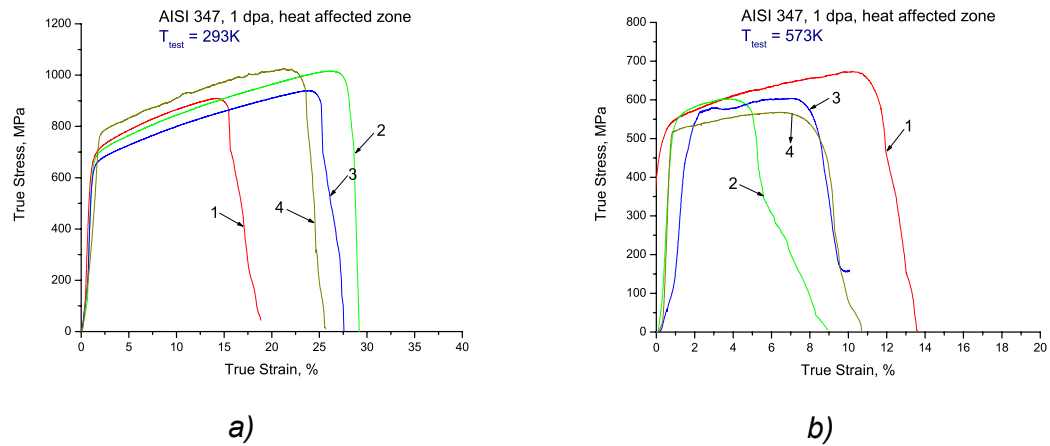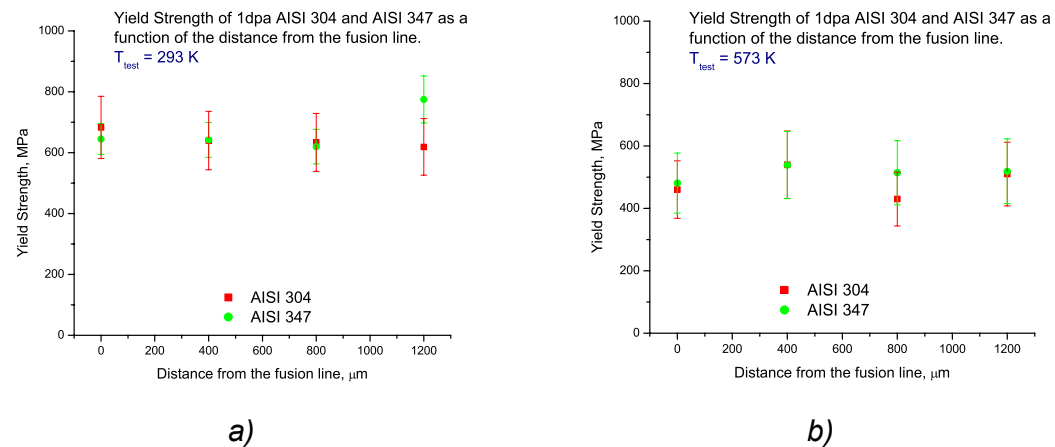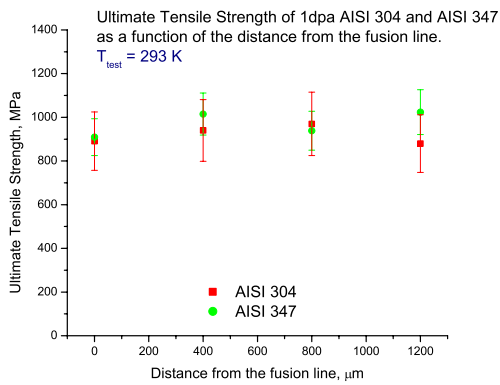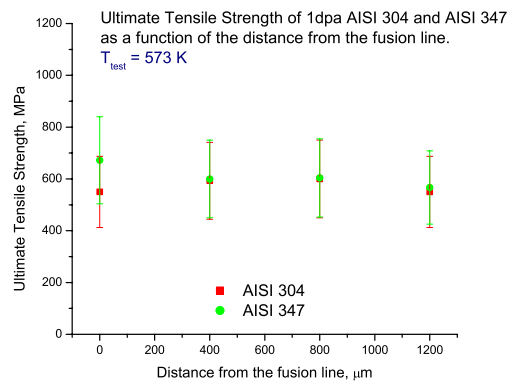

a)   *b)*

Figure 3.25. True stress – true strain dependence for AISI 347 HAZ irradiated up to 1 dpa and tested at a) 293 K and b) 573 K (specimen 1: close to the fusion line, specimen 4: away from the fusion line).

a)   *b)*

Figure 3.26. Yield strength of 1 dpa AISI 304 and AISI 347 as a function of the distance from the fusion line at a) 293 K and b) 573 K.

a)   b)

Figure 3.27 Ultimate tensile strength of 1 dpa AISI 304 and AISI 347 as a function of the distance from the fusion line, at a) 293 K and b) 573 K.
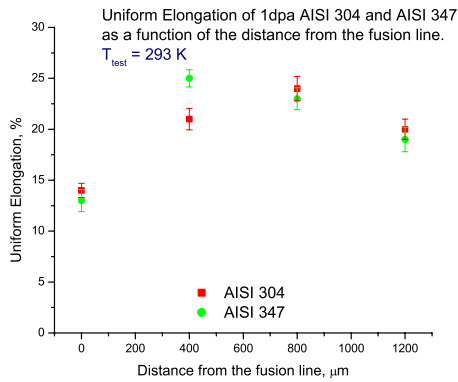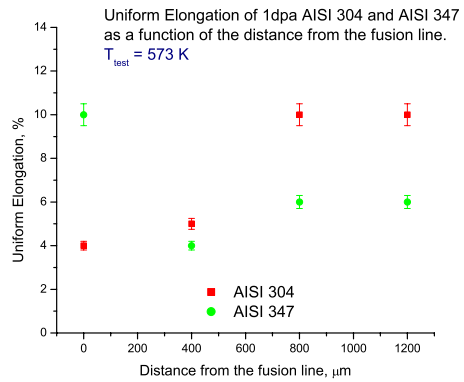
a)   b)

Figure 3.28. Uniform elongation of 1 dpa AISI 304 and AISI 347 as a function of the distance from the fusion line, at a) 293 K and b) 573 K.

Table 3.9. Tensile properties at 293 K of the heat affected zones of AISI 347 and AISI 304 irradiated to 1dpa.

Material	Sample	YS [MPa]		UTS [MPa]		UE [%]	
		True	*Eng*	*True*	*Eng*	*True*	*Eng*
AISI 347	**1**	645	636	909	790	13	14
	2	642	639	1015	790	25	26
	3	620	613	939	744	23	25
	4	775	759	1024	836	19	20
AISI 304	**1**	683	678	891	775	14	14
	2	640	628	939	765	21	21
	3	634	628	970	760	24	25
	4	619	606	879	718	20	21

YS = yield strength
UTS = uniform tensile strength
UE = uniform elongation
Specimen 1: close to the fusion line, specimen 4: far away from the fusion line.
The mean deviation values are of the same order of magnitude as in Table 3.4.

Table 3.10. Tensile properties at 573 K of the heat affected zones of AISI 347 and AISI 304 irradiated to 1dpa.

Material	Sample	YS [MPa]		UTS [MPa]		UE [%]	
		True	*Eng*	*True*	*Eng*	*True*	*Eng*
AISI 347	**1**	481	488	672	609	10	10
	2	539	533	600	580	4	3
	3	514	495	604	566	6	6
	4	519	515	567	534	6	6
AISI 304	**1**	460	465	550	534	5	4
	2	540	534	593	562	4	5
	3	430	432	600	543	10	10
	4	510	507	550	584	10	10

YS = yield strength
UTS = uniform tensile strength
UE = uniform elongation
Specimen 1: close to the fusion line, specimen 4: far away from the fusion line.
The mean deviation values are of the same order of magnitude as in Table 3.4.

3.2.2.3 In-service material

Specimens from the heat affected zones of the in-service material were prepared and tensile tested in the same conditions as the unirradiated and irradiated test materials. For a given position with respect to the fusion line, specimens with different accumulated doses were available. The accumulated dose varied between $1.3 \cdot 10^{-5}$ dpa and $1.3 \cdot 10^{-4}$ dpa for the low dose in-service material (Block A), and between 0.12 dpa and 0.3 dpa for the high dose in-service material (Block B).

3.2.2.3.1 In-service material irradiated to low dose (Block A)

Typical tensile true stress–true strain curves, as obtained in the HAZ at room temperature and high temperature for three different doses, are shown in Figure 3.29. Values of the YS, UTS, and UE, as deduced from the tensile true stress–true strain curves obtained at both testing temperatures are reported in Figures 3.30 – 3.32. These values are also summarised in Table 3.11 for testing at room temperature and in Table 3.12 for the high temperature testing. In these tables the number 1 refers to the specimen that is the closest to the fusion line, while the number 7 refers to the specimen cut out relatively far away from the fusion line.

It can be seen that the very small dose variations within Block A have a small influence on the tensile properties both at room temperature (Figure 3.29.a) and at high temperature (Figure 3.29.b).

A significant decrease in the YS values with increasing the distance from the fusion line can be seen at both testing temperatures. At room temperature the UTS values show a slight decrease with decreasing the distance from the fusion line, while at high temperature no significant influence of the distance from the fusion line is observed. The UE values present a strong increase with increasing the distance from the fusion line.

At the fusion line, the yield strength values range from 386 MPa for a dose of $1.3 \cdot 10^{-5}$ dpa to 452 MPa for $1.3 \cdot 10^{-4}$ dpa at room temperature (Figure 3.30.a), and from 335 MPa for $1.3 \cdot 10^{-5}$ dpa to 352 MPa for $1.3 \cdot 10^{-4}$ dpa at high temperature (Figure 3.30.b). At about 4 mm away from the fusion line, the yield strength values range from 440 MPa for $1.3 \cdot 10^{-5}$ dpa to 420 MPa for $1.3 \cdot 10^{-4}$ dpa at room temperature (Figure 3.30.a), and from 275 MPa for $1.3 \cdot 10^{-5}$ dpa to 286 MPa for $1.3 \cdot 10^{-4}$ dpa at high temperature (Figure 3.30.b).

It can be concluded that there is a small but clear increase in the YS with irradiation dose. The UTS presents no significant dependence on dose, at least at room temperature. At high temperature the UTS is observed to increase with increasing dose. The UE decreases with increasing dose, at least at room temperature.

a)   b)
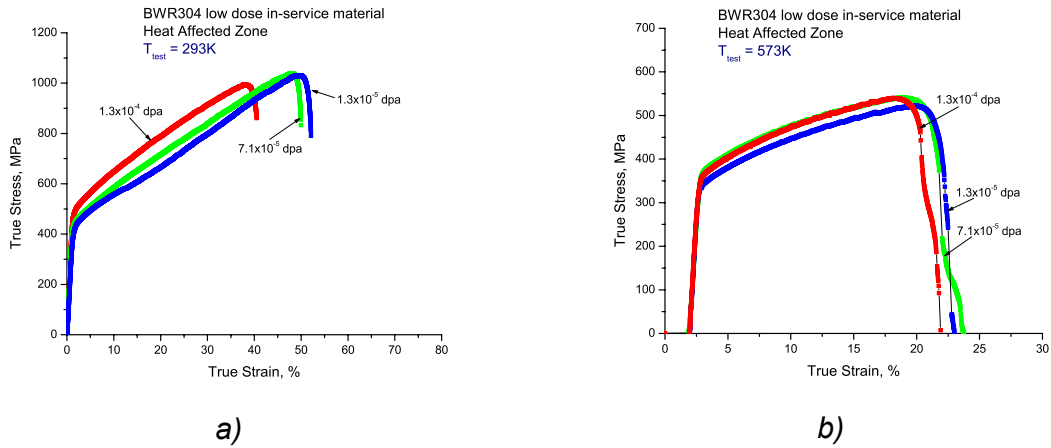
Figure 3.29. Typical tensile true stress–true strain curves versus dose for the HAZ of the low dose in-service material (Block A) at a) 293 K and b) 573 K.

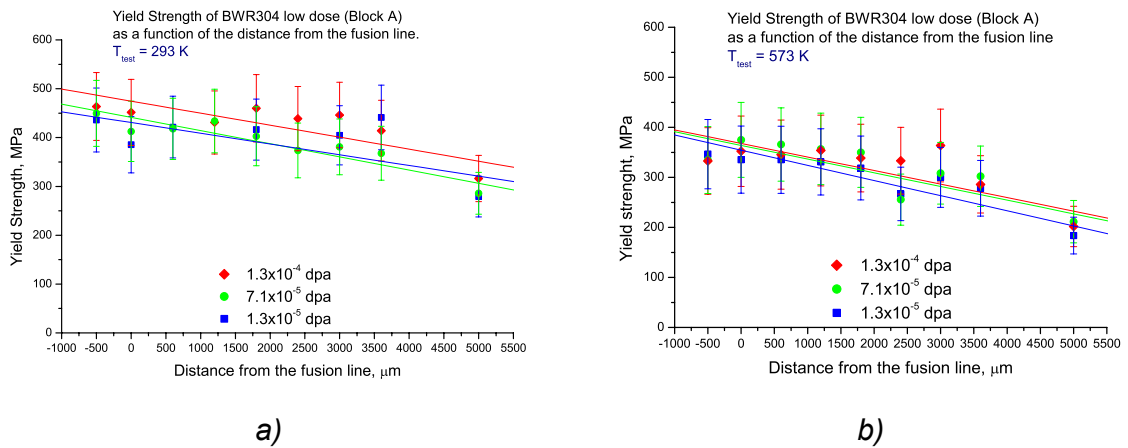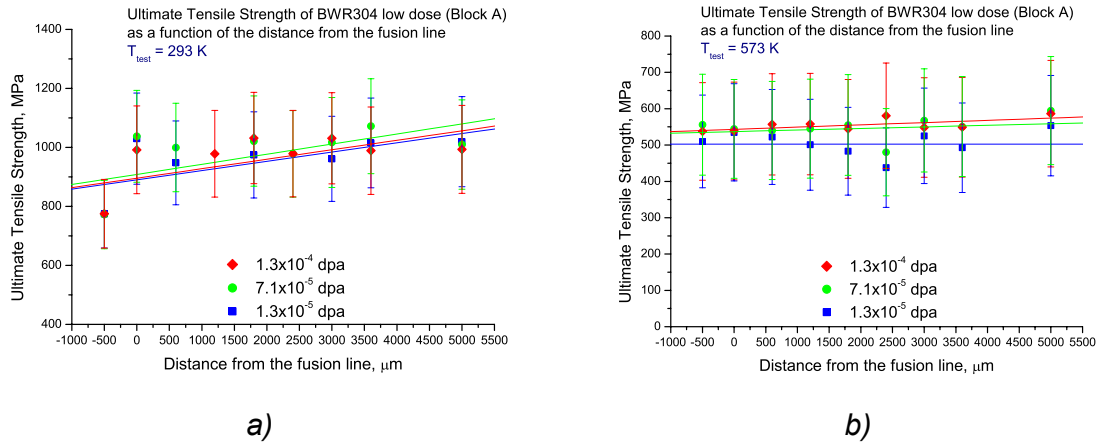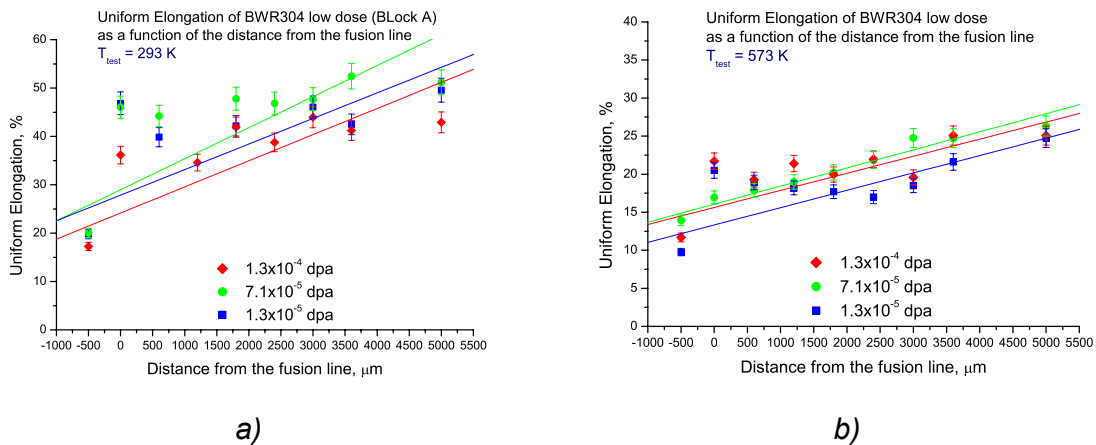a)   b)

Figure 3.30. Yield strength of the in-service material (Block A) as a function of the distance from the fusion line for three different doses at a) 293 K and b) 573 K (position 0 μm is at the heat affected zone, – 500 μm in the weld material).

77

a)   b)

Figure 3.31. Ultimate tensile strength of the in-service material (Block A) as a function of the distance from the fusion line for three different doses at a) 293 K and b) 573 K (position 0 µm is at the heat affected zone, – 500 µm in the weld material).

a)   b)

Figure 3.32. Uniform elongation of the in-service material (Block A) as a function of the distance from the fusion line for three different doses at a) 293 K and b) 573 K (position 0 µm is at the heat affected zone, – 500 µm in the weld material).

Table 3.11. Tensile properties of the low dose in-service material (Block A) at 293 K.

| Dose, dpa	Position	YS [MPa]		UTS [MPa]		UE [%]	
		True	Eng	True	Eng	True	Eng
1.3x10⁻⁵	WM	436	430	775	630	20	21
	1	386	386	1030	633	47	60
	2	420	416	948	625	40	50
	3	–	–	–	–	–	–
	4	416	408	975	630	42	52
	5	–	–	–	–	–	–
	6	405	400	960	596	46	60
	7	440	430	1015	651	42	54
	BM	280	278	1020	615	50	62
7.1x10⁻⁵	WM	450	445	772	630	20	21
	1	413	401	1038	647	46	57
	2	418	416	1000	630	44	55
	3	434	430	–	–	–	–
	4	403	393	1021	621	48	62
	5	374	368	978	603	47	60
	6	381	376	1017	627	48	60
	7	368	360	1072	622	52	70
	BM	286	278	1010	602	54	64
1.3x10⁻⁴	WM	464	452	775	650	17	18
	1	452	434	992	682	36	43
	2	–	–	–	–	–	–
	3	431	430	968	678	34	42
	4	460	455	1032	668	42	52
	5	439	430	980	651	39	47
	6	446	431	1031	652	44	56
	7	414	408	990	642	41	51
	BM	316	312	993	625	43	54

YS = yield strength
UTS = uniform tensile strength
UE = uniform elongation
WM = weld metal
BM = base metal
Specimen 1: close to the fusion line, specimen 7: far away from the fusion line.
The mean deviation values are of the same order of magnitude as in Table 3.4.

Table 3.12. Tensile properties of the low dose in-service material (Block A) at 573 K.

Dose, dpa	Position	YS [MPa]		UTS [MPa]		UE [%]	
		True	Eng	True	Eng	True	Eng
1.3x10^{-5}	WM	346	336	510	460	10	11
	1	335	326	535	436	20	22
	2	335	325	522	428	19	21
	3	331	323	501	416	19	20
	4	319	308	483	403	18	19
	5	267	263	438	368	17	18
	6	300	298	525	433	18	20
	7	278	270	493	395	22	24
	BM	184	184	554	420	25	30
7.1x10^{-5}	WM	335	328	556	477	14	14
	1	375	365	544	457	17	18
	2	366	355	540	449	18	19
	3	357	346	545	446	19	21
	4	350	340	555	453	20	22
	5	255	252	480	389	22	24
	6	308	300	568	441	25	27
	7	302	397	550	428	25	27
	BM	212	210	595	445	26	31
1.3x10^{-4}	WM	333	327	635	537	12	13
	1	352	338	540	450	17	19
	2	345	332	557	455	19	21
	3	354	343	558	450	21	23
	4	340	328	554	445	20	21
	5	333	328	580	464	22	24
	6	364	358	548	450	20	21
	7	286	278	550	426	25	28
	BM	202	200	586	450	25	29

YS = yield strength
UTS = uniform tensile strength
UE = uniform elongation
WM = weld metal
BM = base metal
Specimen 1: close to the fusion line, specimen 7: far away from the fusion line.
The mean deviation values are of the same order of magnitude as in Table 3.4.

3.2.2.3.2 In-service material irradiated to high dose (Block B)

Typical tensile true stress–true strain curves, as obtained in the HAZ at 293 K and 573 K, for three different doses, are shown in Figure 3.35. Values of the YS, UTS, and UE, as deduced from the tensile true stress–true strain curves, are reported in Figures 3.34, 3.35, 3.36, respectively. These values are also summarised in Table 3.13 for testing at room temperature and in Table 3.14 for the high temperature testing. In these figures the number 1 refers to the specimen that is the closest to the fusion line, while the number 7 refers to a specimen cut out relatively far away from the fusion line.

The mechanical behaviour of the high dose in-service material is similar to that of the low dose in-service material.

A significant decrease in the YS values with increasing the distance from the fusion line can be seen at both testing temperatures. The UTS values show a slight decrease with decreasing distance from the fusion line, at both testing temperatures. The UE values present a strong increase with increasing distance from the fusion line, at both testing temperatures.

At the fusion line, the YS values range from 523 MPa for 0.12 dpa to 518 MPa for 0.35 dpa at room temperature (Figure 3.34.a), and from about 400 MPa for 0.12 dpa to 490 MPa for 0.35 dpa at high temperature (Figure 3.34.b). At about 4 mm away from the fusion line, the YS values range from 473 MPa for 0.12 dpa to 504 MPa for 0.35 dpa at room temperature (Figure 3.34.a), and from 390 MPa for 0.12 dpa to 440 MPa for 0.35 dpa at high temperature (Figure 3.34.b).

It can be concluded that there is a significant increase in the YS with irradiation dose, which is more important at high temperature. The UTS values seem also to present a clear increase with the irradiation dose, at both testing temperatures. The dose dependence of the UE values is here less clear than in the case of the stress values.

a)   b)
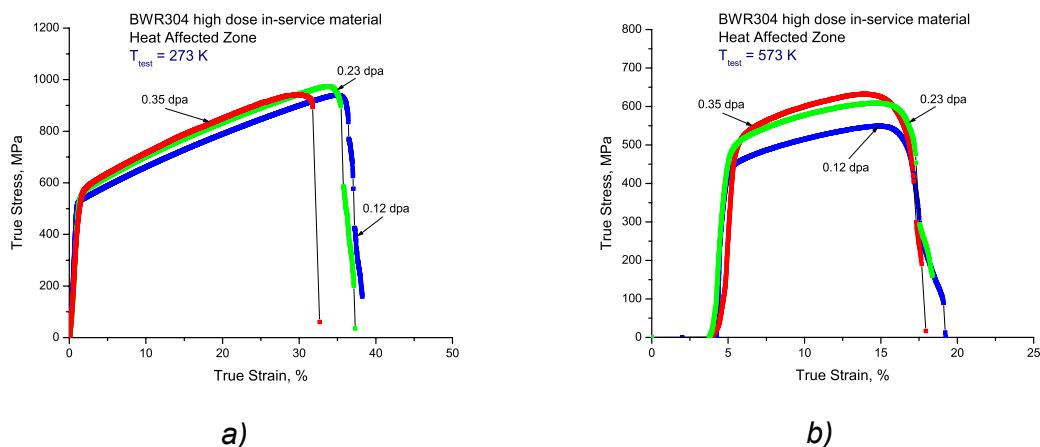
Figure 3.33. Typical tensile true stress–strain curves for the HAZ of the high dose in-service material (Block B,) for three different doses, at a) 293 K and b) 573 K.

a)   *b)*
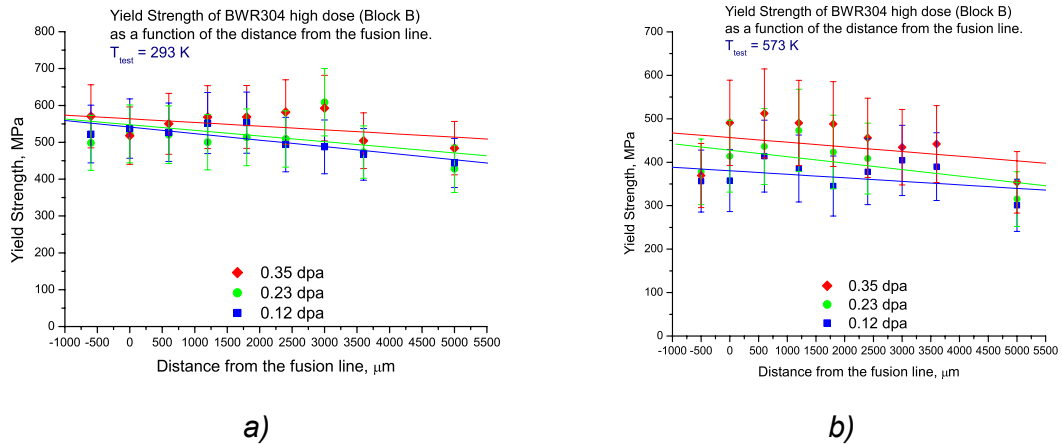
Figure 3.34. Yield strength of the high dose in-service material (Block B) as a function of the distance from the fusion line, for three different doses at a) 293 K and b) 573 K.

a)   *b)*
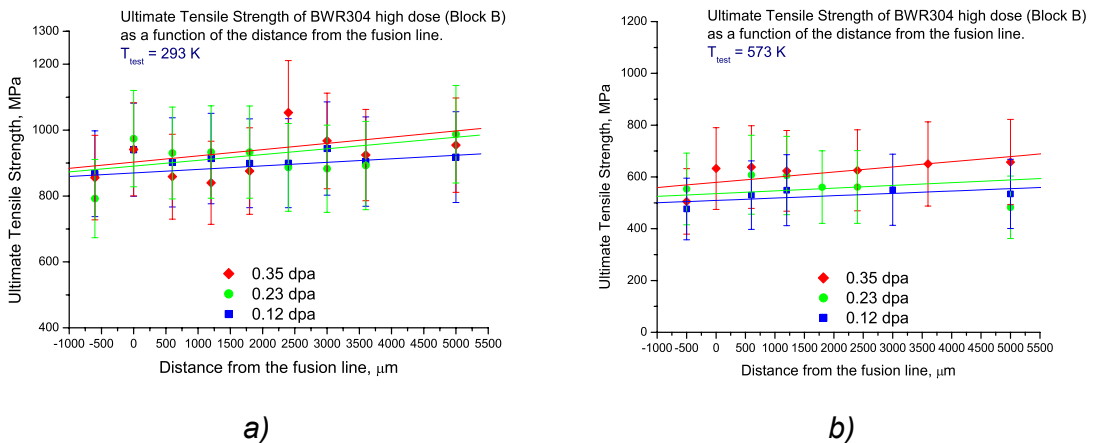
Figure 3.35. Ultimate tensile strength of the high dose in-service material (Block B) as a function of the distance from the fusion line, for three different doses, at a) 293 K and b) 573 K.

a)   *b)*
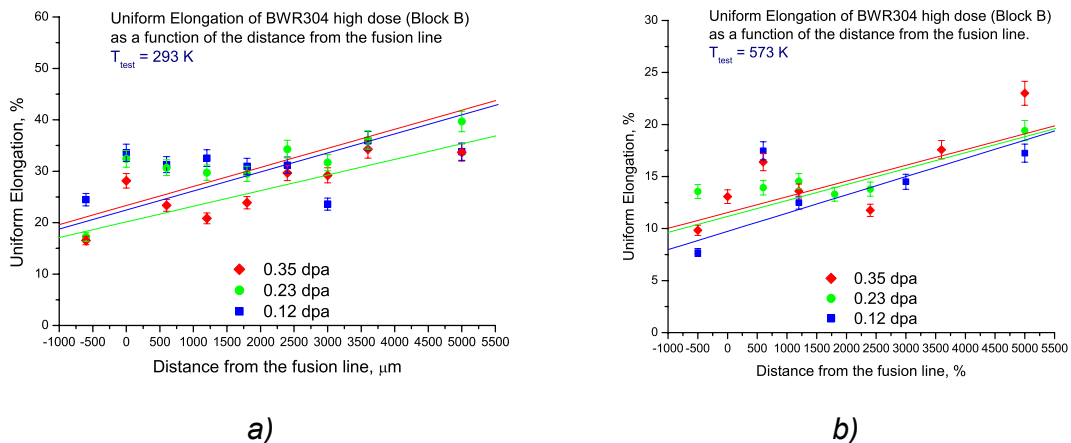
Figure 3.36. Uniform elongation of the high dose in-service material (Block B) as a function of the distance from the fusion line, for three different doses, at a) 293 K and

b) 573 K.
Table 3.13. Tensile properties of the high dose in-service material (Block B) at 293 K.

Dose, dpa	Position	YS [MPa]		UTS [MPa]		UE [%]	
		True	Eng	True	Eng	True	Eng
0.12	WM	500	485	868	673	24	27
	1	523	517	940	668	34	39
	2	520	516	902	660	31	36
	3	500	495	914	660	33	37
	4	514	508	900	657	31	36
	5	510	502	900	655	31	36
	6	610	601	944	744	24	26
	7	473	470	905	630	36	43
	BM	430	424	918	648	34	40
0.23	WM	522	511	792	661	17	19
	1	537	530	974	700	32	38
	2	527	520	930	682	31	35
	3	552	546	934	690	30	34
	4	553	548	933	692	30	34
	5	494	490	890	630	34	39
	6	490	482	890	640	32	37
	7	467	462	892	620	36	42
	BM	444	428	987	660	40	48
0.35	WM	570	560	856	717	17	18
	1	518	502	942	708	28	31
	2	550	543	860	680	23	26
	3	568	561	840	682	21	22
	4	570	572	876	691	24	26
	5	582	550	1053	757	30	32
	6	593	586	967	724	29	32
	7	504	500	924	655	34	38
	BM	484	474	954	680	34	39

YS = yield strength
UTS = uniform tensile strength
UE = uniform elongation
WM = weld metal
BM = base metal
Specimen 1 close to the fusion line, specimen 7 far away from the fusion line.
The mean deviation values are of the same order of magnitude as in Table 3.4.

Table 3.14. Tensile properties of the high dose in-service material (Block B) at 573 K.

Dose, dpa	Position	YS [MPa]		UTS [MPa]		UE [%]	
		True	Eng	True	Eng	True	Eng
0.12	WM	356	352	476	436	7	8
	1	–	–	–	–	–	–
	2	414	402	530	466	17	13
	3	390	370	550	485	12	13
	4	345	332	–	–	–	–
	5	378	368	–	–	–	–
	6	404	390	550	476	14	15
	7	390	380	–	–	–	–
	BM	300	298	535	450	17	19
0.23	WM	378	374	553	484	13	14
	1	414	395	–	–	–	–
	2	436	425	609	530	14	14
	3	473	450	605	523	15	15
	4	410	390	560	490	13	14
	5	424	404	460	488	14	15
	6	–	–	–	–	–	–
	7	–	–	–	–	–	–
	BM	315	310	483	400	19	20
0.35	WM	370	367	505	460	9	10
	1	491	460	632	552	13	14
	2	512	480	638	540	16	17
	3	490	465	623	543	14	15
	4	488	457	–	–	–	–
	5	456	460	626	555	12	12
	6	435	415	–	–	–	–
	7	442	418	650	544	18	19
	BM	354	347	658	503	23	27

YS = yield strength
UTS = uniform tensile strength
UE = uniform elongation
WM = weld metal
BM = base metal
Specimen 1 close to the fusion line, specimen 7 far away from the fusion line.
The mean deviation values are of the same order of magnitude as in Table 3.4.

3.3 SCANNING ELECTRON MICROSCOPY OBSERVATIONS

Fractography analyses of tensile tested samples from the base test materials were performed by means of scanning electron microscopy (SEM).

A low magnification image of the AISI 347 tensile tested at 293 K is shown in Figure 3.37. A slight necking phenomenon is evidenced. Figures 3.38 and 3.39 show SEM images at higher magnification of the fracture surfaces of AISI 347 and AISI 304, respectively. It can be seen that the fracture surfaces have a ductile aspect.
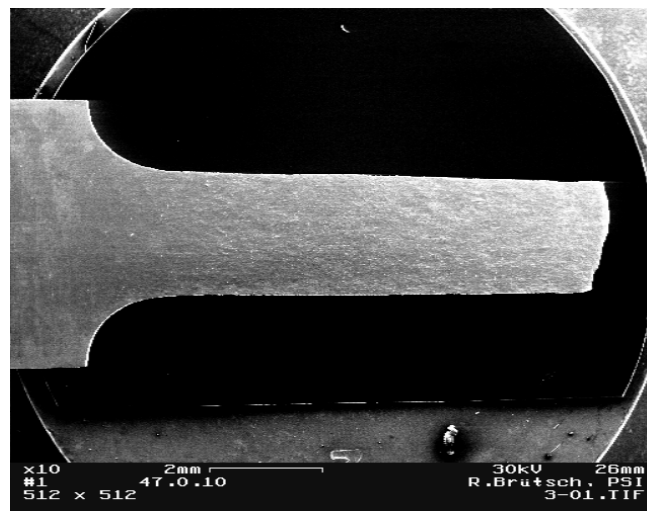
Figure 3.37. SEM image of a tensile specimen of the AISI 347 BM following deformation up to fracture at 293 K.
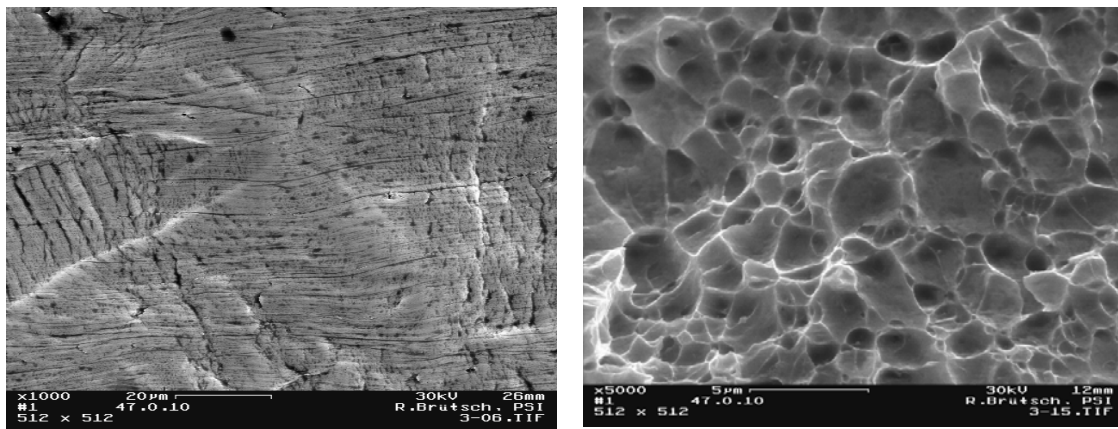
Figure 3.38. SEM images of fracture surface of the AISI 347 BM tensile tested up to fracture at 293 K.
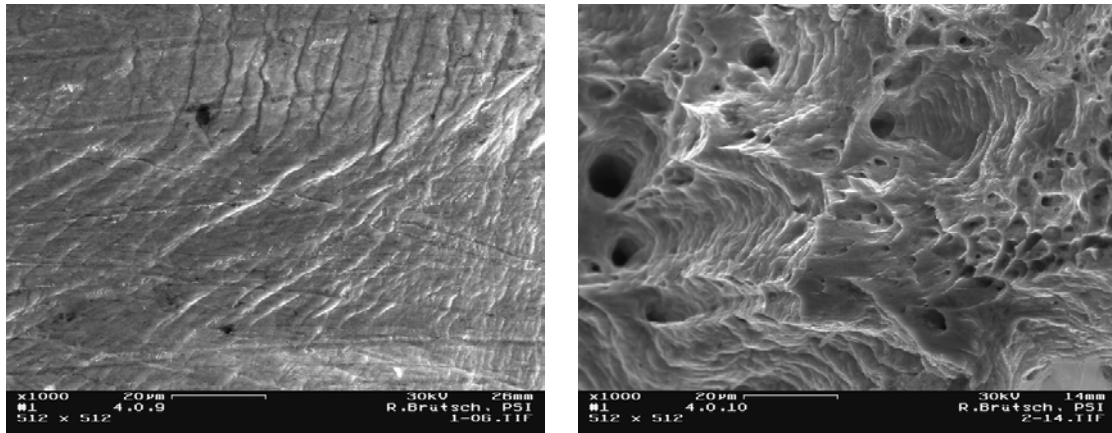
Figure 3.39. SEM images of fracture surface of the AISI 304 BM tensile tested up to fracture at 293 K.

3.4 TRANSMISSION ELECTRON MICROSCOPY OBSERVATIONS

3.4.1 Microstructure of undeformed materials

3.4.1.1 Unirradiated test materials

Bright field TEM images of the BMs, unaffected by the thermal cycles upon welding, are presented in Figure 3.40 for AISI 304 and in Figure 3.41 for AISI 347.

The microstructure is typical of that of austenitic stainless steels, for both materials, with isolated dislocations and extended stacking faults.

Figures 3.42 and 3.43 show bright field TEM images of the HAZs, close to the fusion line, for AISI 304 and AISI 347, respectively.

Close to the fusion line one observes recrystallised areas offering a uniform contrast, as they are relatively free of dislocations, surrounded by a matrix full of dislocations.
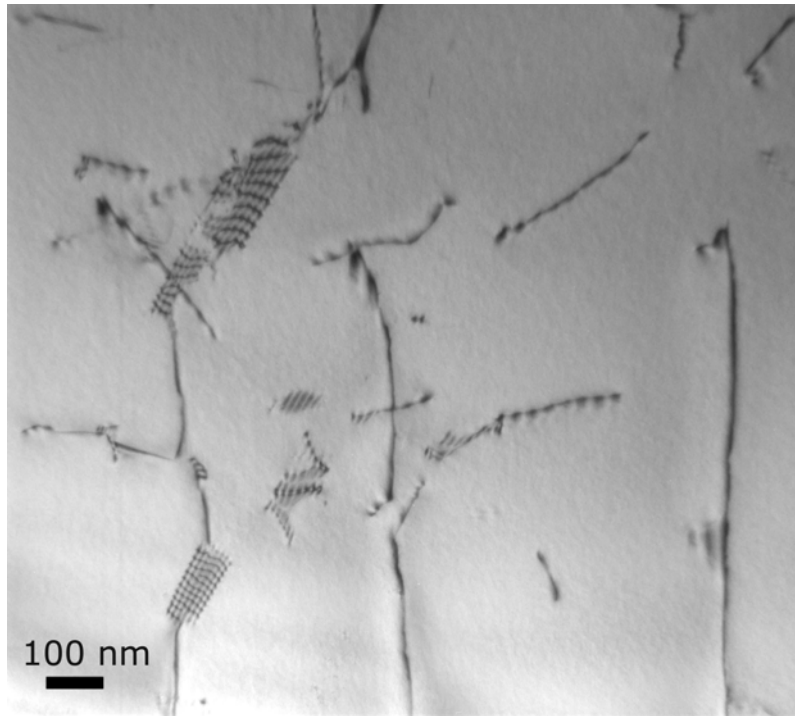
Figure 3.40. AISI 304 base material.
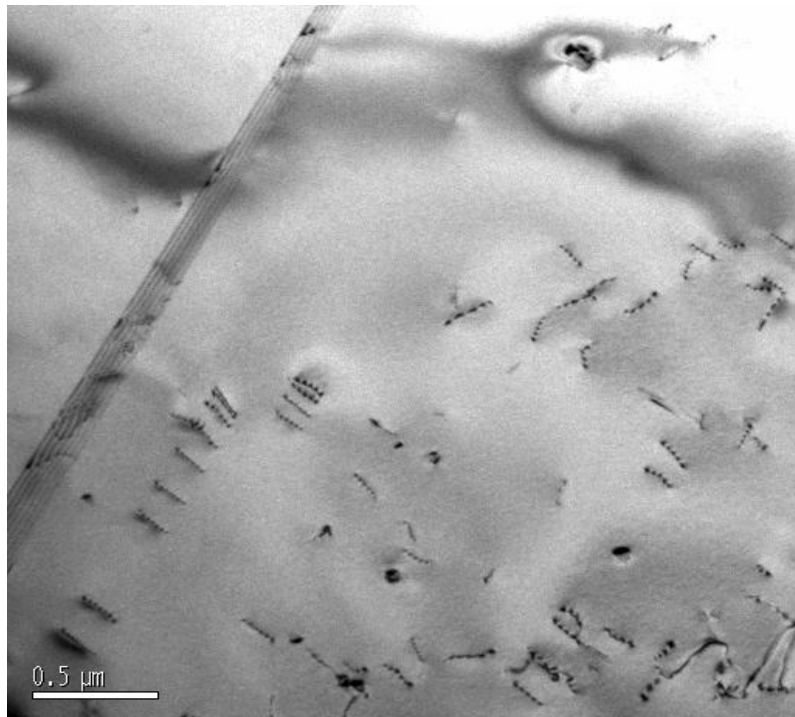
Figure 3.41. AISI 347 base material.
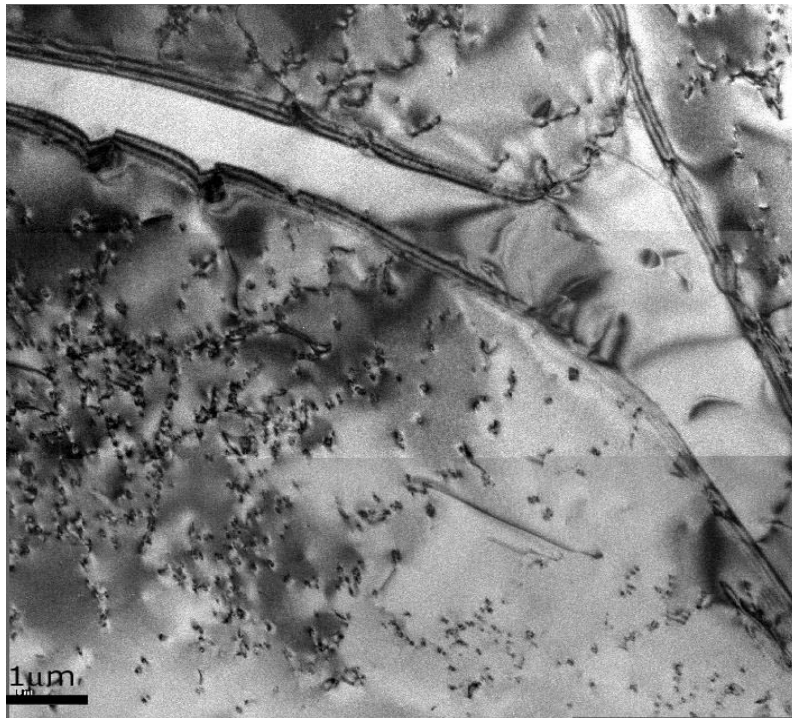
Figure 3.42. AISI 304 heat affected zone.

Figure 3.43. AISI 347 heat affected zone.

Dislocation density

The mean dislocation density has been evaluated for the BM and the HAZ of both test materials. Results are listed in Table 3.15. They are also reported in Figure 3.44 as a function of the distance from the fusion line.

As it can be seen in Figure 3.44, the dislocation density decreases as the distance from the fusion line increases. It can also be observed that the dislocation density is slightly higher in the case of AISI 304, as compared to AISI 347.

Table 3.15. Dislocation density in AISI 304 and AISI 347 test materials.

Material	Mean dislocation density [$*10^9$ cm^{-2}]					
	1	2	3	4	5	BM
AISI 304	13	7	2	6	9	3
AISI 347	8	8	6	9	5	1

1, 2, 3, 4 or 5 represents the distance from the fusion line, according to Figure 2.4 (specimen no 1: close to the fusion line). BM = base material.
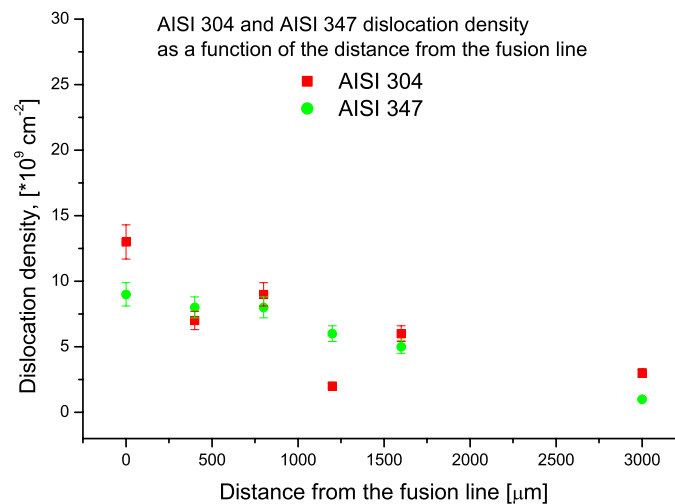
Figure 3.44. Dislocation density as a function of the distance from the fusion line for the unirradiated, undeformed test materials.

Stacking fault energy

Weak beam dark field TEM images g(3g), with an operating diffraction vector [20-2] close to a zone axis <111>, were used to determine the stacking fault energy in the case of the AISI 347 base test material. The weak beam image in Figure 3.45 shows clearly the dislocation numbered 1, with the Burgers vector b = [10-1], dissociated into two partial dislocations with the Burgers vectors b_1 = 1/6[21-1] and b_2 = 1/6[1-1-2]. Figure 3.46.a presents the corresponding simulated image, using the same imaging conditions, and the associated transverse intensity profile (Figure 3.46.b).

The apparent separation distance between the two partial dislocations was measured to be 14 nm. The actual separation distance was found to be 10 nm, through correction of the apparent distance by image simulations and the stacking fault energy was determined to be 38 mJ/m^2.
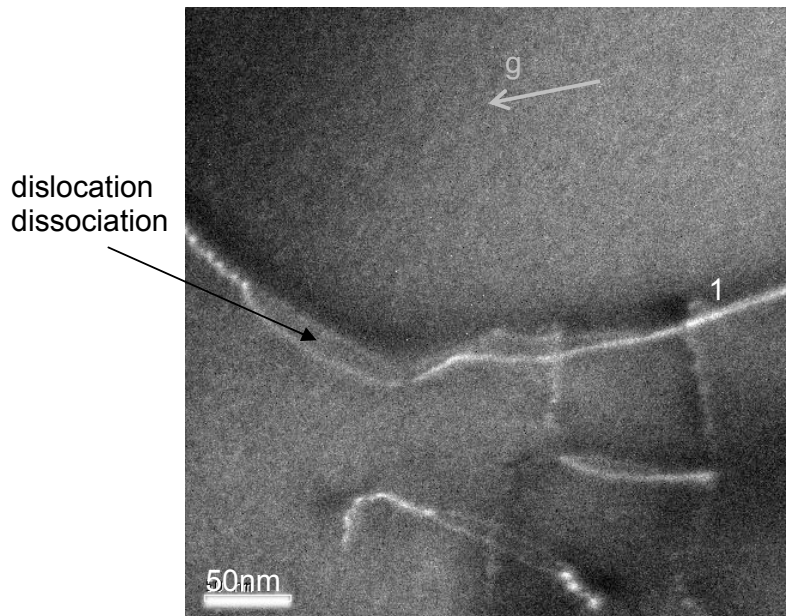
Figure 3.45. Experimental g(3g) weak beam TEM image, g = [20-2], close to a zone axis <111> of a dissociated dislocation in the AISI 347 BM.

a)

b)
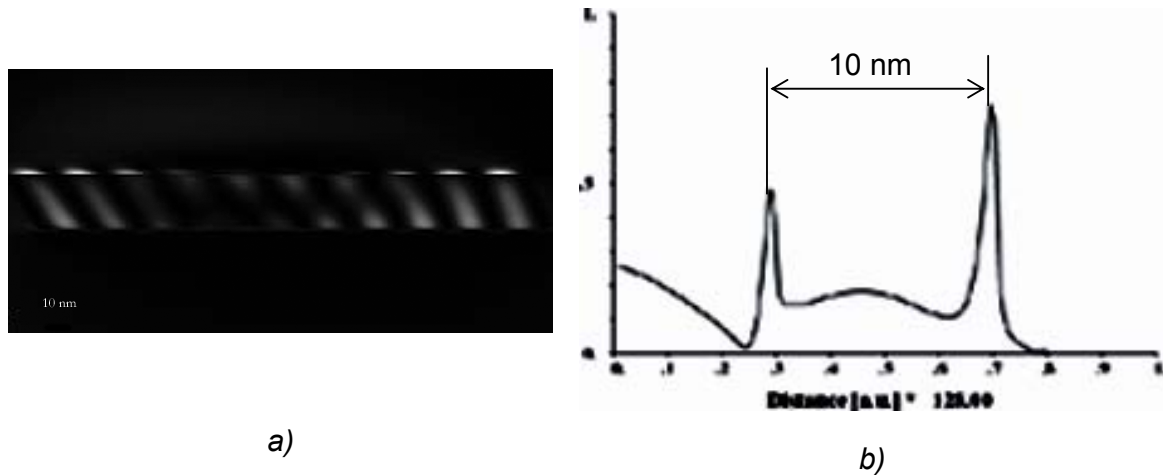
Figure 3.46 a) Corresponding simulated weak beam image and b) the associated transverse intensity profile.

Recrystallised areas in the heat-affected zone

After welding the austenitic stainless steels develop a duplex microstructure, consisting of a fine discontinuous network of ferrite interphase, separated by grains of austenite, as shown in Figures 3.42 and 3.43. This interphase was characterised by TEM using selected area diffraction (SAD) and convergent beam electron diffraction (CBED) techniques. The CBED patterns taken in the TEM were simulated using the Electron Microscopy Image Simulation software EMS [104] for a better determination of the lattice parameter.

The simulated CBED images were superimposed on the images taken in TEM, according to Figure 3.47, to determine the lattice parameter of the interphase. Simulations were performed for the (-1-1-1) zone axis, the (-1-1-1) foil normal and the (8.8, -15.04, 6.21) centre of Laue circle. The lattice parameter, determined by fitting the simulated Kikuchi lines to the experimental ones, was found to be: $a_0 = 0.364$ nm.

The lattice type of the interphase was determined by indexing the CBED patterns. Figure 3.48 shows a CBED of the (111) zone axis of the matrix, together with the corresponding SAD. It is known that austenitic stainless steels have fcc structure. To find the (111) zone axis in the interphase it was necessary to tilt away from the orientation conditions found for the matrix. The CBED pattern of the (111) zone axis of the interphase is presented in Figure 3.49, with the corresponding SAD. Strong differences between the two obtained patterns can be seen. By comparing the obtained patterns to the ones found in the literature, it was concluded that the interphase has a bcc structure (ferrite).

The chemical composition of the interphase was determined in TEM by Energy Dispersive Spectrometry (EDS) and compared to the one obtained for the matrix. The results are listed in Table 3.16, for AISI 347. It was found that Cr is enriched in the interphase, while Ni is depleted. This is in agreement with the previous

conclusion, pointing out that the interphase is ferrite, as it is well known that Cr and Si are ferrite forming elements, while Ni and Fe are austenite forming elements.

Table 3.17. Chemical composition determined by EDS of the matrix and the interphase for AISI 347, in wt.%.

Position	Si	Cr	Mn	Fe	Ni	Nb
Matrix	1.7	20.6	1.3	67.29	9.02	0.18
Interphase	1.9	29.83	0.7	65.03	4.22	0.08
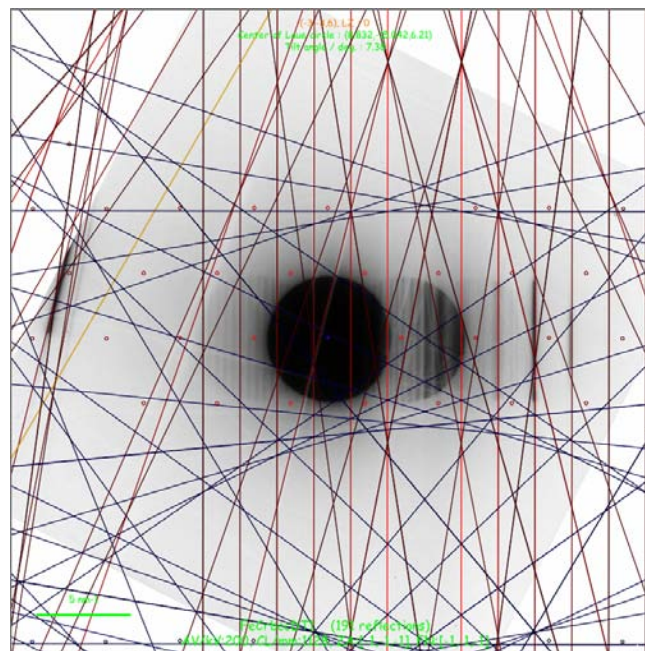
Figure 3.47. Simulated and experimental CBED images of the interphase in the HAZ.
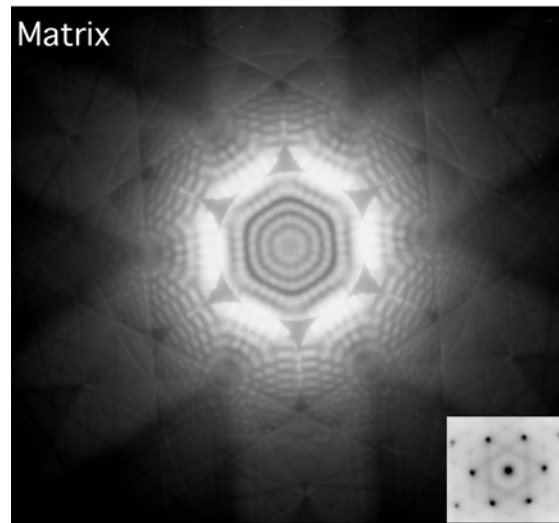
Figure 3.48. CBED pattern and corresponding SAD pattern obtained for the (111) zone axis of the matrix (fcc structure).
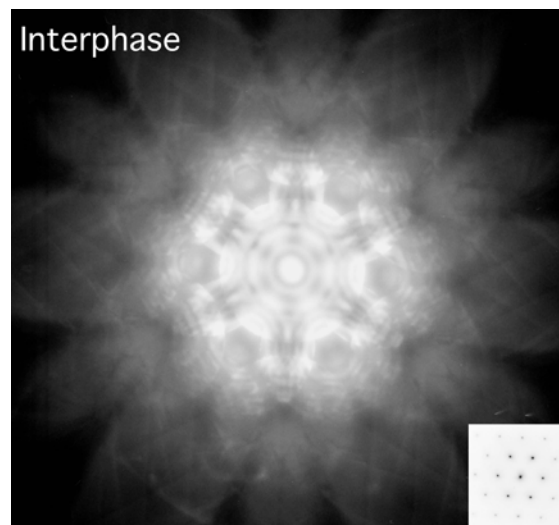
Figure 3.49. CBED pattern and corresponding SAD pattern obtained for the (111) zone axis of the interphase (bcc structure).

3.4.1.2 Irradiated test materials

The microstructure of both materials irradiated up to 0.3 dpa was studied by TEM. Figure 3.50 shows a WBDF image of AISI 304 close to the fusion line irradiated to 0.3 dpa, which was taken using the diffraction condition g(5g), with g(200) close to the zone axis (110). The microstructure contains typical irradiation-induced defects, such as black dots and faulted dislocation loops (Frank loops). The Frank loops were identified on the basis of their specific black/white image contrast. Black dots are very small defects that appear as white dots in WBDF and cannot be identified. In Figure 3.51 a detail of the interphase present in the HAZ is shown. No irradiation-induced defects have been evidenced in the interphase. Either no defects have been produced by the irradiation in the interphase of bcc structure, or the defects produced by the irradiation have annihilated to sinks or they are too small to be resolved in TEM. Note that the TEM resolution limit is about 1 nm in WBDF imaging. For the AISI 347 material irradiated up to 0.3 dpa the same characteristics were observed. In Figure 3.52 a WBDF image of the AISI 347 matrix, full of irradiation-induced defects, is shown. The exact position as a function of the distance from the fusion line of the TEM specimens could not be determined, as explained in § 2.4.3.1, but all the specimens were cut out from the HAZ.

In increasing the irradiation dose to 1 dpa, no significant changes were observed in the irradiation-induced microstructure. Figure 3.53 shows a WBDF image of the AISI 304 irradiated up to 1 dpa and Figure 3.54 the AISI 347 irradiated to the same dose.

Two-beam dark field images taken under dynamical conditions were used to determine the Burgers vector of the Frank loops, using the four different reflections close to a <110> zone axis. The contrast of the loops depends on the magnitude of $\lvert g \cdot b \rvert$ and on the dislocation loop orientation. The obtained contrasts are shown in Figure 3.55 and the corresponding values of $\lvert g \cdot b \rvert$ are reported in Table 3.18. By this procedure, the Burgers vector of the Frank loop shown in Figure 3.55 was determined to be: b = 1/3[01-1].

The defect size distribution was determined using series of micrographs imaged using different dark field and weak beam conditions, and reported in Figure 3.56 for 0.3 dpa irradiated materials and in Figure 3.57 for 1 dpa irradiated materials. The mean defect size and density values are also summarised in Table 3.17. Figures 5.58 and 5.59 present the defect density and defect size as a function of the irradiation dose, respectively. It can be seen that the loop density remains more or less constant with dose for both AISI 304 and AISI 347. The density of black dots increases with increasing dose for AISI 304 and decreases with increasing dose in the case of AISI 347. The mean loop size increases with increasing dose for in the case of AISI 347 and remains more or less constant for AISI 304, while the black dot size remains constant with dose for both materials. The total defect density is higher in AISI 304 as compared to AISI 347. The loop size is slightly higher in AISI 347 as compared to AISI 304. The mean size of black dots is similar in both materials, for both irradiation doses.
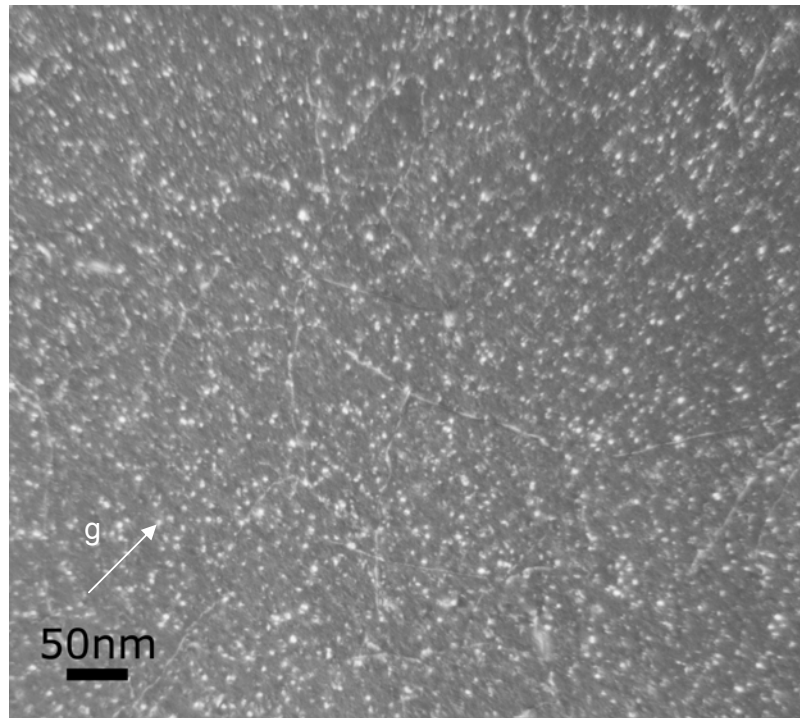
Figure 3.50. Weak beam image g(5g), g {200}, close to a zone axis <011> of AISI 304 close to the fusion line, irradiated up to 0.3 dpa.
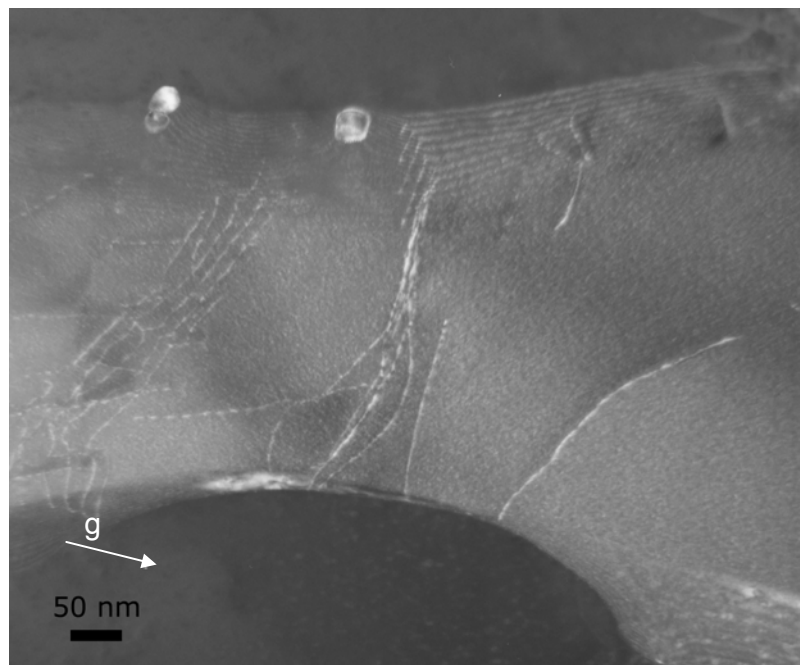
Figure 3.51. Weak beam image g(4g), g {111}, close to a zone axis <311> of AISI 304 ferrite interphase irradiated up to 0.3 dpa.

95
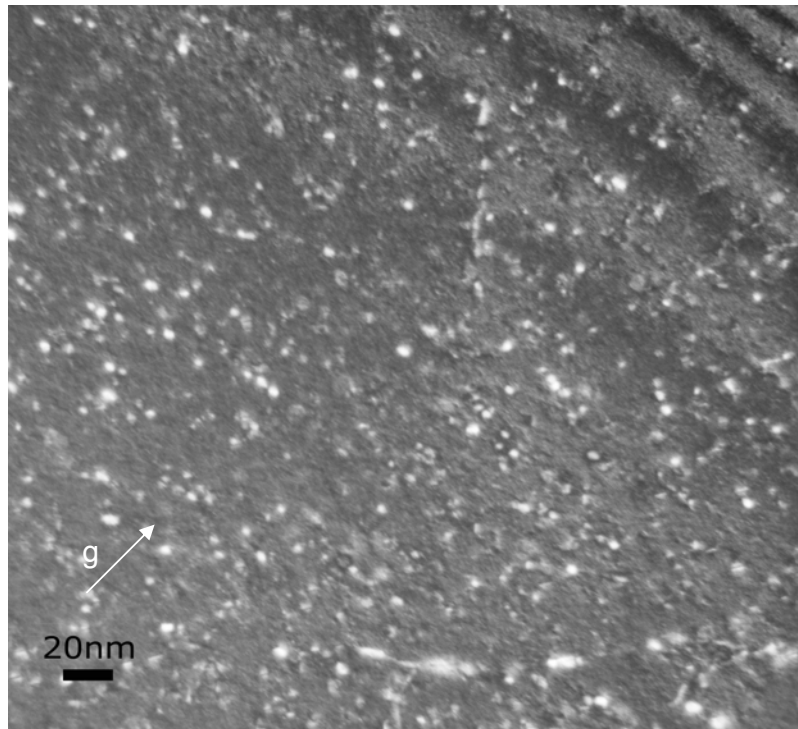
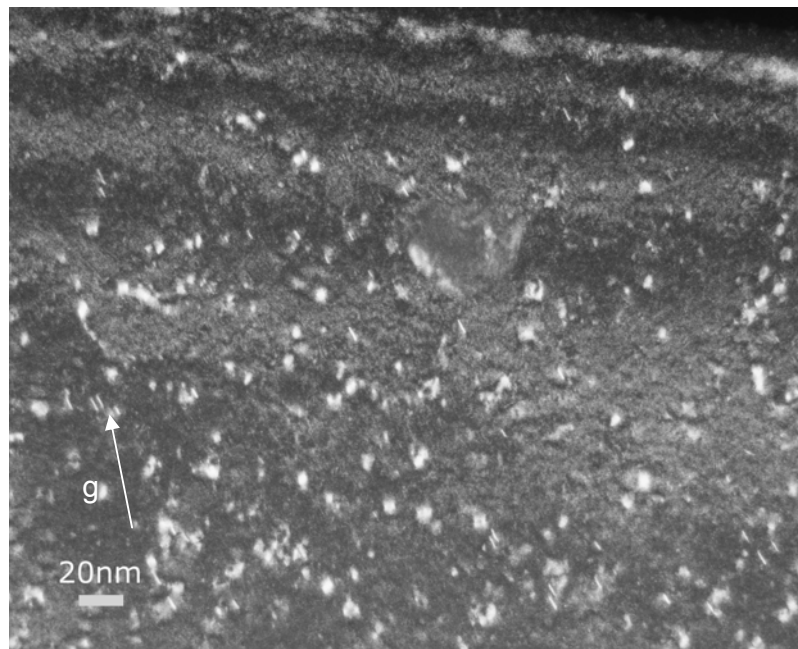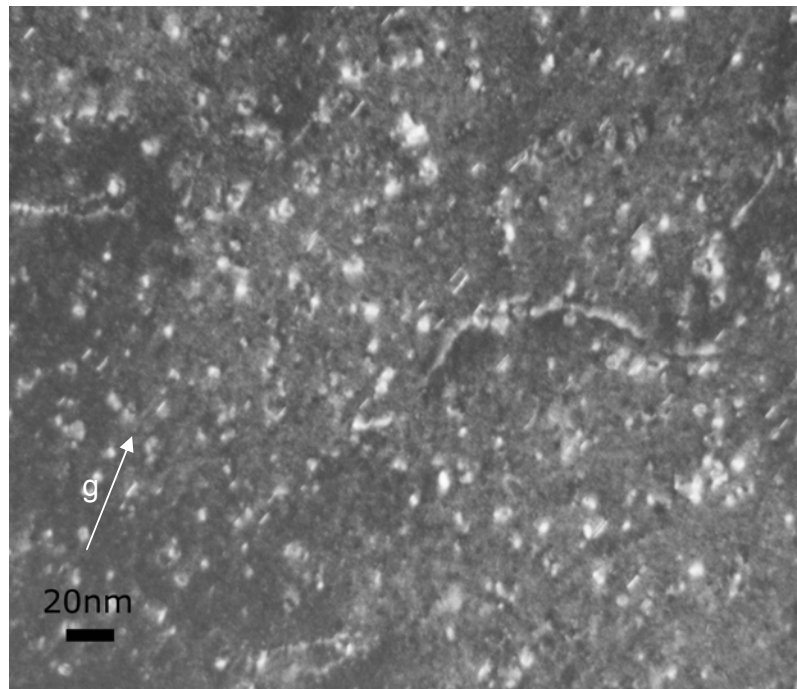*Figure 3.52. Weak beam image g(5g), g {200}, close to a zone axis <011> of AISI 347 irradiated up to 0.3 dpa.*

Figure 3.53. Weak beam image g(5g), g {200}, close to a zone axis <011> of AISI 304 irradiated up to 1 dpa.

Figure 3.54. Weak beam image g(5g), g {200}, close to a zone axis <011> of AISI 347 irradiated up to 1 dpa.
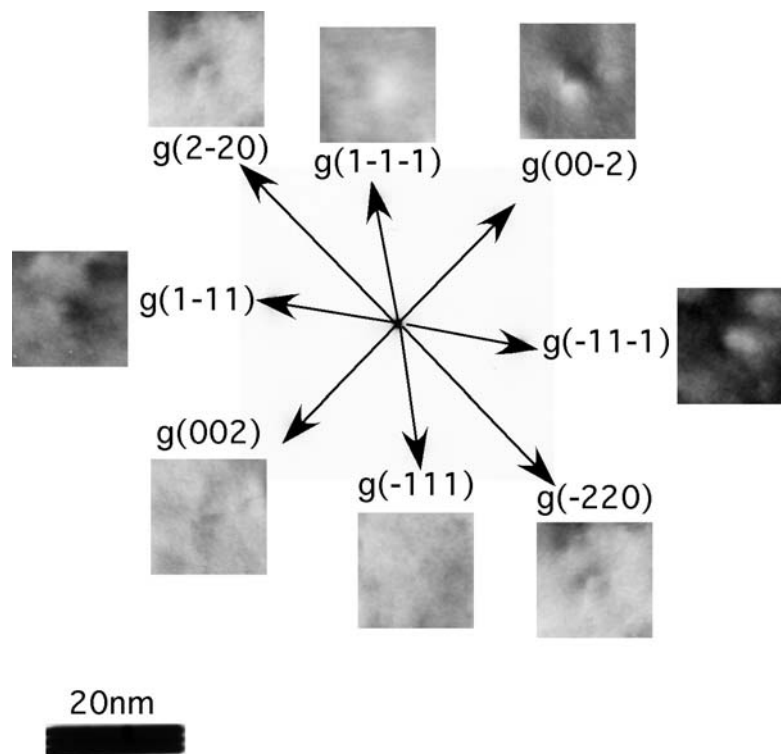
Figure 3.55. Dark field images (s_g = 0 or very close to zero) of a dislocation loop showing different image contrasts for different reflections close to a zone axis <011> in the case of AISI 347 irradiated up to 1 dpa.

Table 3.18. $|g \cdot b|$ values for all possible Burgers vectors.

b \ g	[002]	[00$\bar{2}$]	[$\bar{1}$11]	[1$\bar{1}$1]	[$\bar{1}\bar{1}$1]	[11$\bar{1}$]	[$\bar{2}$20]	[$\bar{2}\bar{2}$0]
[101]	2	-2	0	2	-2	0	2	-2
[0$\bar{1}$1]	2	-2	2	0	0	-2	-2	2
[01$\bar{1}$]	-2	2	0	-2	2	0	-2	2
[10$\bar{1}$]	-2	2	-1	0	0	2	2	-2
[1$\bar{1}\bar{1}$]	-2	2	-3	1	1	3	4	-4
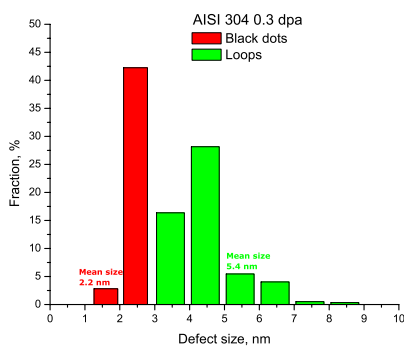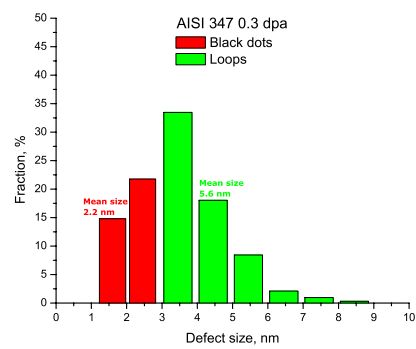
Figure 3.56. Defect size distribution for a) AISI 304 and b) AISI 347 irradiated up to 0.3 dpa.
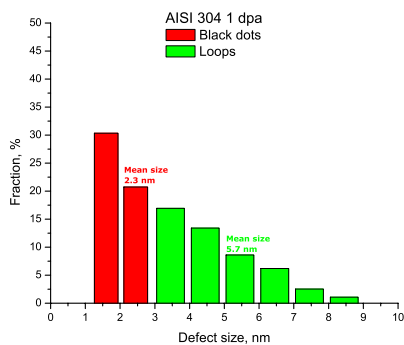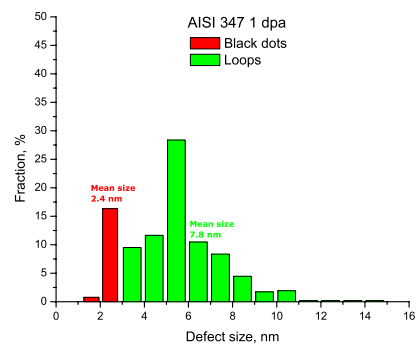
Figure 3.57. Defect size distribution for a) AISI 304 and b) AISI 347 irradiated up to 1 dpa.
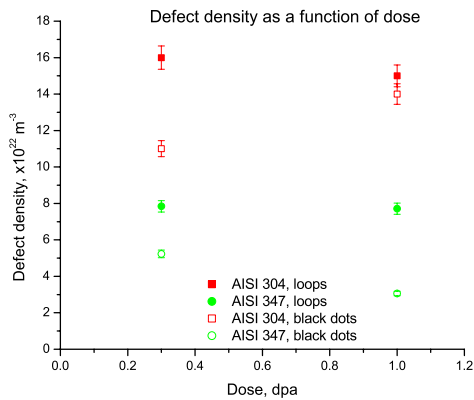
Figure 3.58. Defect density as a function of dose for both AISI 304 and AISI 347.
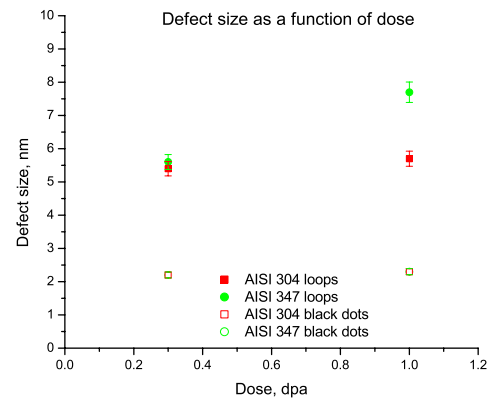
Figure 3.59. Defect size as a function of dose for both AISI 304 and AISI 347.

Table 3.17. Defect density and mean size versus dose for the AISI 304 and AISI 347 irradiated materials.

Material	Black dots		Dislocation loops		Total density
	density [m^{-3}]	mean size [nm]	density [m^{-3}]	mean size [nm]	
AISI 304 0.3 dpa	1.1×10^{23}	2.2	1.6×10^{23}	5.4	2.7×10^{23}
AISI 304 1.0 dpa	1.4×10^{23}	2.2	1.6×10^{23}	5.4	2.7×10^{23}
AISI 347 0.3 dpa	5.2×10^{22}	2.2	7.8×10^{22}	5.6	1.3×10^{23}
AISI 347 1.0 dpa	3.0×10^{22}	2.3	7.7×10^{22}	7.7	1.0×10^{23}

3.4.1.3 In-service material

Weak beam dark field TEM images of the low dose in-service BM (Block A), unaffected by the thermal cycles upon welding, irradiated to 1.3×10^{-5} dpa and 1.3×10^{-4} dpa, are presented in Figures 3.60 and 3.61, respectively.

The low dose in-service material (Block A) exhibits a microstructure typical of austenitic stainless steels, with no visible irradiation-induced defects, certainly due to the very small accumulated damage.

Weak beam dark field images of the low dose in-service (Block A) HAZ, close to the fusion line are presented in Figure 3.62 for 1.3×10^{-5} dpa and Figure 3.63 for 1.3×10^{-4} dpa. There is no significant difference between the microstructure of the base material and that of the HAZ, both microstructures containing isolated dislocations and extended staking faults, with no evidence of irradiation-induced defects.

The mean dislocation density was determined for the HAZ and the BM of the low dose in-service material (Block A). The measured values are listed in Table 3.18, and reported as a function of the dose in Figure 3.64.

There seems to be a small irradiation-induced increase in the dislocation density with dose in both the BM and the HAZ, this increase being slightly more important in the HAZ.
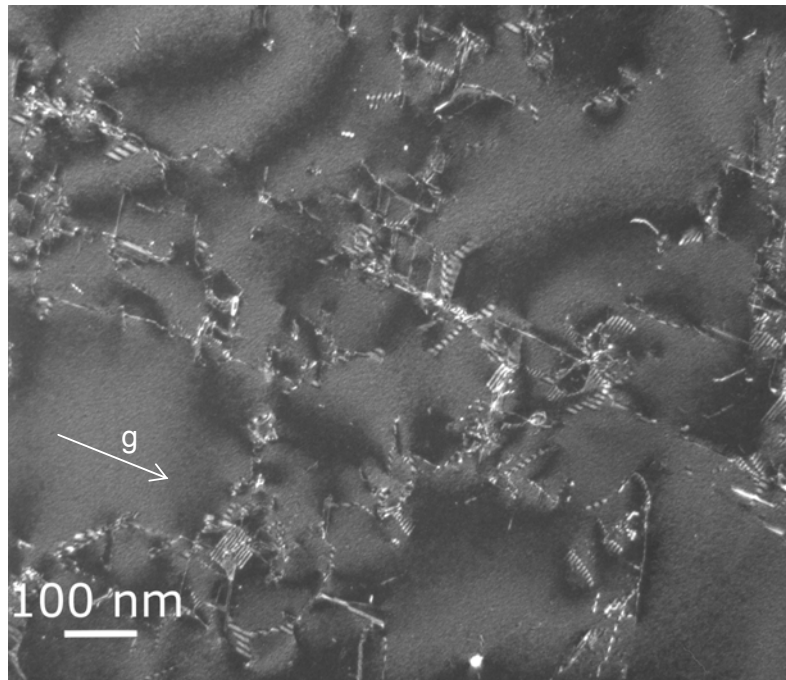
Figure 3.60. Weak-beam image g(4g), g {200}, close to a zone axis <011>, of the low dose in-service (Block A) BM (4 mm away from the fusion line) irradiated to 1.3×10^{-5} dpa.
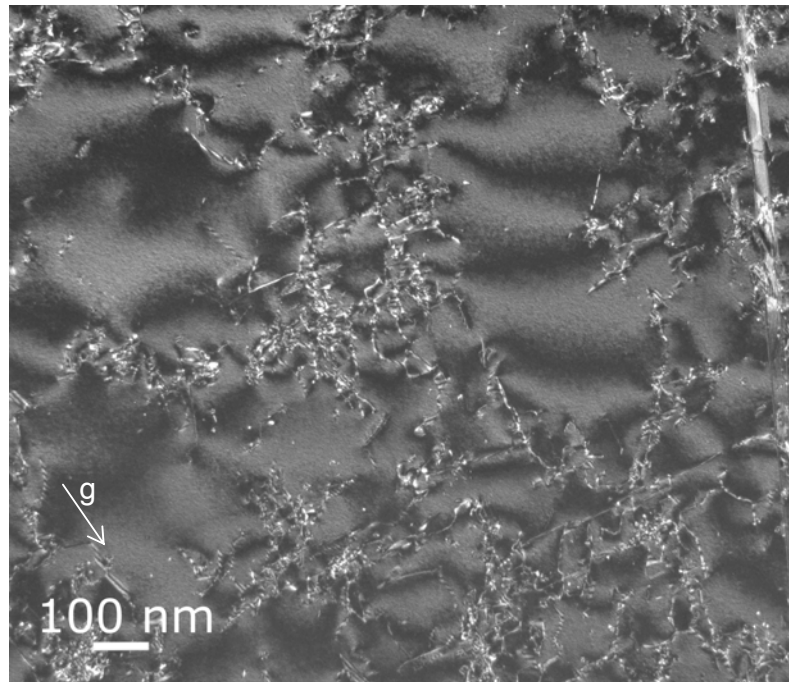
Figure 3.61. Weak-beam image g(6g), g {200},close to a zone axis <011>, of the low dose in-service (Block A) BM (4 mm away from the fusion line) irradiated to 1.3x10^{-4} dpa.
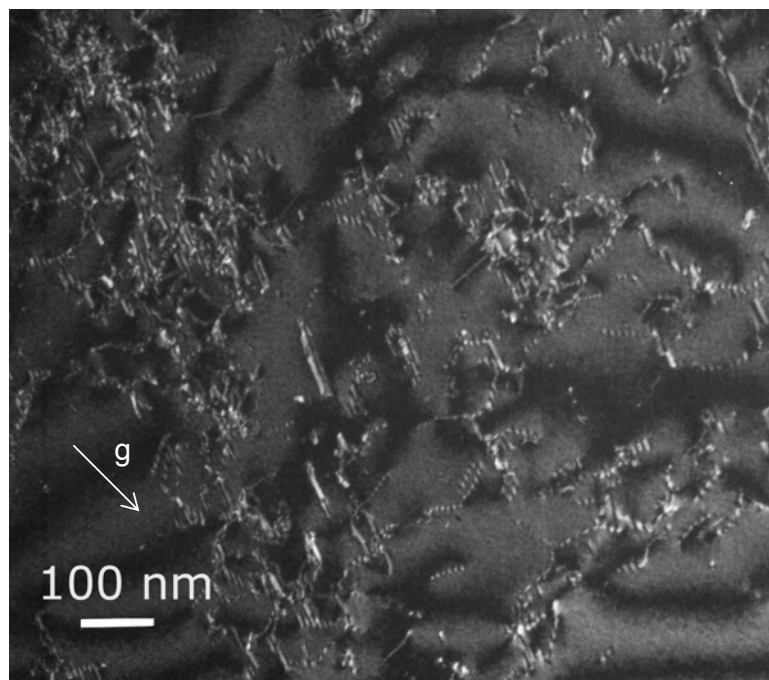
Figure 3.62. Weak-beam image g(3g), g {200}, close to a zone axis <011>, of the low dose in-service (Block A) HAZ (near the fusion line) irradiated to 1.3x10^{-5} dpa.
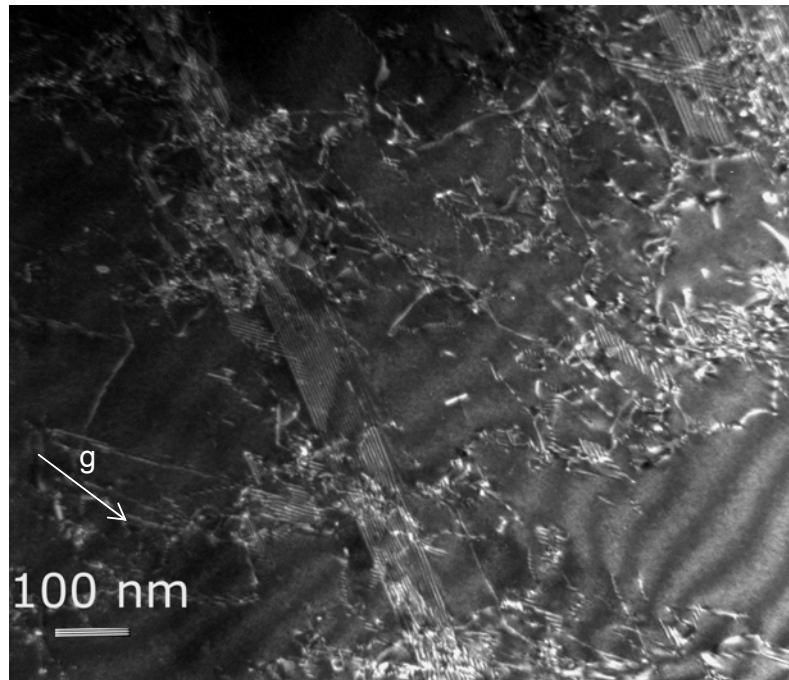
Figure 3.63. Weak-beam image g(6g), g {200}, close to a zone axis <011>, of the low dose in-service (Block A) HAZ (near the fusion line) irradiated to $1.3x10^{-4}$ dpa.

Table 3.18. Dislocation density versus dose for the BM and the HAZ of the low dose in-service material (Block A).

Low dose in-service material (Block A)	Dislocation density [$*10^{10}$ cm^{-2}]	
	BM	HAZ
$1.3x10^{-5}$ dpa	3.8	4.68
$1.3x10^{-4}$ dpa	4.6	7.6
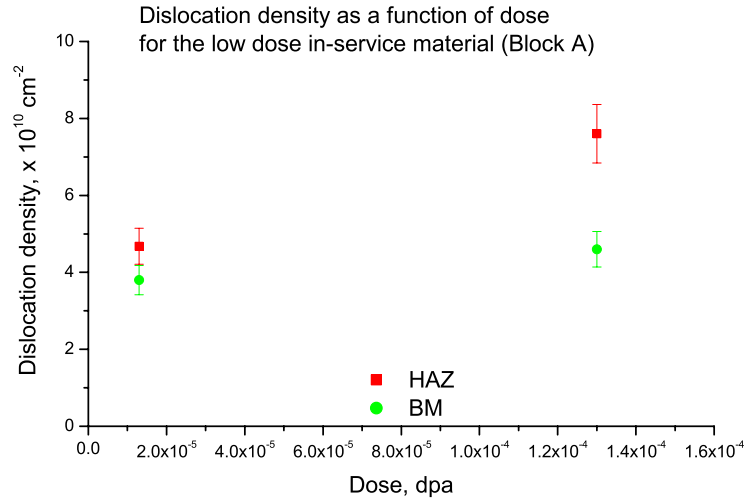
Figure 3.64. Dislocation density as a function of dose for the BM and HAZ of the low dose in-service material (Block A).

Weak beam dark field TEM observations were also performed on the high dose in-service material (Block B). Weak beam images of the high dose in-service (Block B) BM, far away from the fusion line (at about 4 mm), and irradiated to 0.12 dpa and 0.35 dpa are shown in Figure 3.65 and in Figure 3.66, respectively. Weak beam images of the high dose in-service (Block B) HAZ, close to the fusion line, and irradiated to 0.12 and 0.35 dpa, are presented in Figures 3.67 and 3.68, respectively.

Irradiation to doses up to 0.12 dpa leads to the apparition of additional defects, with respect to the unirradiated material, such as black dots and dislocation loops. With the dose increasing up to 0.35 dpa, the density of irradiation-induced defects increases.

The defect size distribution for the BM (far away from the fusion line) irradiated to 0.12 and 0.35 dpa is shown in Figure 3.69. For the HAZ irradiated to 0.12 dpa and 0.35 dpa, the defect size distribution is reported in Figure 3.70. The defect density and the mean size values are summarized in Table 3.19 for both the base material and the heat affected zone and both irradiation conditions.

Figures 5.71 and 5.72 present the defect density and size as a function of irradiation dose for both HAZ and BM. It can be seen that the loop density increases with increasing dose in the HAZ and remains constant with dose in the BM. The density of black dots decreases with increasing dose in the HAZ and remains constant with dose in the BM. The mean loop size decreases with increasing dose in both the HAZ and the BM, while the mean size of black dots remains more or less constant. The total defect density increases with irradiation dose, in both the BM and the HAZ. The defect density is higher in the HAZ, as compared to the BM, for both irradiation conditions.
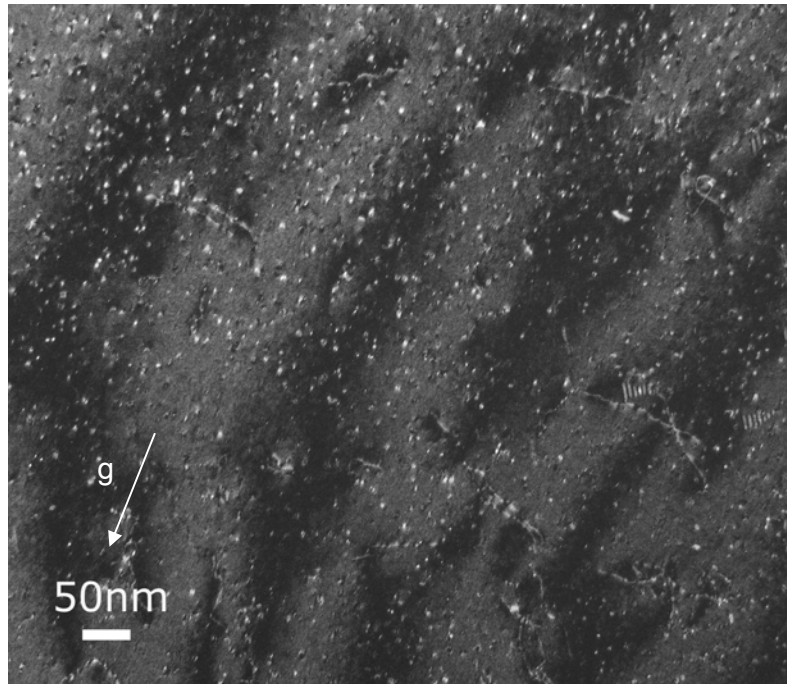
Figure 3.65. Weak-beam image g(5g), g {200}, close to a zone axis <011>, of the high dose in-service (Block B) BM (far away from the fusion line) irradiated to 0.12 dpa.
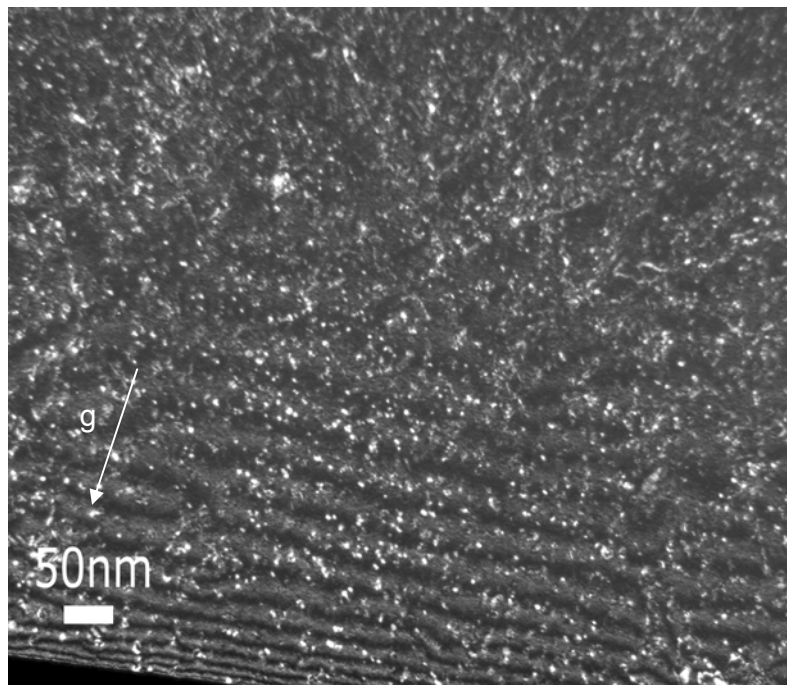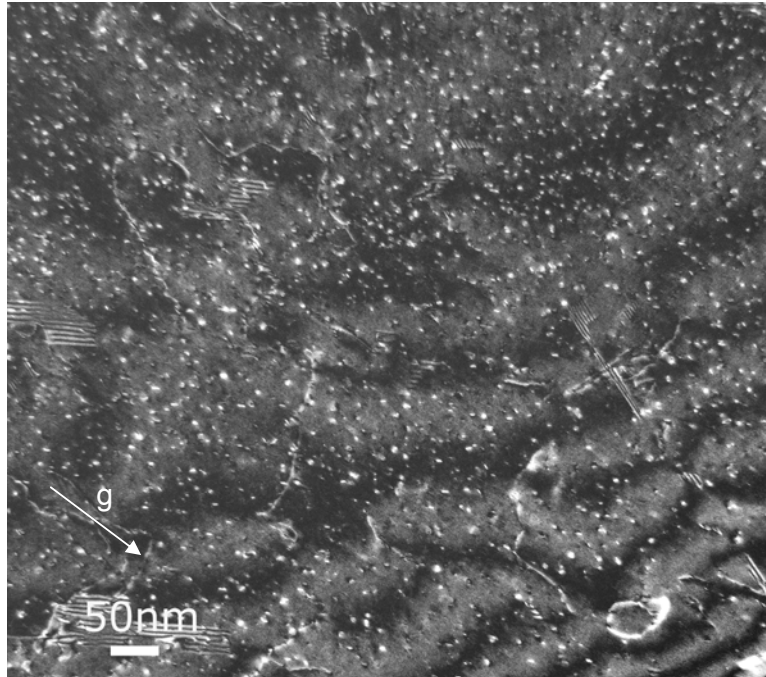

Figure 3.66. Weak-beam image g(5g), g {200}, close to a zone axis <011>, of the high dose in-service (Block B) BM (far away from the fusion line) irradiated to 0.35 dpa.

Figure 3.67. Weak-beam image g(5g), g {200}, close to a zone axis <011>, of the high dose in-service (Block B) HAZ (near the fusion line) irradiated to 0.12 dpa.
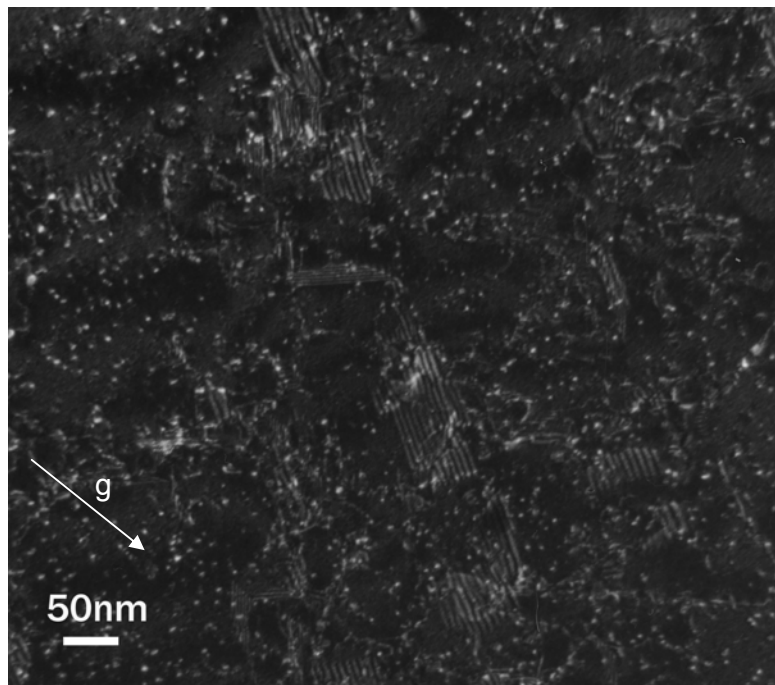
Figure 3.68. Weak-beam image g(5g), g {200}, close to a zone axis <011>, of the high dose in-service (Block B) HAZ (near the fusion line) irradiated to 0.35 dpa.

a)   b)
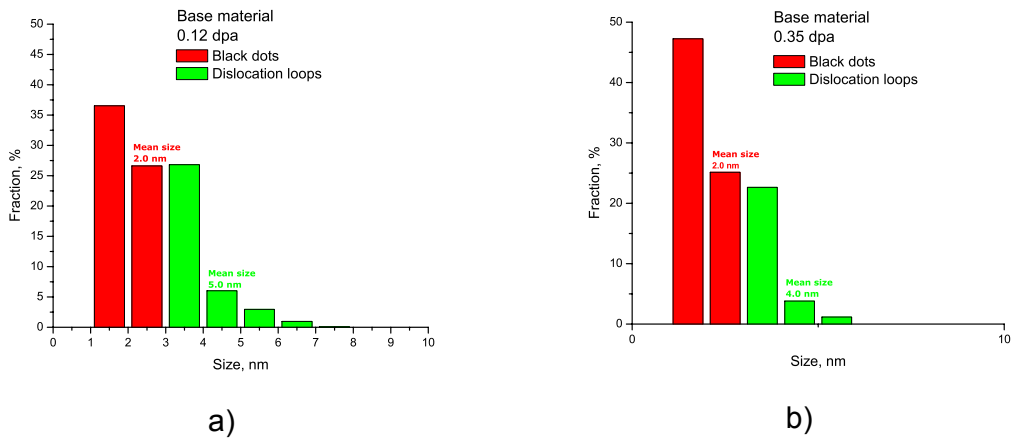
Figure 3.69. Irradiation-induced defect size distribution for the high dose in-service (Block B) BM (far away from the fusion line) irradiated to (a) 0.12 dpa and (b) 0.35 dpa.

a)   b)
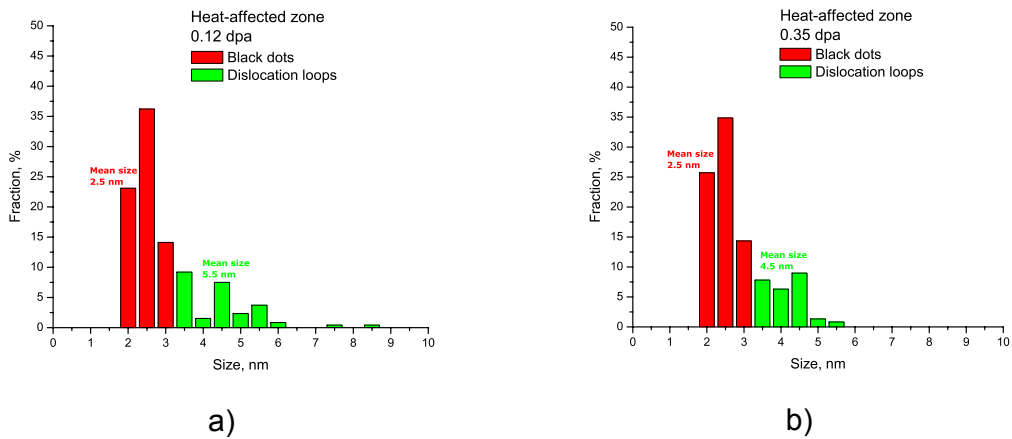
Figure 3.70. Irradiation-induced defect size distribution for the high dose in-service material (Block B) HAZ (close to the fusion line) irradiated to (a) 0.12 dpa and (b) 0.35 dpa.
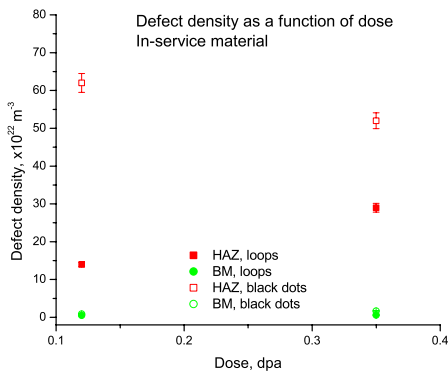
Figure 3.71. Defect density as a function of dose for the in-service material Block B, BM and HAZ.
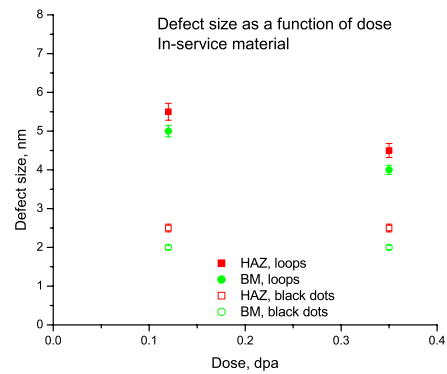
Figure 3.72. Defect size as a function of dose for the in-service material Block B, BM and HAZ.

Table 3.19. Defect density and mean size versus dose for the BM and HAZ of the high dose in-service material (Block B).

Specimen	Black dots		Dislocation loops		Total
	density [m^{-3}]	mean size [nm]	density [m^{-3}]	mean size [nm]	
BM 0.12 dpa	9.0×10^{21}	2.0	5.7×10^{21}	5.0	1.5×10^{22}
BM 0.35 dpa	1.7×10^{22}	2.0	6.7×10^{21}	4.0	8.4×10^{22}
HAZ 0.12 dpa	6.2×10^{23}	2.5	1.4×10^{23}	5.5	7.7×10^{23}
HAZ 0.35 dpa	5.2×10^{23}	2.5	2.9×10^{23}	4.5	8.0×10^{23}

3.4.2 Microstructure of deformed materials

3.4.2.1 Unirradiated test materials

TEM observations were performed on deformed specimens from the test weld materials. Figures 3.73 and 3.74 show the microstructure of the AISI 304 and AISI 347 base materials, following deformation at 293 K and 573 K, respectively.

a)   b)
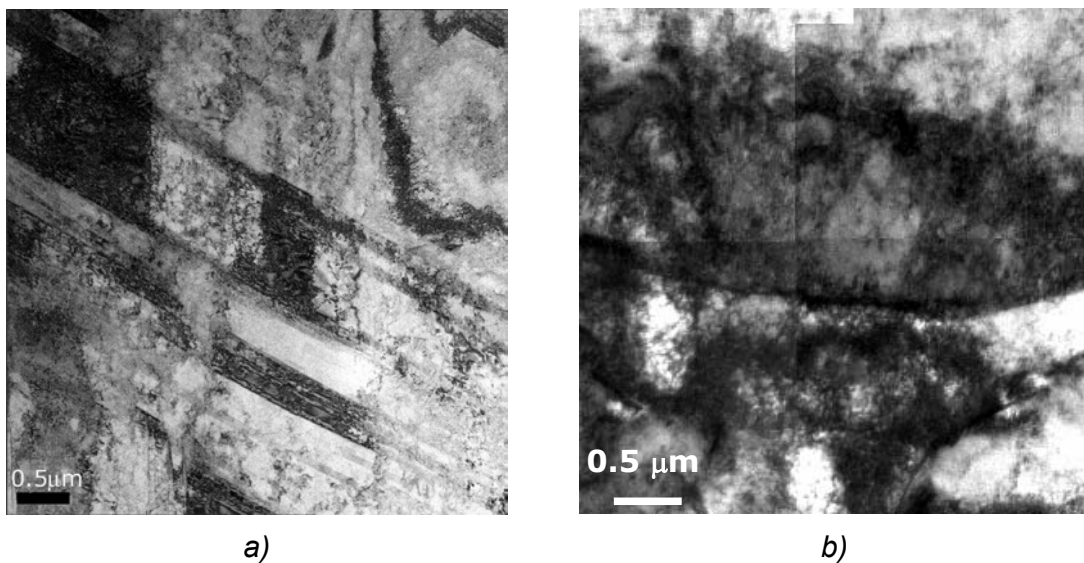
Figure 3.73. Bright field TEM images of AISI 304 tested at a) 293 K and b) 573 K.

<center>

a)   b)

</center>
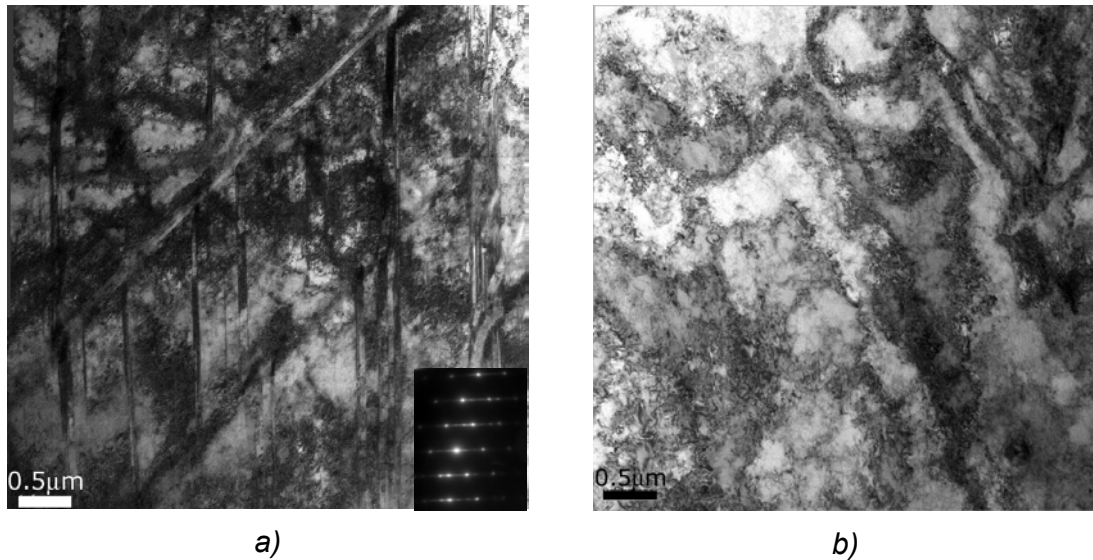
Figure 3.74. Bright field TEM images of AISI 347 tested at a) 293 K and b) 573 K.

Following tensile testing at room temperature the microstructure contains mainly twins. The twins are in {111} planes along <110> directions, as it was deduced from diffraction patterns as the one inserted in Figure 3.74.a.

Following tensile testing at high temperature the microstructure appears composed of dislocation cells.

The same deformation behaviour was observed for the HAZs of both materials, at both testing temperatures.

3.4.2.2 Irradiated test materials

The deformation mode of both irradiated test materials was studied by means of TEM. The deformation mode was found to present no significant dependence on the material, the irradiation dose and the test temperature. In all cases, the microstructure of irradiated test materials exhibits twins and stacking faults. For example, the deformation microstructure of 0.3 dpa AISI 304 close to the fusion line is shown in Figure 3.75.a, following room temperature deformation and in Figure 3.75.b, following high temperature deformation. Stacking faults and twins are present at both deformation temperatures. Figure 3.76 shows the microstructure of AISI 347 irradiated up to 1 dpa and deformed at room temperature (Figure 3.76.a) and at high temperature (Figure 3.76.b). The same microstructural features, stacking faults and twins, are observed at both deformation temperatures.
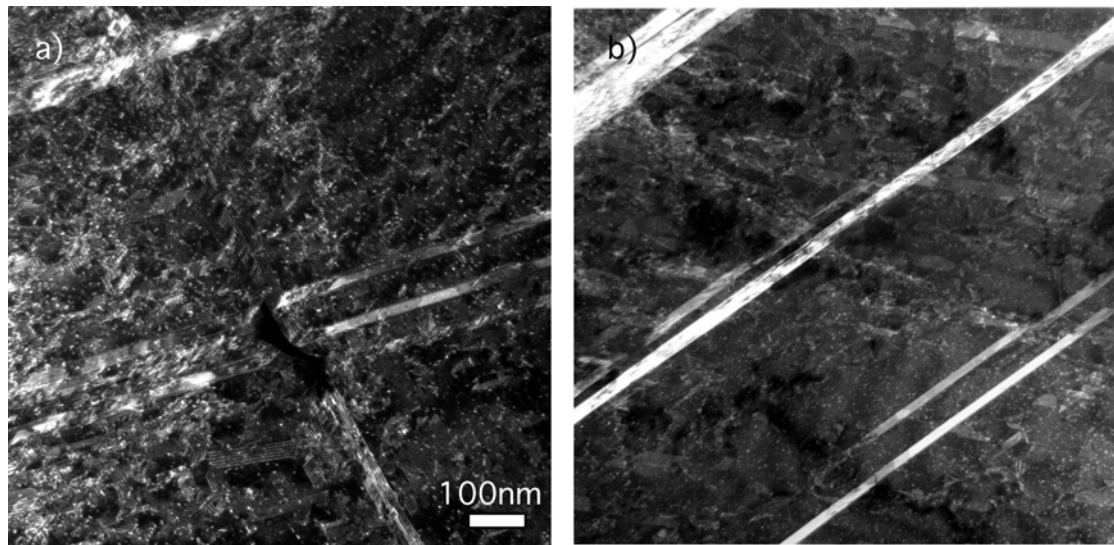
Figure 3.75. Bright field images of 0.3 dpa AISI 304 close to the fusion line deformed at a) 293 K and b) 573 K.
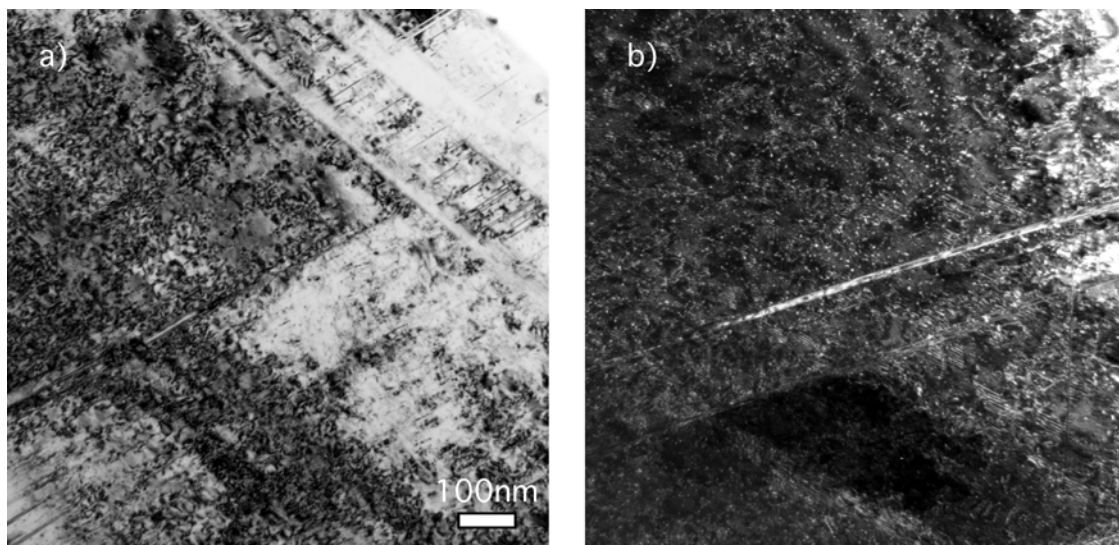

Figure 3.76. Bright field images of 1 dpa AISI 347 a) far away from the fusion line deformed at 293 K and b) close to the fusion line deformed at 573 K.

109

3.4.2.3 In-service material

TEM observations were performed on deformed specimens from the in-service material, Block A and Block B. Figures 3.77 and 3.78 show the microstructure of the low dose in-service material, Block A, BM and HAZ, and of the high dose in-service material, Block B BM and HAZ, respectively, at both deformation temperatures.

Following tensile testing at both temperatures the microstructure contains stacking faults and twins, as in the case of the irradiated test weld materials, whatever the distance from the fusion line.
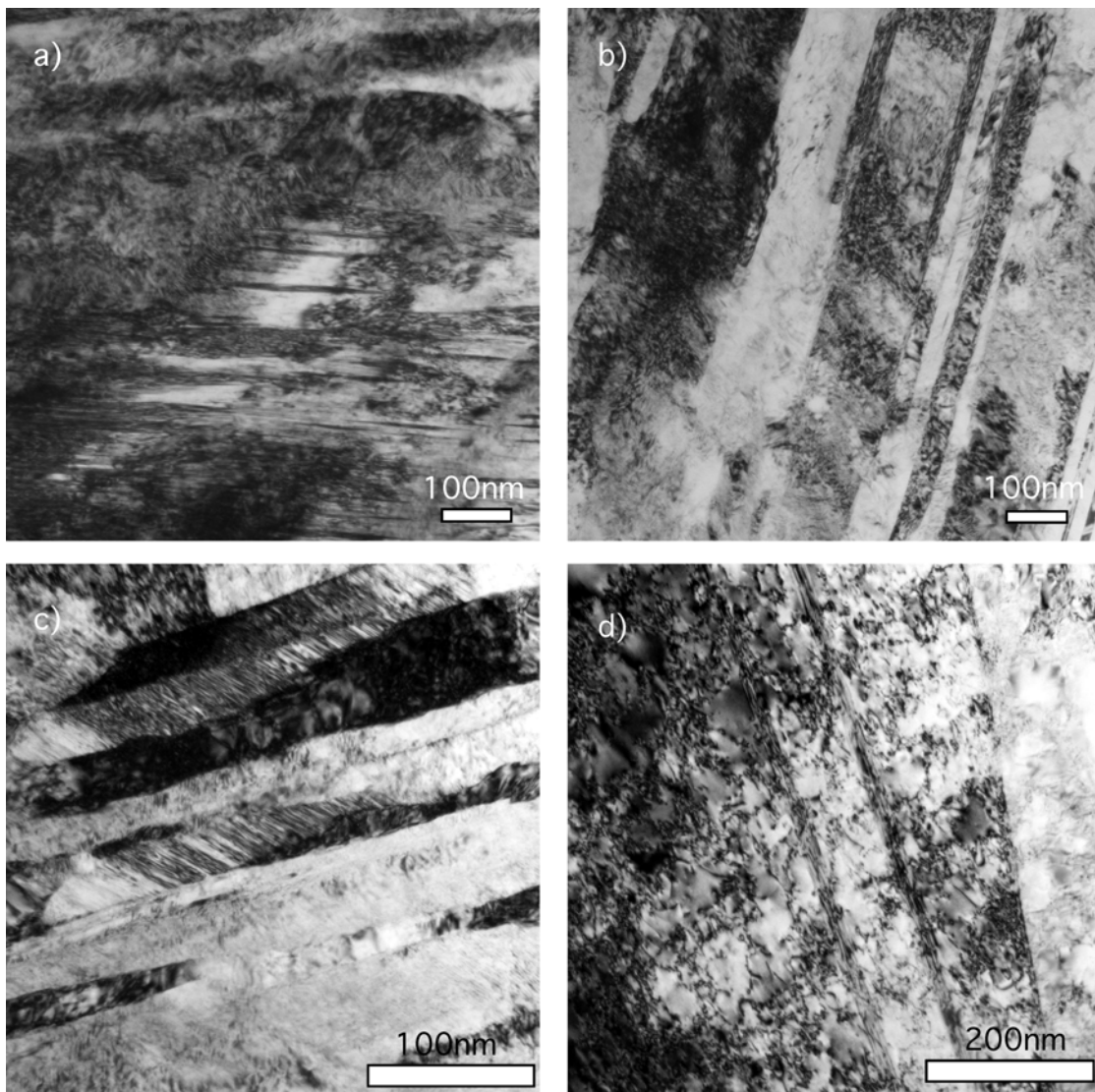
Figure 3.77. Bright field images of the low dose in-service material (Block A).
a) BM tested at 293 K, b) BM tested at 573 K, c) HAZ tested at 293 K, d) HAZ tested at 573 K:
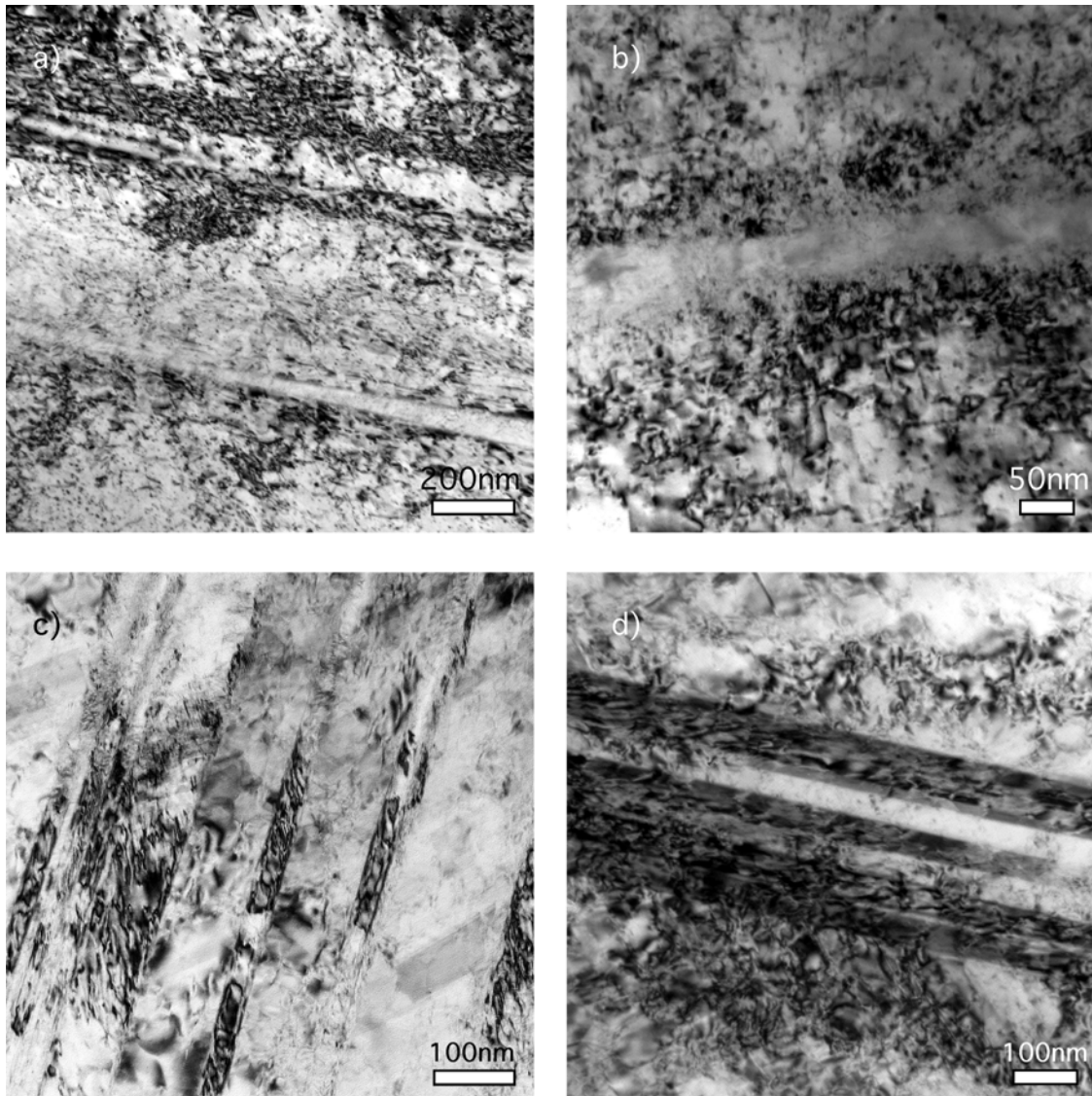
Figure 3.78. Bright field images of the low dose in-service material (Block B).
a) BM tested at 293 K, b) BM tested at 573 K, c) HAZ tested at 293 K, d) HAZ tested at 573 K:

CHAPTER 4

DISCUSSION

The experimental results are discussed in four sections: the microstructure of unirradiated materials, neutron irradiated materials and/or deformed materials, the mechanical properties of unirradiated and neutron irradiated materials, the relationships between the microstructure and the mechanical properties, and the integration of the obtained results within the INTERWELD project.

4.1 Microstructure

4.1.1 Undeformed unirradiated microstructure

The microstructure of the two welded austenitic stainless steels AISI 304 and AISI 347 in various states was fully characterised in order to identify the eventual changes of the microstructure after welding and/or after irradiation and how they relate to the eventual changes in mechanical properties.

The optical microscopy observations showed that the microstructure of both base materials in the unirradiated state is composed of equiaxed grains with twins. The welding process causes melting of the material, forming the so-called weld metal. Upon solidification, primary delta ferrite crystals initially form from the melt. Depending on the chromium and nickel contents, γ crystals also precipitate from the melt apart from the δ crystals, in the three phase sector (L + γ + δ), as it is shown in the phase diagram in Figure 4.1. After the solidification has been completed, the transformation of δ ferrite into austenite begins. Depending on the chemical composition of the material and the welding conditions, a certain amount of ferrite remains in the weld after solidification. The amount of ferrite retained in the weld metal was determined using the WRC – 1992 (Welding Research Council) solidification diagram [58], shown in Figure 4.2. The WRC solidification diagram converts the alloy composition into two factors, chromium equivalent (Cr_{eq}) and nickel equivalent (Ni_{eq}) [59]. The former relates to the alloying elements that are ferrite stabilisers, and the later relates to the alloying elements that are austenite stabilisers, according to the following formulae:

$$Cr_{eq} = Cr + Mo + 0.7Nb \qquad\qquad\qquad (4.1)$$
$$Ni_{eq} = Ni + 35C + 20N + 0.25Cu \qquad\qquad (4.2)$$

where the elemental symbols refer to the alloying elements, in weight percent (wt. %).

The calculated values are 19 for the chromium equivalent factor and 11 for the nickel equivalent factor for both AISI 304 and AISI 347, which corresponds to a ferrite number of 8, according to Figure 4.1, and thus to a concentration of 7.6 % ferrite in the austenitic weld metal. The residual delta ferrite is usually enriched with chromium and depleted with nickel, due to segregation phenomena during solidification [60].

Adjacent to the weld metal, the so-called heat affected zone is formed. This region has undergone microstructural changes because of the high temperatures reached during the welding process (Figure 4.1). The microstructural changes are reflected by the larger grain size in the heat affected zone as compared to the base material, and by the presence of small amounts of residual ferrite, as observed in TEM. The amount of ferrite in the heat affected zone was determined from the TEM images to be about 3 % in the austenite matrix, for both AISI 304 and AISI 347. The ferrite islands have dimensions between 2 and 12 µm. EDS measurements performed in TEM revealed a higher chromium and a lower nickel content in the residual ferrite as compared to the surrounding matrix (§3.4.1.1). The ferrite formed in the heat affected zones influences the irradiation-induced microstructure and the mechanical

properties, as it will be further discussed. These results are in good agreement with the data found in literature for welded austenitic stainless steels containing residual ferrite due to the welding process [94 – 96].

The successive heating and cooling phenomena that take place in the heat affected zone during the welding process introduce mechanical stresses in the material, reflected by the higher dislocation density in the heat affected zone as compared to the base material. The dislocation density measured from TEM images in the austenite matrix was found to decrease from 13×10^9 cm^{-2} in the heat affected zone to 3×10^9 cm^{-2} in the base material for AISI 304 and from 9×10^9 cm^{-2} in the heat affected zone to 1×10^9 cm^{-2} in the base material for AISI 347.
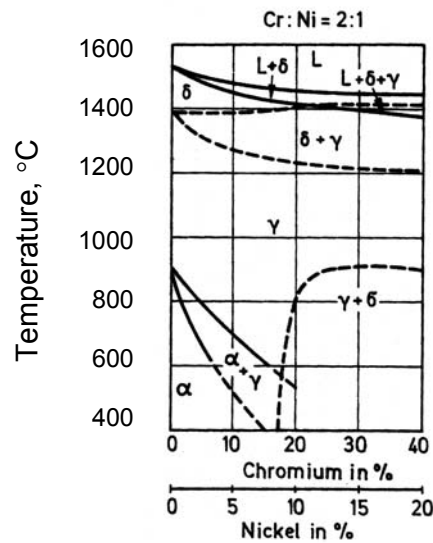
Figure 4.1. Ternary iron-chromium-nickel phase diagram for a chromium : nickel ratio of 2:1 [60].
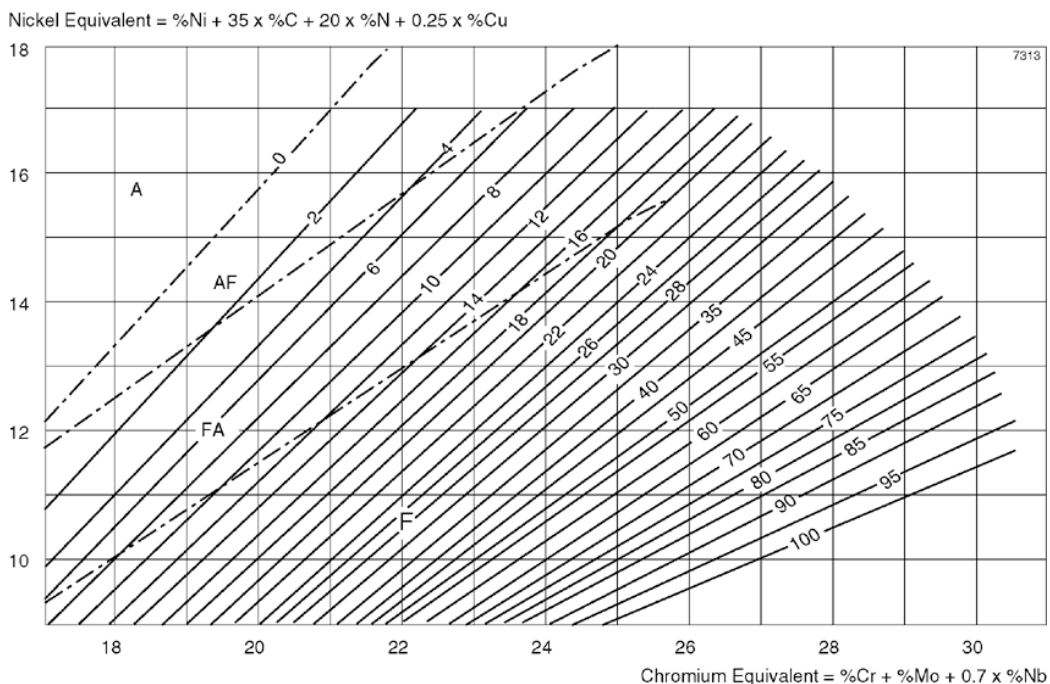
Figure 4.2. WRC – 1992 solidification diagram, according to [59].

115

4.1.2 Deformed unirradiated microstructure

Plastic deformation occurs by propagation of dislocations and hence the critical shear stress on the onset of plastic deformation is the stress required to move dislocations [61]. Extensive studies on the deformation mechanisms of austenitic stainless steels have been performed. It is clear from the literature that at low temperatures fully developed twins as well as widely dissociated dislocations, enclosing stacking fault ribbons, are present in the deformed materials [62 – 64]. At higher temperatures (above 200°C) the deformation microstructure consists of entangled dislocations along with stacking faults. As the deformation tends to operate in planes with the closest atomic packing, in fcc austenitic stainless steels dislocation slip occurs in the {111} planes, in the <110> directions.

TEM observations performed on deformed materials (§ 3.4.2.1) revealed that at room temperature twinning contributes significantly to the deformation process, while at high temperature perfect dislocation motion prevails, for both AISI 304 and AISI 347. There is no significant difference between the deformation mechanism taking place in the heat affected zones and the one operating in the base materials.

By calculating the strain hardening all along the true stress-true strain curves, it was found that a single strain hardening stage takes place in the plastic deformation regime, which suggests that a single deformation mechanism is operating in that regime. This observation holds for the BMs and HAZs of both materials, at both deformation temperatures.

4.1.3 Undeformed irradiated microstructure

In the literature the irradiation-induced defects in austenitic stainless steels are classified as black dots, dislocation Frank loops and cavities, their density and size depending on the irradiation conditions. Black dots refer to the irradiation-induced defects that are too small to be resolved in TEM. These contrasts may stem from any type of structural defects, such as 3D agglomerates of vacancies, interstitials, secondary phase precipitates, or a combination of those, which size is typically smaller than 1 to 2 nm. Figures 4.3 – 4.6 present the data on defect density and size found in the literature for different austenitic stainless steels and different irradiation conditions [32 – 35, 44, 63, 65 – 67]. The irradiation-induced defect densities measured for the materials studied in the present work are also included in the graphs.

As it can be seen in Figure 4.3 the Frank loop densities found in the literature present a large scatter. This is probably due to the different irradiation particles used, the different materials and different irradiation temperatures investigated. In the low temperature irradiation regime (from about 50°C to about 300°C), the densities of radiation-induced defects detected in TEM are almost independent of the irradiation temperature [84], and therefore these values can be more easily compared. It is well established in the literature that the irradiation-induced loop density increases with increasing irradiation dose and reaches a saturation level at about 1 dpa, to values of about 2 to 4 x10^{23} m^{-3}. it seems that the loop mean size ranges between 1 and

20 nm, with a saturation level appearing at about 2 to 3 dpa with loop sizes of about 9 nm, as shown in Figure 4.5. The black dot density seems to saturate at about 4 x10^{23} m^{-3} from about 1 dpa, as it can be seen in Figure 4.4. From Figure 4.6 it can be concluded that the black dot size remains constant, at about 2 nm, whatever the irradiation dose.

Note that in the present study no cavities have been observed, contrary to the observations of Edwards [35], certainly due to the lower irradiation temperatures investigated here.

The densities and sizes of Frank loops and black dots reported in the present study tend to agree with the published data, at least for the test materials AISI 304 and AISI 347 irradiated up to 0.3 or 1 dpa, as well as for the in-service base material. The densities of both Frank loops and black dots appear higher in the heat affected zone of the in-service material when compared to most of the literature data. Other authors have also found high loop densities in weld materials as compared to base materials in different welded austenitic stainless steels [95, 97 – 99].

The absence of TEM observable irradiation-induced defects in the ferrite phase can be related to the lower defect accumulation rate in the bcc (ferrite) structures with respect to the fcc (austenite) structures under irradiation. At low irradiation temperatures, below recovery stage V, the microstructure of irradiated bcc is dominated by micro-voids and voids [101, 102], which can be better resolved using the positron annihilation technique.
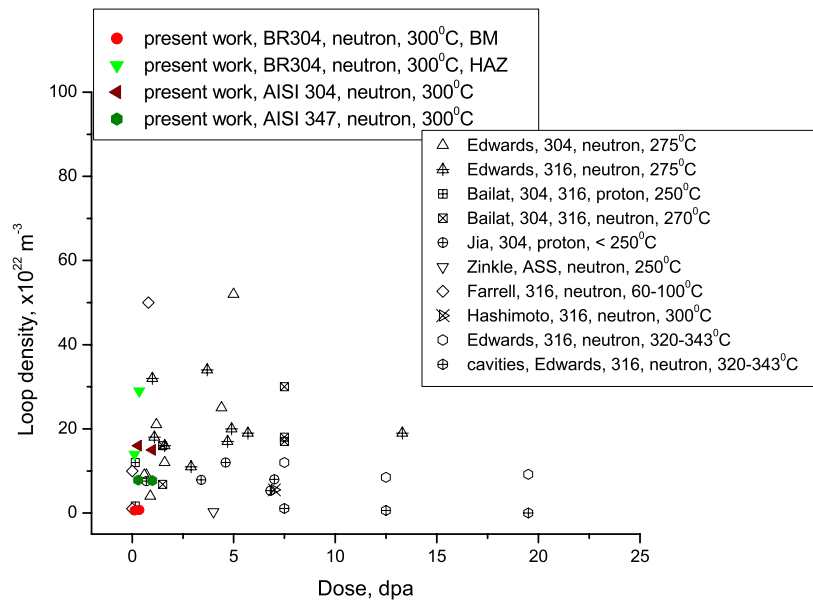

Figure 4.3. Frank loop density dependence with dose for austenitic stainless steels; comparison with the literature data.
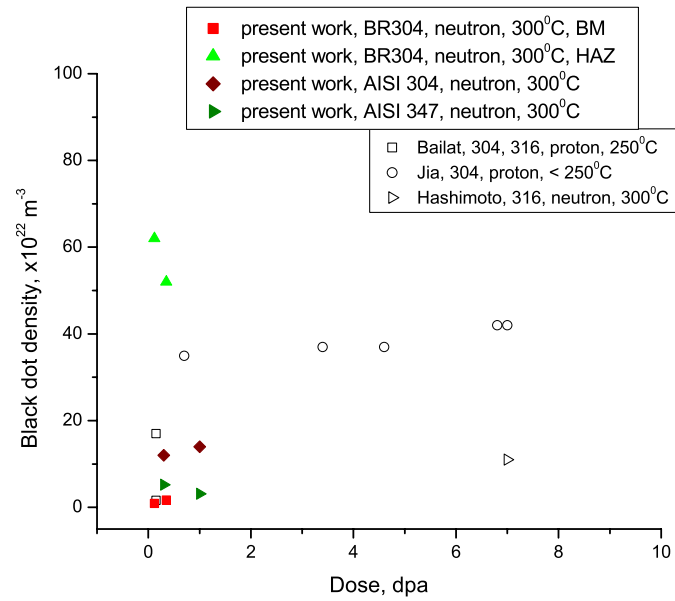
Figure 4.4. Black dot density dependence with dose for austenitic stainless steels; comparison with the literature data.
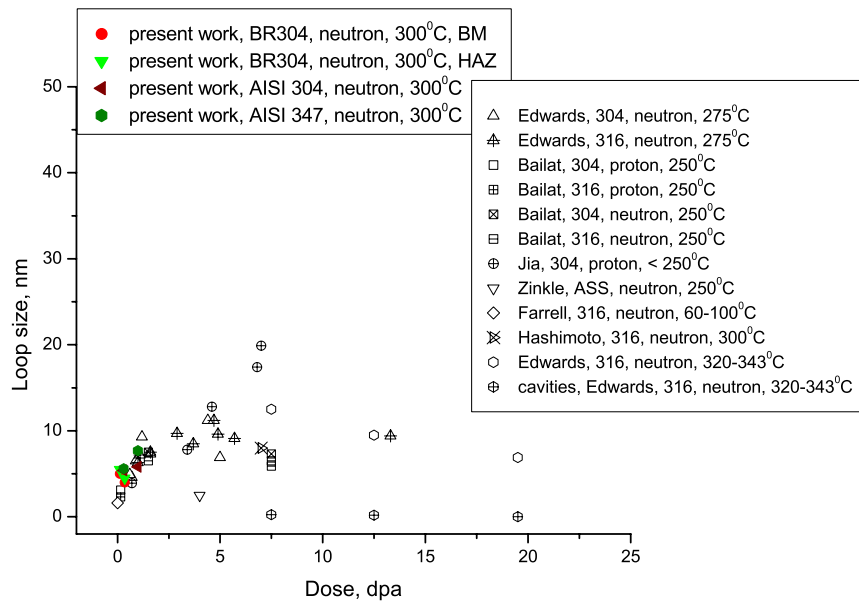

Figure 4.5. Frank loop size dependence with dose for austenitic stainless steels; comparison with the literature data.
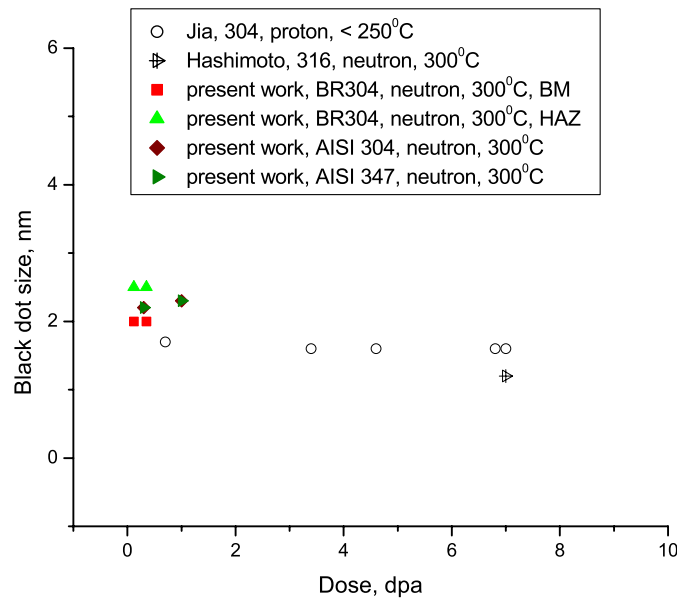
Figure 4.6. Black dot size dependence with dose for austenitic stainless steels; comparison with the literature data.

In the literature, the nature of the small irradiation-induced defects in the stainless steels is rather controversial. As a result from the atomic displacement cascades produced by impinging particles, interstitials, vacancies and clusters of those are produced in the lattice. There is a critical temperature of about 300°C, defining stage V, at which vacancy clusters become thermally instable and start to emit vacancies in the lattice [69]. This phenomenon explains that different damage microstructures are produced in stainless steels irradiated below or above that temperature. Below 300°C small defect clusters (black dots), dislocation loops (Frank loops) and some small precipitates are usually observed. No cavities have been observed at these irradiation temperatures. 'Black dots' have been postulated by some authors to be small Frank loops, of sizes of about 2 to 3 nm [35, 69]. This statement was, however, not confirmed by experimental observations. At irradiation temperatures above 300°C, the density of black dots decreases and clearly identified Frank loops become the predominant damage microstructure features.

For irradiation temperatures below 300°C it is postulated by some others authors that the identified Frank loops are interstitial in nature, while the black dots are predominantly of vacancy nature [63, 70 – 72]. More recent studies [35] contradict this statement and conclude that Frank loops with sizes in the range 1 – 30 nm can be either of vacancy or of interstitial type. In the present work, the nature of Frank loops has been investigated using the inside-outside contrast method [49]. The principle of the inside-outside contrast technique is illustrated in Figure 4.7. Dislocation loops of interstitial or vacancy nature (Figure 4.7.b) are imaged with either of the diffraction vectors shown in Figure 4.7.a, and a deviation parameter $s_g > 0$. The corresponding intensity profiles in the TEM images are plotted in Figure 4.7.c. The image peak may lie inside or outside the projected position of the dislocation core. The loop can then exhibit either an inside or an outside contrast,

depending on its nature, interstitial or vacancy, its inclination relative to the sense of g and the sense of g (Figure 4.7.d).
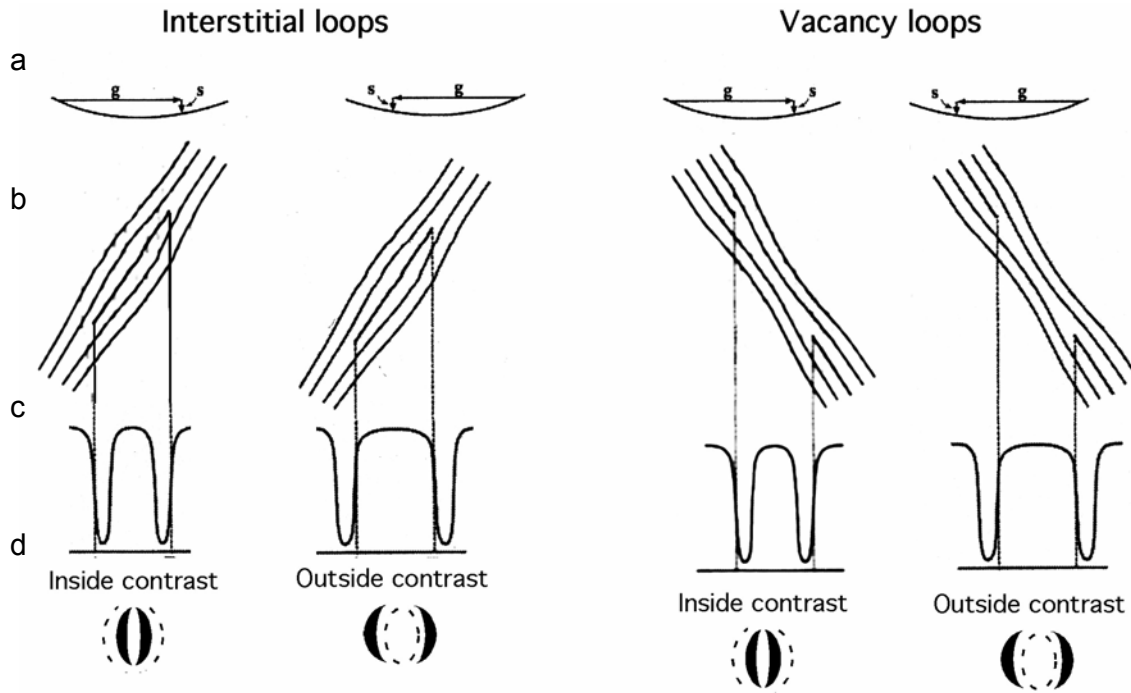

Figure 4.7. Schematics explaining the principle of the inside-outside contrast technique to identify dislocation loop nature using bright field TEM (after [49]): a) sense of the diffraction vector, b) strain field around the dislocation loop, c) intensity profiles derived from the strain field around the dislocation loop, d) the resulting contrasts in TEM images.

The difficulty in such a study arrives from the identification of the inside or outside contrast and from the identification of the inclination of the loop relative to the sense of the operating diffraction vector g. It also resides in the fact that the present irradiation-induced damage size is relatively small, which requires a very good optical quality. Weak beam dark field TEM is usually used as it allows the best resolution in diffraction contrast.

In order to identify the inclination of the habit plane of the loop, a pair of pictures are taken under exactly the same diffraction conditions (same g, same deviation parameter), but for different sample orientations. Usually a tilt of 10 to 20° is sufficient. A stereoscopic observation using both pictures allows one determining the orientation of the loops habit plane. In essence, it is the evolution of the width of the loop contrast from one picture to the other that allows determining its inclination.

Figure 4.8 shows two experimental weak beam dark field TEM images taken with a diffraction vector {200}, close to a zone axis <011>, under a slightly different angle. There is a tilt of about 10° between the two pictures in Figure 4.8.a and Figure 4.8.b. The corresponding diffraction vectors are inserted in the upper part of the images. The two upper loops marked by white arrows exhibit an outside contrast that is broader in Fig. 4.8.a than in Fig. 4.8.b, but the third one at the bottom of the image

exhibits a narrower contrast. It is concluded that the two upper loops are interstitial in nature, while the one at the bottom is made of vacancies. This analysis indicates that Frank loops can be either both interstitial or vacancy in nature. Horiki [100] found in an austenitic stainless steel type Fe-16Ni-15Cr irradiated at temperature 353 K to 2.5×10^{23} n/m^2 that 7 % of the defect clusters were of interstitial type and 93 % of vacancy type.
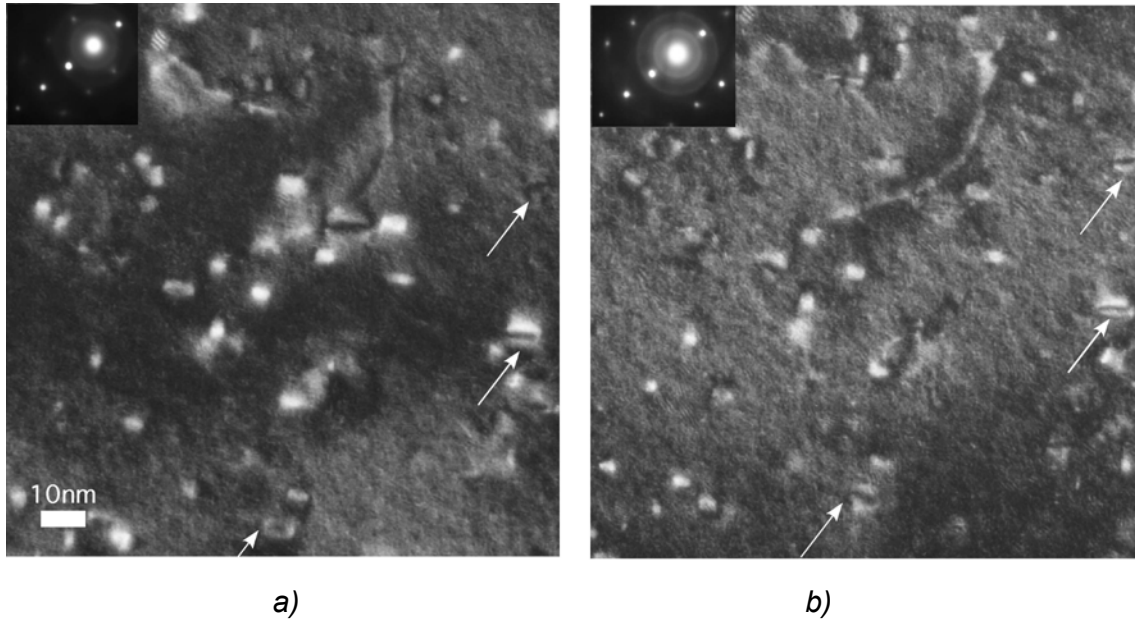

a)   *b)*

Figure 4.8. Weak-beam dark field TEM images, g(6g), g{200}, close to <011> zone axis of AISI 347 irradiated to 1 dpa, taken at two different tilt angles.

Stacking fault tetrahedra (SFTs) have also been observed [66 – 67, 73] in irradiated austenitic stainless steels usually in low densities (< 1 %). In the work of Horiki and Edwards [73, 34], a small fraction of SFTs with respect to the total irradiation-induced defect population has been observed in high purity Fe-Ni-Cr alloys. The SFTs reported by Zinkle [67] were observed in a Fe–17Cr–16.7Ni–2.5Mo alloy, but the alloy purity was not specified, nor the fraction of SFTs. In another study [85] Zinkle reported a small fraction of SFTs (< 0.2 %) in a solution-annealed type 304 L stainless steel irradiated with neutrons at 120°C up to 0.5 dpa. More surprising are the observations by Jia [66], who observed in an irradiated 304 steel a SFT density corresponding to about 20 to 25 % of the total density of defects.

In the present study, only a small amount of image contrasts that could stem from SFTs were identified. It should be noted that one faces here the problem of the interpretation of TEM images. In order to illustrate our discussion, Figure 4.9 shows examples of TEM images displayed at the same scale for various irradiated metals: pure copper (a) [68] and different types of austenitic stainless steels (b – d) [66 and present study]. These images were taken with a diffraction vector of the {200} type close to a zone axis of the <011> type. The white arrows indicate the contrast arising from a possible SFT. The geometry of SFTs leads to characteristic shapes of the interface separating the black and the white lobs, as it is clearly seen in pure copper, Figure 4.9.a. In austenitic stainless steels triangular-shaped contrasts can appear in

121

TEM pictures as a result of overlapping defects in the electron beam direction. Typically, when looking down a zone axis of the <011> type, Frank loops lying in {111} planes will appear edge-on for the two families of planes (e.g. (11-1) and (1-11)) containing the zone axis (e.g. [011]). The image contrast is then a well delineated straight segment, bounded on each side by a light contrast. When two of these loops are lying on two conjugate {111} planes containing the zone axis <011> and are located one above the other, the resulting contrast, actually composed of two straight segments touching each other, may have the appearance of a triangle (as the strong contrasts identified by black arrows in Figure 4.9.d). These contrasts may be then wrongly interpreted as stemming from SFTs. On the other hand, the size of the clusters relative to the effective extinction distance is very important when imaging in weak-beam. The contrast of defects smaller than the effective extinction distance in weak-beam imaging mode is very sensitive to the foil thickness, the depth of the defect in the foil and the deviation parameter. Variations in one of these parameters can lead to a very weak contrast, making the defect invisible. Another difficulty in determining the nature of SFT comes from the TEM image background, which relates to specimen surface and surface contamination. In pure metals, such as copper in Figure 4.9.a, the background shows a uniform contrast, while in alloys, such as austenitic stainless steels in Figures 4.9.b and Figure 4.9.c the background shows a rough contrast. When increasing the effective extinction distance, by using dark field imaging instead of weak beam, the situation improves slightly, as in Figure 4.9.d, at the expense of the spatial resolution.

In this view, a careful analysis has been performed in the present study in order to clarify this point. One example is shown in Figure 4.10, where two-beam dark field images of a small irradiation-induced defect in AISI 347 irradiated up to 1 dpa at 300°C were taken close to a <110> zone axis. In Figure 4.10.a, taken with a diffraction vector of the {200} type, the image contrast presents a triangular aspect. When the diffraction condition is changed to a diffraction vector of the {220} type the image contrast looses its triangular aspect, indicating that it cannot result from a SFT (Figure 4.10.b). The triangular appearance of the contrast is thought to be due to overlapping defects, as mentioned earlier, or to the asymmetrical strain field of a single defect of another type, whose contrast varies depending on the diffraction conditions, as suggested by Jenkins [49]. According to the Silcox and Hirsch model [86] the SFTs are formed by the dissociation of a triangular vacancy loop. On the basis of this model, Jenkins stated that loops may dissociate before they form triangular loops (Figure 4.11) and defines them as partially-dissociated Frank loops, whose defect structure is intermediate between a Frank loop and a SFT.
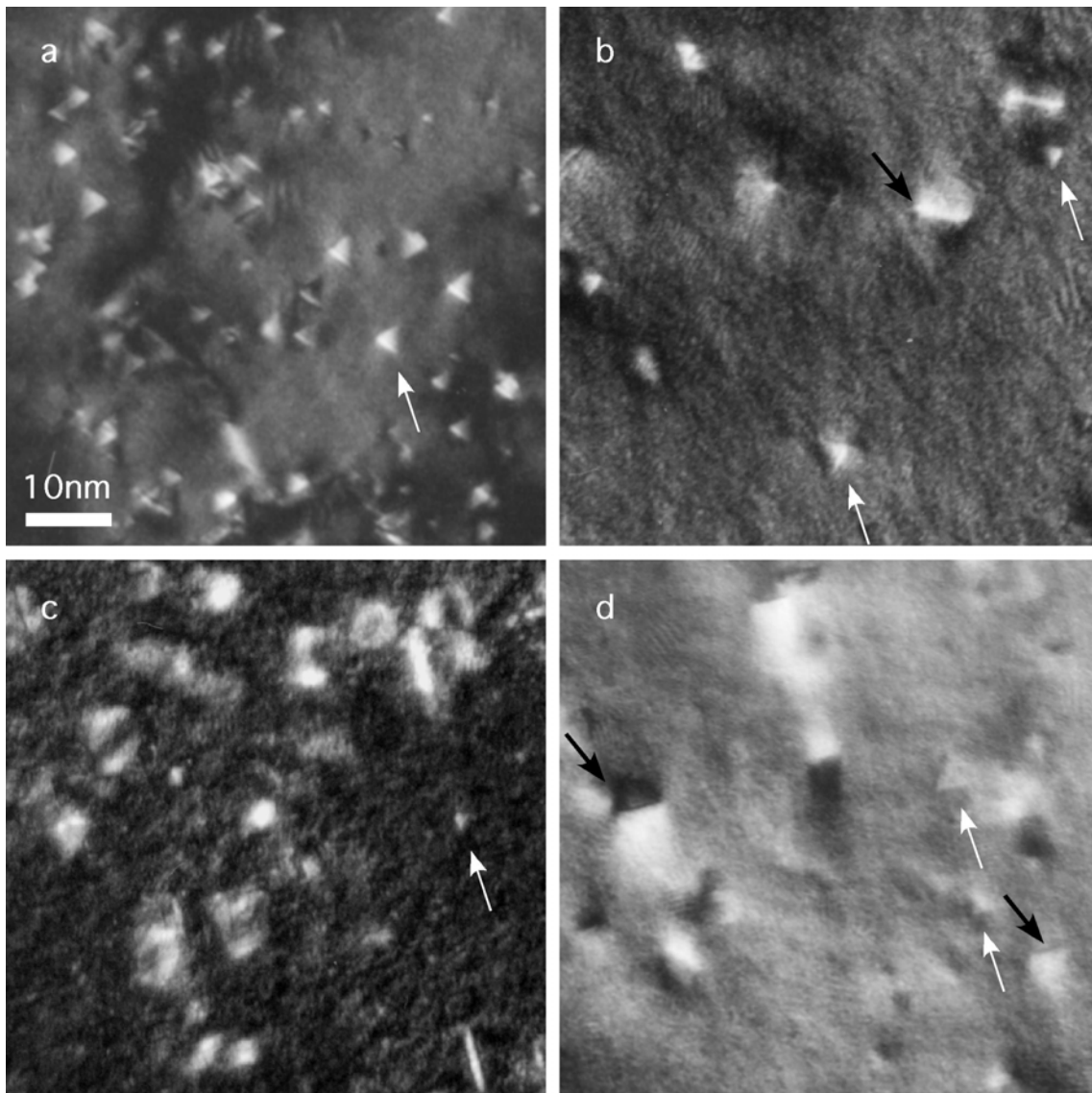
Figure 4.9. SFT contrast in dark field TEM pictures for different materials: a) pure copper, irradiated with protons to 10^{-2} dpa at room temperature, weak beam g(6g), g(200) [68]; b) AISI 304 irradiated to 3.2 dpa with protons at $T < 250\,°C$, weak beam g(6g), g(200) [66]; c) AISI 304 irradiated to 1 dpa with neutrons at $T \sim 300\,°C$, weak beam g(6g), g(200); d. AISI 347 irradiated to 0.3 dpa with neutrons at $T \sim 300\,°C$, dark field g(2g), g(200).
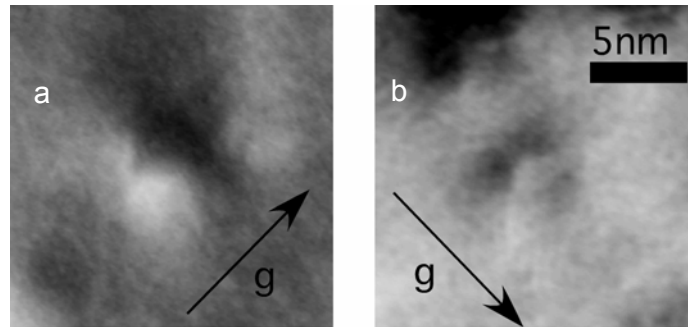
Figure 4.10. Strain field contrast of a small irradiation-induced defect imaged in two-beam dark field condition using a) a {200} reflection and b) a {220} reflection, close to a <110> zone axis.
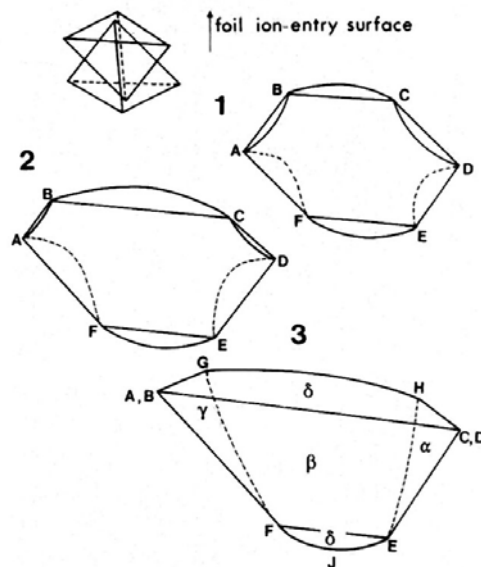
Figure 4.11. Schematic diagram of a partially dissociated Frank loop according to Jenkins [49].

In other fcc metals, like for example pure copper, the irradiation-induced microstructure contains about 90% of SFTs [87]. By comparing neutron-irradiated pure copper with neutron-irradiated copper alloys, Zinkle [83, 88] concluded that the fraction of SFTs in irradiated pure copper is larger than in its alloys. By considering the formation of SFTs directly from the vacancy-rich core of the displacement cascade region, the authors asserted that the lower density of SFTs in copper alloys may be due to the preferential binding of vacancies to solute atoms. Solely on the basis of the stacking fault energy and the shear modulus, one may infer that SFTs should also be the dominating feature in irradiated stainless steel [89]. Indeed, the stacking fault energy in Cu is about 45 mJ/m^2 and the shear modulus of Cu is 54.6 GPa [89], while in stainless steels the stacking fault energy is between 10 to 50 mJ/m^2 [90] and, according to § 3.4.1.1, it was found to be 38 mJ/m^2 for AISI 347 in the present study. The ratio of the stacking fault energy to the shear modulus times the Burgers vector ($\gamma/\mu \cdot b$) gives a value of 1/490 (using $\gamma = 38 \times 10^{-3}$ J/m^2, $\mu = 74.23 \times 10^9$ N/m^2, $b = 0.253 \times 10^{-9}$ m) which, according to Schäublin [89], should

favour the formation of SFTs, and this is actually not the case. A similar idea was proposed by Zinkle [83, 84] who suggested that copper alloys contain a smaller fraction of SFTs than pure copper, even their stacking fault energy is lower than in pure copper.

The scarcity or absence of SFTs in irradiated stainless steel may be rationalized in two different ways. One scenario consists in the premature partial dissociation of Frank loops, before they reach the triangular shape needed for the SFT formation, giving to the loop a waffle-like structure, as suggested by Jenkins. After reaching this shape, the loop morphology cannot evolve anymore so easily, as this would require the constriction of one or more of the dissociated edges in order to allow for the glide of the boarding dislocation to a triangular shape. The smaller stacking fault energy in stainless steels, relative to the one of Cu, would be in favour of such a premature dissociation. In the other scenario, it is suggested that impurities and alloying elements are altering the evolution of Frank loops towards SFTs. In alloys, due to the different atom sizes, the recoil collision sequences are less efficient than in pure metals, with uniform atom size. This can modify the displacement cascade process, in the sense that the interstitials and vacancies will not be effectively separated from one another and the vacancy-rich core may not develop so well [91]. Vacancies can preferentially migrate to solute atoms, reducing the possibility of SFT formation [88]. In addition, the differences in atomic radii, between the one of atoms of Fe and the one of other alloying elements, might be sufficient to locally impede the nucleation and/or the glide of the $1/6<112>$ Shockley partial necessary to unfold the stacking fault planes that are the premises of a nascent SFT.

Our investigation of the nature of Frank loops supports this analysis. The fact that Frank loops can be either interstitial or vacancy in nature explains the scarcity of the observed SFTs. The balance of point defects, interstitials and vacancies, produced in even quantities by the impinging particles can be maintained, as vacancies can be equally found in Frank loops, thus voiding the need for SFTs, which are intrinsically vacancy in nature.

Radiation-induced segregation to grain boundaries has been observed in neutron-irradiated austenitic stainless steels. Because segregation occurs in very narrow areas across grain boundaries, for a better determination of the grain boundary composition segregation models are used [74]. Experimental measurements have been made using analytical TEM and high-resolution field-emission-gun TEM. In the present study, electron dispersive X-ray spectroscopy (EDS) was performed in TEM for grain boundary analyses in the case of the in-service material heat affected zone irradiated up to 0.35 dpa. No clear segregation of the alloying elements was observed. Note that the interpretation of grain boundary segregation in TEM depends strongly on the grain boundary orientation. If the grain boundary is not perfectly edge-on, the eventual segregation profiles can not be exactly determined, considering that segregation of major alloying elements extends usually only over 5 to 10 nm along the grain boundary. So, no clear conclusion on the segregation at grain boundaries could be drawn from the present study.

4.1.4 Deformed irradiated microstructure

The deformation-induced microstructure of irradiated materials depends to a large extent on the microstructure that developed under irradiation. The deformation mechanism of irradiated pure metals and austenitic stainless steels has been widely studied, by a number of different authors. These studies indicate that deformation proceeds by the formation of defect free channels [65, 74], stacking faults and twins [66, 75, 76] or by a combination of those [79]. Defect free channels, as observed in deformed irradiated pure metals such as Cu or Pd [68], appear to be due to the sweeping, absorption and/or destruction of the irradiation-induced defects by the moving dislocations. Once the irradiation-induced defects have been destroyed or weakened by the passage of a first dislocation, subsequent dislocations that stem from the same source, may propagate more easily than in the surroundings that still contain the original defect microstructure. It should be noted that Byun [78] concluded that localised deformation, resulting from dislocation channeling, is a common mechanism occurring under high stresses, whether the material is irradiated or not. In other studies concerning channeling, the authors concluded that the channels are not completely free of defects, but contain a remnant density of Frank loops [44, 77, 78].

Song [75] suggested that the formation of twins in irradiated fcc materials with low stacking fault energy occurs by the unfaulting of Frank loops, following the intersection of more than one dislocation with a Frank loop. After a first dislocation interacts with the loop, two partials are formed. With more dislocations intersecting the loop, the partial dislocations are further separated. In materials with low stacking fault energy the unfaulting of the loop depends on the local shear stress. Because the attraction force between the two partials is large, a high energy is necessary to separate them. The low stacking fault energy in stainless steels eases the extension of the stacking fault and the formation of twins. Niewczas [80] explained the twin nucleation from Frank loops by Shockley partial dislocations bounding a stacking fault. The sequence of interaction between a dislocation and a Frank loop is shown in Figure 4.13. The (a/2) [101] dislocation gliding in the (11-1) primary plane interacts with the Frank loop along the [011] direction and leads to the formation of a (a/6) [121] partial dislocation, according to the reaction:

(a/2) [101] + (a/3) [-11-1] = (a/6) [121]
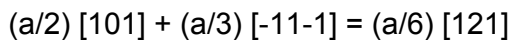
The (a/6) [121] Heidenreich – Shockley dislocation produces the shear displacement necessary to generate an intrinsic stacking fault in the (1-11) plane during deformation. This dislocation is pinned at the two nodes N_1 and N_2. Because the configuration is bounded by a sessile Frank loop, it can be activated under stress. Depending upon the position of the primary dislocation with respect to the twinning dislocation, four configurations of twinning sources (Figures 4.13.c – f) can be considered. The growth of the twin proceeds by the motion of a Shockley partial around the primary poles. The sessile Frank jog can act as stress barrier for the twinning source. If two twinning dislocations pass the sessile jog simultaneously, the stress barrier is reduced to zero. If only one dislocation passes, the twinning dislocation may get stack at the Frank jog, producing a block of undeformed matrix inside the twinned material.

In the present study, it was found that in the case of the in-service material deformation takes place mainly by twinning at both testing temperatures, for both BM and HAZ in the unirradiated and irradiated states. Together with twins, a large fraction of stacking faults is observed.

The deformation of both AISI 304 and AISI 347 test weld materials irradiated up to 0.3 or 1 dpa takes place by the formation of a mixture of twins and stacking faults, at both deformation temperatures, whatever the distance from the fusion line. The twins found in the deformation microstructure were studied more in detail. Figure 4.14 shows weak-beam dark field images of a twin imaged using two different diffraction conditions, close to a <110> zone axis. In Figure 4.14.a, taken with a {200} diffraction vector, the twin appears free of defects. Using a <111> diffraction vector, defects are clearly observed inside of the twin (Figure 4.14.b).

No defect free channels have been observed in any of the materials, at both testing temperatures.

b
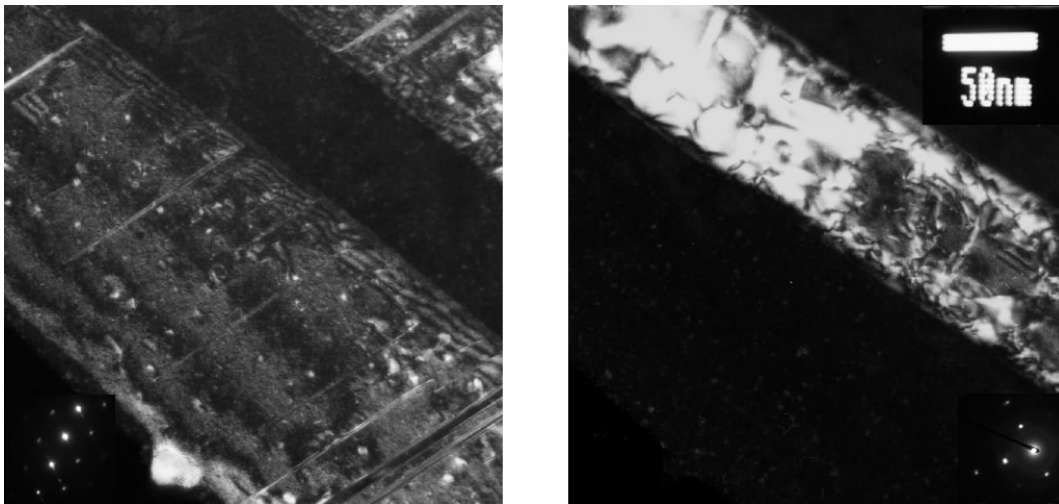
Figure 4.14. Weak-beam dark field images of AISI 304 close to the fusion line irradiated up to 1 dpa and deformed at room temperature. Twin imaged close to a {110} zone axis using a) a {200} and b) a {111} diffraction vector, as shown by the diffraction pattern inserted at the lower corner of each figure.
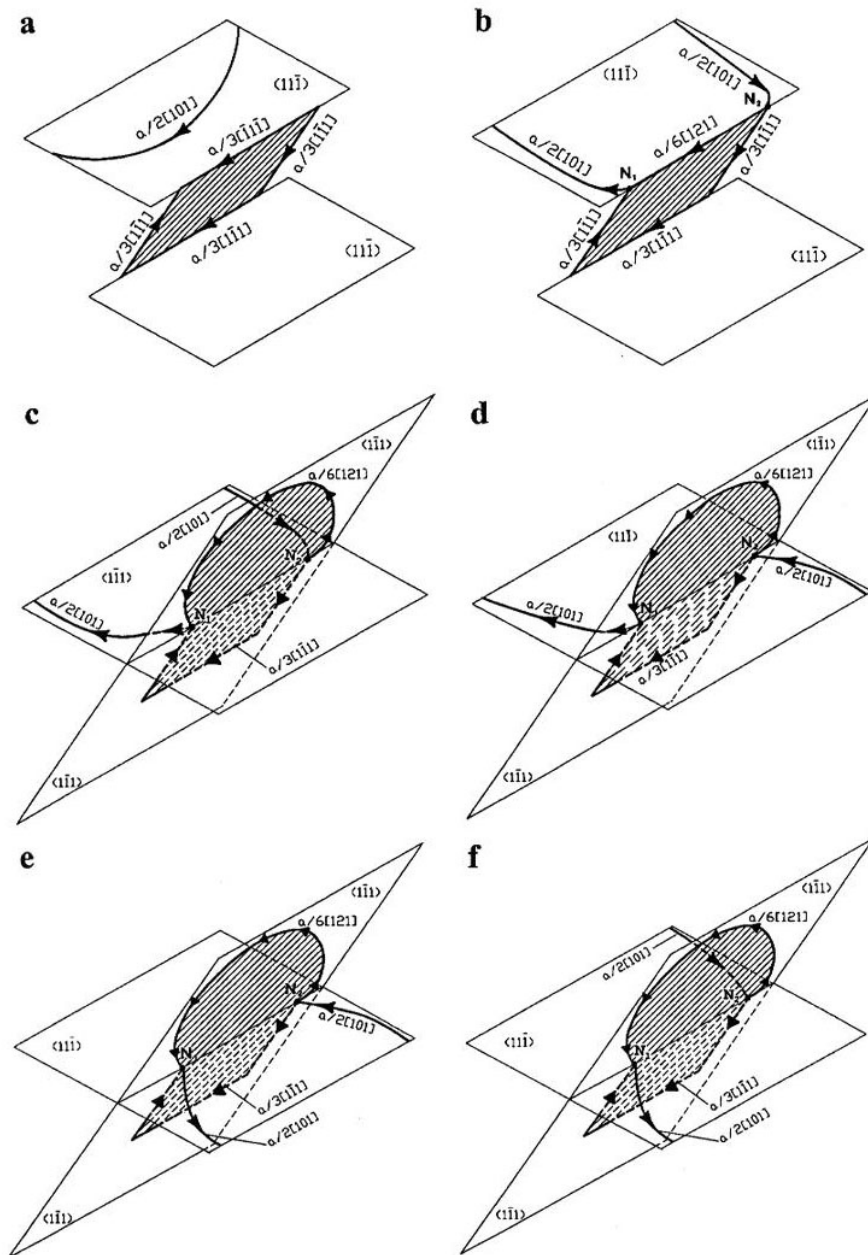
Figure 4.13. Sequential stages of the interaction of a dislocation with a faulted Frank loop [80].

An interesting feature concerning the deformation of irradiated heat affected zone is the behaviour of the bcc interphase. It seems that the twins are passing through the interphase without deforming it (Figure 4.15.a), or they are just stopped at the intersection with the interphase (Figure 4.15.b). Figure 4.16 shows a spatial representation of a dislocation glide plane intersecting the unshearable ferrite interphase.

a)   b)
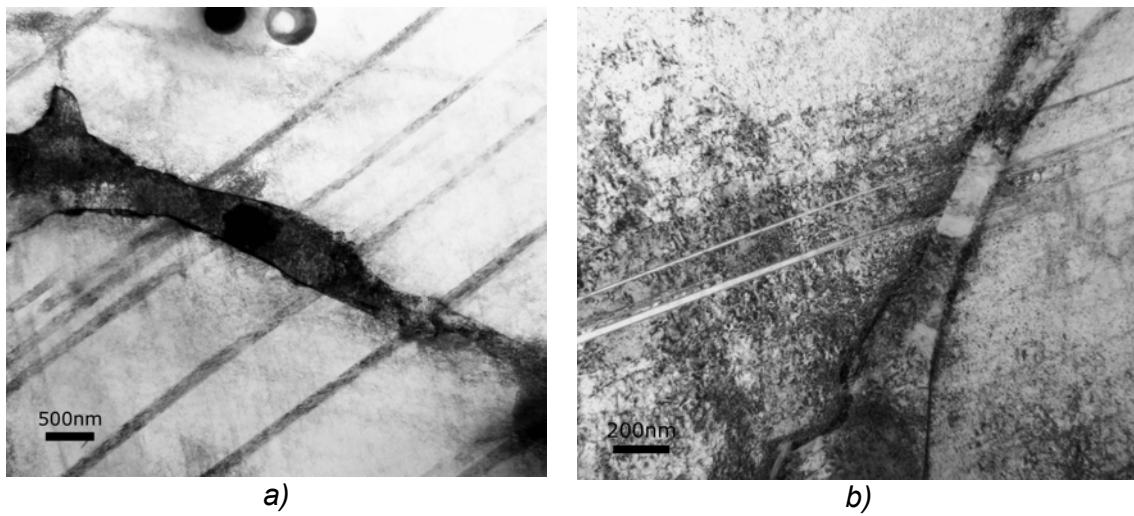
Figure 4.15. Intersection of twins with the bcc interphase in the case of AISI 347 close to the fusion line irradiated up to 0.3 dpa and deformed at room temperature, a) twins passing through the bcc structure and b) twins stopped at the intersection with the bcc structure.
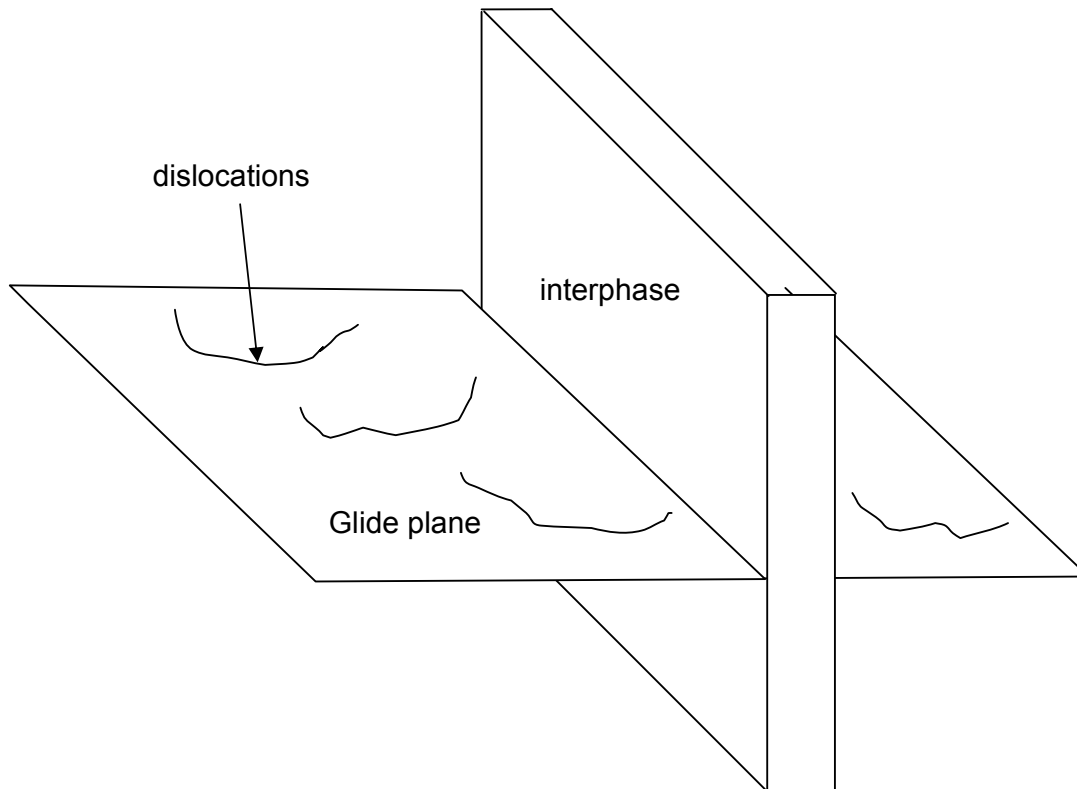
Figure 4.16. Spatial sketch of a dislocation glide plane intersecting the interphase.

4.2 Mechanical properties

4.2.1 Unirradiated materials

Tensile tests were performed on small specimens from the unirradiated base test materials, at two deformation temperatures: 273 K and 523 K. Table 4.1 shows the mechanical properties at room temperature found in the literature for both materials. The values obtained in the present study are comparable to those found in the literature, for both materials. From the experimental results (as well as from the literature), it is observed that the yield strength of AISI 347 is larger than that of AISI 304, while the UTS and the UE of AISI 304 present larger values than those of AISI 347. The mechanical properties of both test materials are decreasing with increasing test temperature.

Table 4.1. Mechanical properties of austenitic stainless steels at room temperature.

Type	Tensile Strength, MPa	Yield Strength, MPa	Elongation, %
AISI 304	500 – 700	190	40 – 60
AISI 347	510 – 740	205	40 – 60

Concerning the heat affected zone of both test materials, a strong increase in the yield strength and a decrease in the uniform elongation were observed with respect to the base material, at both testing temperatures. These results can be due to the different microstructures exhibited by the base materials and heat affected zone, as it will be discussed in § 4.3.

4.2.2 Irradiated materials

The effects of irradiation on the mechanical properties of the various materials are investigated by comparing the values obtained for the unirradiated materials with those obtained for the irradiated ones. Figures 4.17 – 4.20 summarise the results of tensile testing at both testing temperatures of irradiated AISI 304 and AISI 347 and compare them with those obtained for the unirradiated materials, as a function of the distance from the fusion line. A strong increase in the yield strength, due to irradiation, is observed at room temperature for both materials, whatever the distance from the fusion line (Figure 4.17). The increase in yield strength is less marked at high temperature as compared to the room temperature values (Figure 4.19). the change in yield strength clearly increases with the irradiation dose, at least for AISI 347.

A strong decrease in the uniform elongation after irradiation is observed for both materials, whatever the distance from the fusion line and the testing temperature. The change in uniform elongation apparently increases with the irradiation dose, at least for the AISI 304 tested at room temperature. No significant difference can be seen between the two irradiation doses of 0.3 and 1 dpa. It must be noted that the two investigated doses of 0.3 and 1 dpa are very close to each other. In Figures 4.17.a and 4.18.a the yield strength and uniform elongation values found in the literature [65, 92] for AISI 304 irradiated base materials tested at room temperature have been also reported. It can be seen that the yield strength of the irradiated heat affected zone presents higher values as compared to the irradiated base material, while the uniform elongation of the base material is higher.

a)   b)
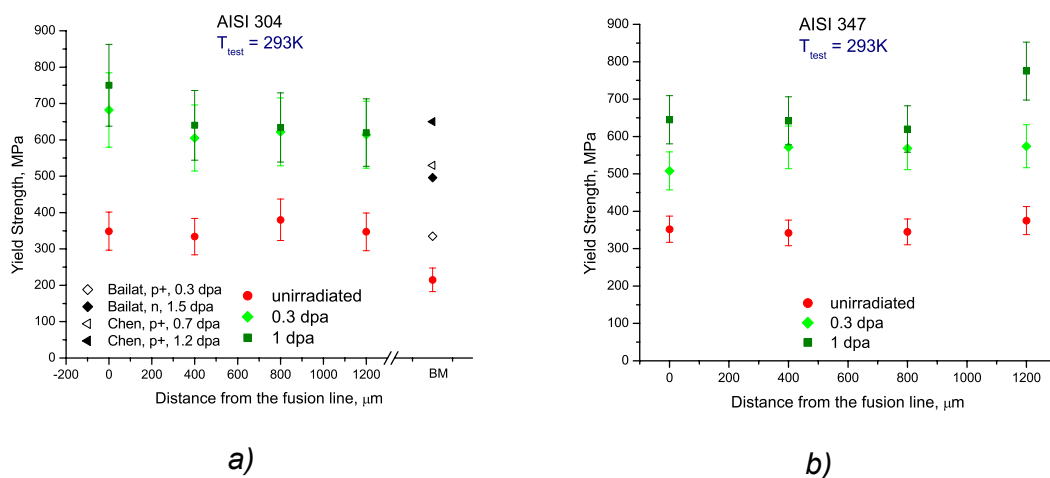
Figure 4.17. Yield strength dependence on the irradiation dose and the distance from the fusion line at room temperature for a) AISI 304 and b) AISI 347.

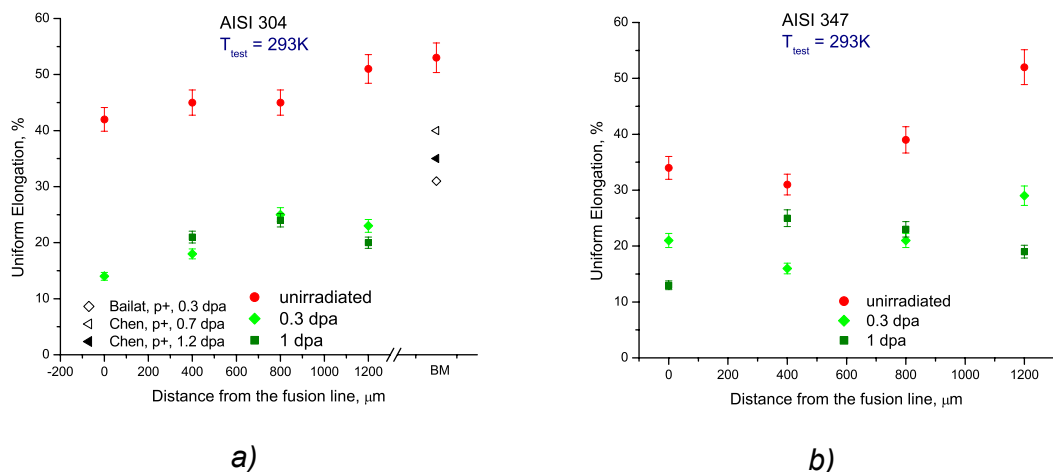a)   b)

Figure 4.18. Uniform elongation dependence on the irradiation dose and the distance from the fusion line at room temperature for a) AISI 304 and b) AISI 347.
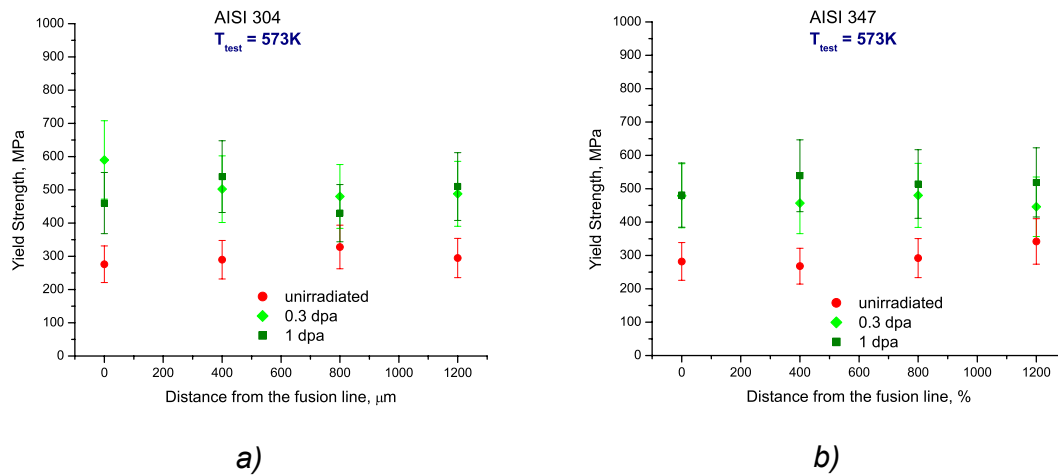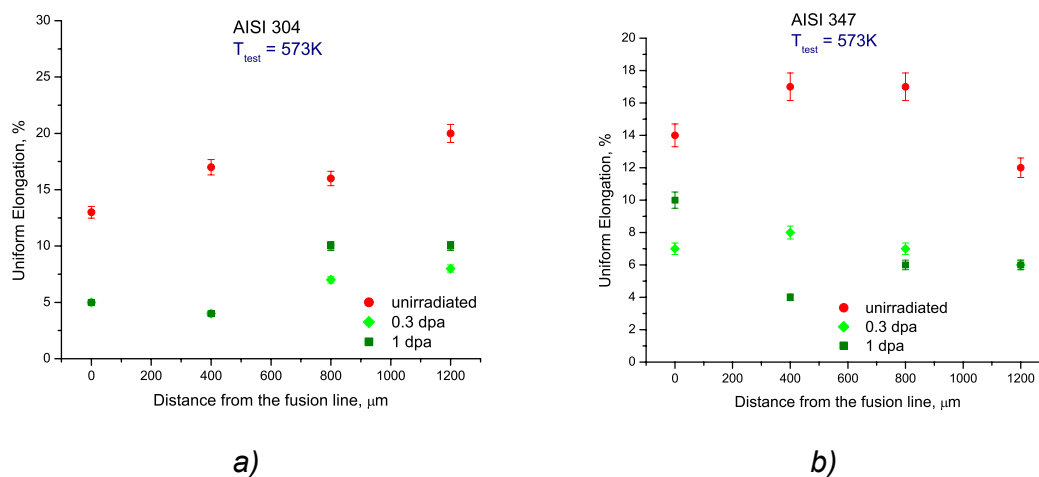
a)   *b)*

Figure 4.19. Yield strength dependence on the irradiation dose and the distance from the fusion line at high temperature for a) AISI 304 and b) AISI 347.

a)   *b)*

Figure 4.20. Uniform elongation dependence on the irradiation dose and the distance from the fusion line at high temperature for a) AISI 304 and b) AISI 347.

The radiation hardening is defined as the increase in yield strength of the irradiated materials as compared to the unirradiated ones, and it is plotted in Figure 4.21 for AISI 304 and AISI 347 tested at room temperature, together with the data found in the literature, as in Figures 4.17.a and 4.18.a. The radiation hardening is observed to be smaller in the heat affected zone as compared to the literature data for the base materials. The lower value from Bailat study on 0.3 dpa proton irradiated AISI 304 base material could be due to different irradiation or tensile testing conditions.

The loss of ductility is defined as the decrease of uniform elongation of the irradiated materials as compared to the unirradiated materials, and it is reported in Figure 4.22 for AISI 304 and AISI 347 tested at room temperature. In the case of AISI 347 the data are more scattered (Figure 4.22.b). The loss of ductility is observed to be higher in the irradiated heat affected zones as compared to the irradiated base materials (Figure 4.22.a).

132

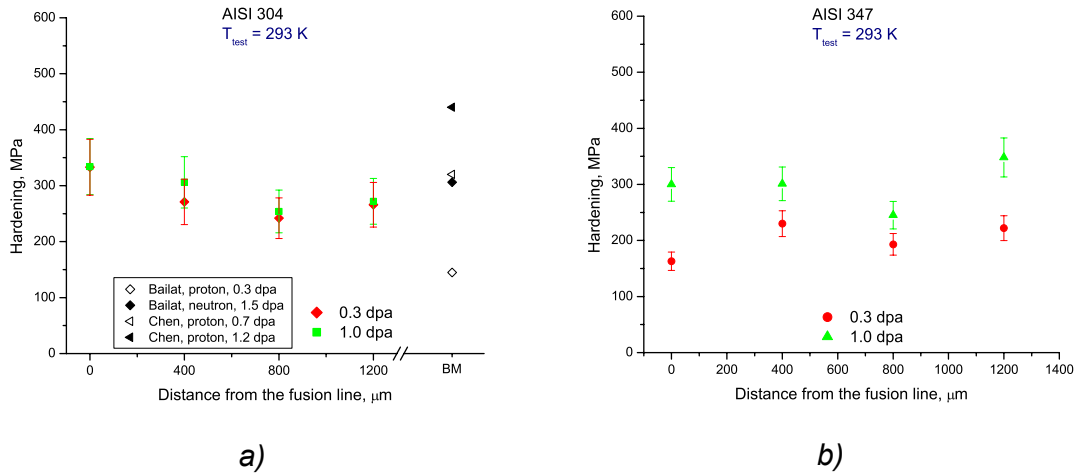*a)*   *b)*

Figure 4.21. Radiation hardening at 0.3 and 1 dpa as a function of the distance from the fusion line for a) AISI 304 and b) AISI 347 tested at room temperature.

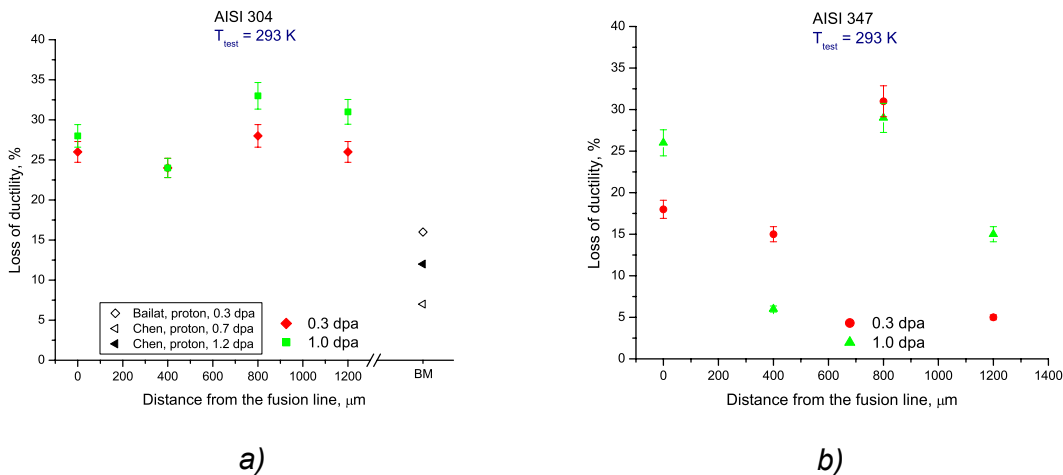*a)*   *b)*

Figure 4.22. Loss of ductility at 0.3 and 1 dpa as a function of the distance from the fusion line for a) AISI 304 and b) AISI 347 tested at room temperature.

From Figures 4.17 – 4.22 it can be concluded that heat affected zone presents a better resistance to irradiation than the base material, certainly due to the different original microstructure of the heat affected zone with respect to the base material in terms of a different microchemistry, a larger grain size, a higher dislocation density and the presence of ferrite interphase.

Similar behaviour was observed for the BR-3, AISI 304 in-service material. Figures 4.23 and 4.24 show the yield strength and uniform elongation variations with the irradiation dose and the distance from the fusion line in the case of the in-service material. The yield strength presents higher values in the heat affected zone as compared to the base material as both deformation temperatures. The uniform elongation values are lower in the heat affected zone as compared to the base material at both deformation temperatures. In the same time, the yield strength and uniform elongation show lower values at high temperature. Hardening and loss of

133

ductility are observed for both material states (base material and heat affected zone), at both testing temperatures. Hardening is more important at high temperature, while loss of ductility is more significant at room temperature. In these plots it is also be seen that hardening and loss of ductility are quite the same for the heat affected zone and base material, at both testing temperatures.

The values found in the literature for the yield strength and uniform elongation of different irradiated austenitic stainless steels [44, 65] are plotted in Figures 4.25 and 4.26, respectively. The data obtained in the present study for the different materials are also included in the figures. They are in good agreement with the literature data. Note that the yield strength and uniform elongation seem to saturate at about 700 MPa and at about 10 % respectively, from a dose of about 1 dpa.
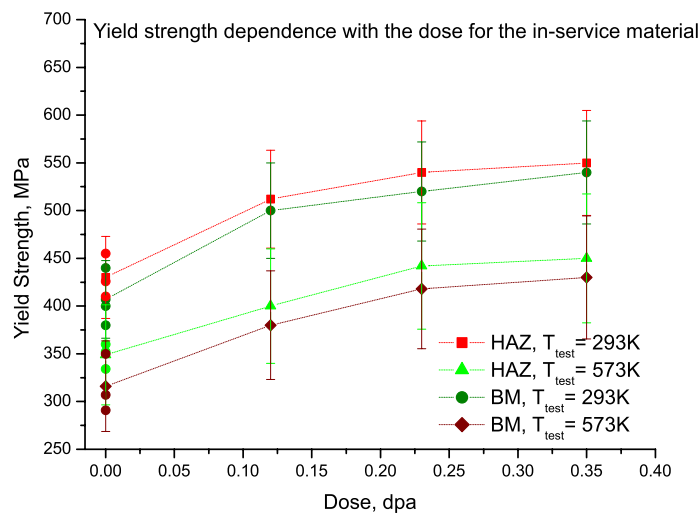
Figure 4.23. Yield strength dependence on the irradiation dose for the BR-304 in-service material, base material and heat affected zone, at both testing temperatures.
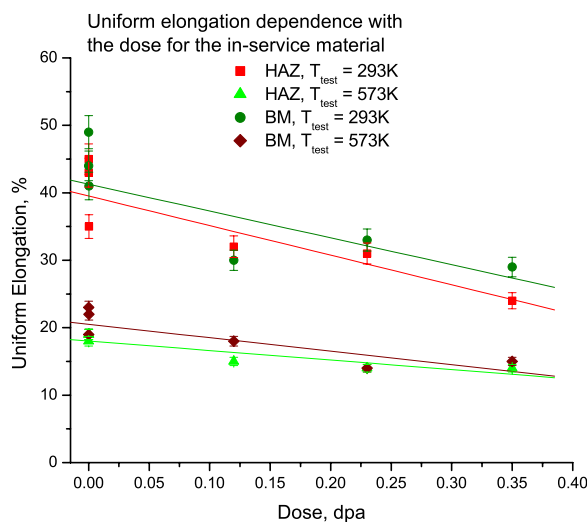

Figure 4.24. Uniform elongation dependence on the irradiation dose for the BR-304 in-service material, base material and heat affected zone, at both testing temperatures.
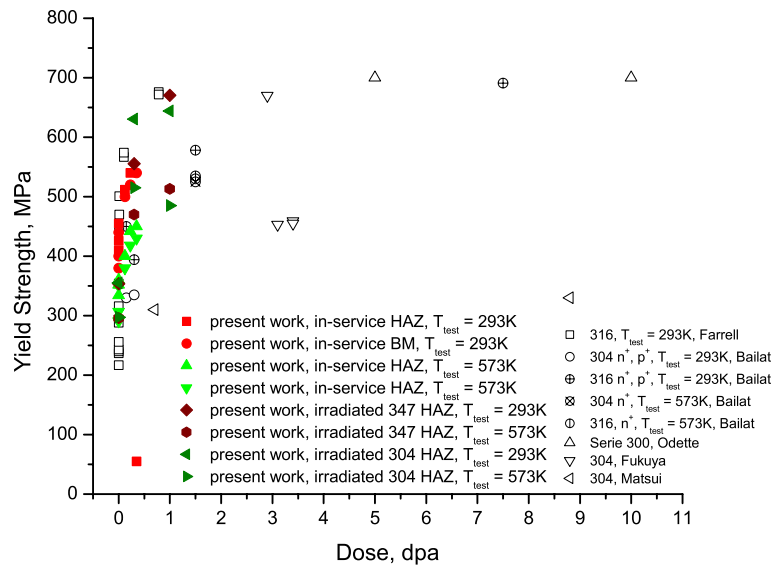
Figure 4.25. Yield strength dependence on the irradiation dose; comparison with the literature data (the irradiation temperature in the present study was about 300 °C).
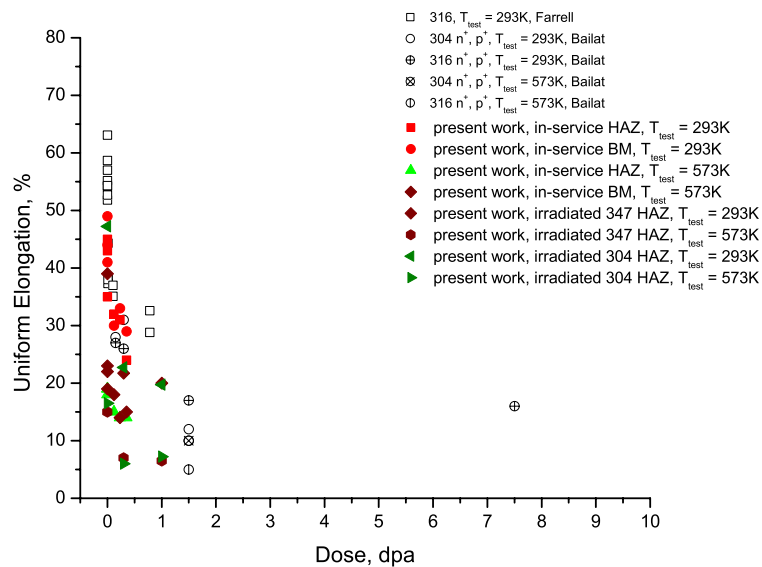

Figure 4.26. Uniform elongation dependence on the irradiation dose; comparison with the literature data (the irradiation temperature in the present study was about 300 °C).

The difference between the mechanical properties of unirradiated and neutron irradiated materials is attributed to the irradiation-induced changes in the microstructure, as it will be discussed in the next chapter.

4.3 Correlation between mechanical properties and microstructure

4.3.1 Unirradiated materials

One of the contributions to the strength of a material is the dislocation-dislocation interaction. As the dislocation density in the heat-affected zones is higher than in the base materials, one may expect that the heat affected zones are harder than the base materials. The following model can be used to determine the dislocation contribution to the yield strength [93]:

$$\sigma_d = M \cdot \alpha \cdot \mu \cdot b \cdot \sqrt{\rho} \qquad\qquad (4.3)$$

where M is the Taylor factor that relates to the shear stresses in a slip plane of a single crystal to the tensile stresses necessary to activate slip in a polycrystalline material, equal to 3.06 for fcc materials [66], α is a value that characterises the obstacle strength, taken equal to 0.2 [42], μ is the shear modulus, equal to 76.92 GPa for AISI 304 and 74.23 GPa for AISI 347, according to Table 2.5, b is the modulus of the Burgers vector of the gliding dislocations and ρ is the dislocation density. The dislocations in a fcc structure have a Burgers vector of the type $(a_0/2)\langle110\rangle$ [61]. The lattice parameter a_0 was determined from the diffraction patterns taken in TEM to be 0.364 nm for AISI 304 and 0.359 nm for AISI 347, which gives a Burgers vector modulus equal to 0.257 nm and 0.253 nm, respectively. For the in-service material, the shear modulus is 76.92 GPa, the lattice parameter 0.368 nm and the Burgers vector modulus 0.26 nm.

The yield strength due to dislocation-dislocation interaction was calculated with formula 4.5 and the results are reported in Figures 4.27 and 4.28 for AISI 304 and AISI 347 respectively, as a function of the distance from the fusion line. The corresponding experimental values are also included in the graphs. It can be seen that the calculated yield strength follows the same trend as the dislocation density variation (Figure 3.44). Differences exist between the experimental values and the calculated ones. These differences can be attributed to the presence of other features, apart from dislocations, contributing to the yield strength. One contribution could come from a change in the chemical composition of the heat affected zone due to heating during welding. The grain size is slightly higher in the heat affected zone with respect to the base material, which should yield a decrease in the yield strength of the heat affected zone with respect to that of the base material. According to the Hall-Petch relation the variation of yield strength σ_y with grain size is [105]:

$$\sigma_y = \sigma_0 + k_y \cdot d^{-1/2} \qquad\qquad (4.4)$$

where σ_0 is the friction stress (or the yield stress of a single crystal) and k_y is a constant dependent on the material.

Another effect could come from the presence of the ferrite in the austenite matrix. The amount of residual ferrite in the heat-affected zone is anyway very small (3 %).

The variation of the ferrite-austenite ratio in welded duplex stainless steels was found to have no significant influence on the hardness [103].
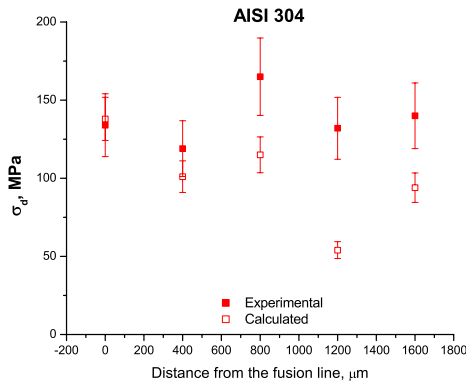

Figure 4.27. Yield strength due to dislocations as a function of the distance from the fusion line for AISI 304 tested at 273 K.
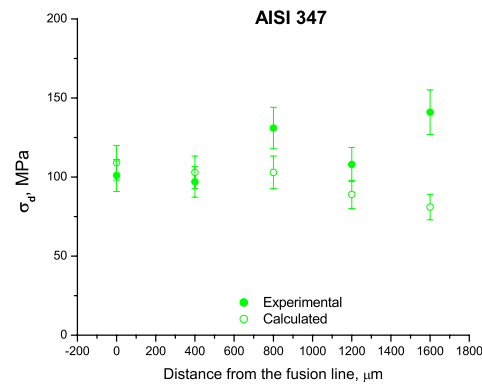
Figure 4.28. Yield strength due to dislocations as a function of the distance from the fusion line for AISI 347 tested at 273 K.

4.3.2 Irradiated materials

The changes in mechanical properties of irradiated materials with respect to those of unirradiated ones are a direct consequence of the damage microstructure. Different models have been developed to understand the mechanical behaviour of irradiated materials from the microstructure evolution under irradiation. The dispersed barrier hardening model describes the increase in yield strength which is necessary in an irradiated material to move a dislocation through a field of irradiation-induced obstacles. The yield strength increase, or radiation hardening, defined as the difference between the yield strength of the irradiated material and that of the unirradiated one, is given by [42]:

$$\Delta\sigma_y = M \cdot \alpha \cdot \mu \cdot b \cdot \sqrt{N \cdot d} \qquad\qquad (4.5)$$

where M is the Taylor factor, α is a value that characterises the obstacle strength, μ is the shear modulus, b is the modulus of the Burgers vector of the gliding dislocations (of the $(a_0/2)\langle 110 \rangle$ type in fcc crystals [61]), N is the number density and d is the mean size of the obstacles. The values of M, μ, b are as reported in § 4.3.1 and the values of N and d in Table 3.17. The total number density and size of the defects, calculated using the data reported in Table 3.17, are listed in Table 4.2. The measured mean distance between obstacles L = (N·d)$^{-1/2}$ is also reported in Table 4.2. As expected, this parameter decreases as the irradiation dose increases.

The obstacle strength, α, values range usually between 0.1 and 1, depending on the barrier type [28, 42, 65, 66, 82]. For weak obstacles, such as small loops and

clusters, a value of 0.2 is usually used for α, while for intermediate obstacles, such as Frank loops, $\alpha = 0.33 - 0.4$ [82].

According to the literature, to determine the value of the obstacle strength, α, the radiation hardening $\Delta\sigma_y$, as determined experimentally, is plotted as a function of $\sqrt{N \cdot d}$. By fitting the data with a straight line going through the origin (by definition the radiation hardening is zero for unirradiated materials), the value of α can be estimated from its slope, m, as [81]:

$$\alpha = \frac{m}{M \cdot \mu \cdot b} \qquad\qquad (4.6)$$

In the present study, the average between the yield strength values measured at room temperature for the four specimens along the fusion line was calculated, and the radiation hardening was determined using this value. In Figures 4.29 and 4.30 the radiation hardening is plotted against $\sqrt{N \cdot d}$ for AISI 304 and AISI 347, respectively, irradiated at 300°C to 0.3 and 1 dpa.

The resulting α values, calculated using Formula 4.6 and Figures 4.29 and 4.30, are listed in Table 4.2 for both irradiated test materials. The α values determined experimentally are small as compared to the literature ones.
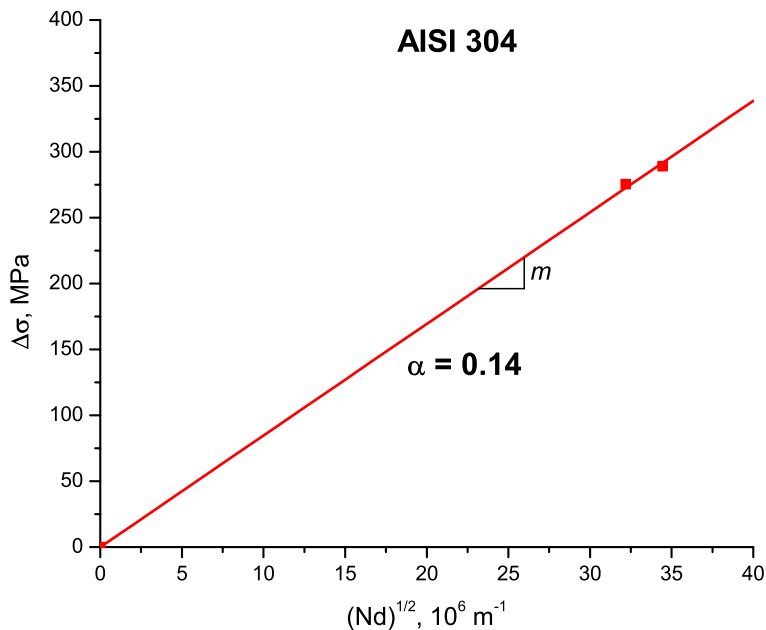

Figure 4.29. Radiation hardening versus the square root of the product of the defect cluster density and their mean size for AISI 304 test material irradiated at 300°C to doses of 0.3 and 1 dpa.
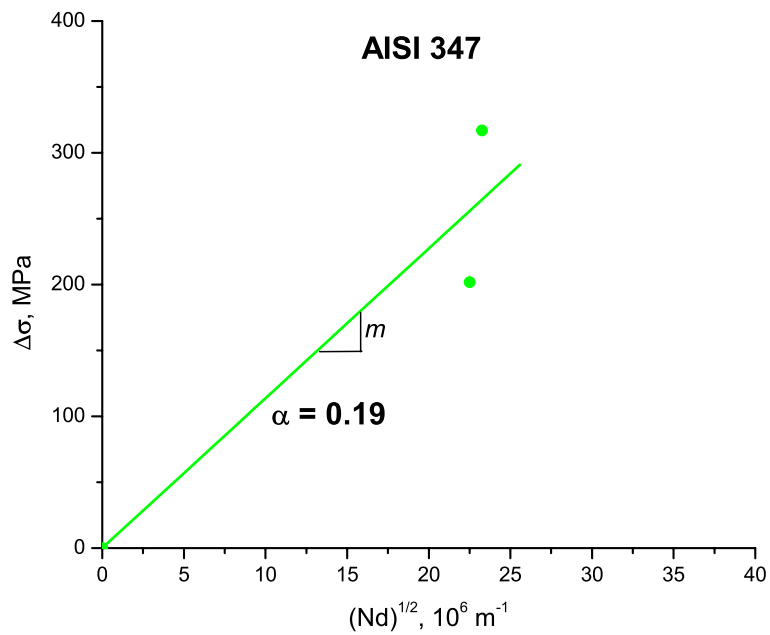
Figure 4.30. Radiation hardening versus the square root of the product of the defect cluster density and their mean size for AISI 347 test material irradiated at 300°C to doses of 0.3 and 1 dpa.

Table 4.2. Calculated irradiation-induced obstacle strength values for the irradiated test materials irradiated at 300°C to 0.3 and 1 dpa.

Material	Dose	N, m^{-3}	d, nm	L = (N·d)$^{-1/2}$, nm	α
AISI 304	0.3 dpa	1.2×10^{23}	2.2	31	0.14
	1 dpa	1.4×10^{23}	2.3	29	
AISI 347	0.3 dpa	1.6×10^{23}	5.4	44	0.19
	1 dpa	1.5×10^{23}	5.7	42	

Generally, the contributions from different defect types are combined according to a superposition law and the total change in yield strength can be calculated as [42]:

$$\Delta\sigma_{tot} = \sqrt{\sum_i \left(\Delta\sigma_{SR,i}\right)^2} + \Delta\sigma_{LR} \qquad\qquad (4.7)$$

where $\Delta\sigma_{SR}$ is related to short range obstacles such as black dots and Frank loops and $\Delta\sigma_{LR}$ to long range obstacles such as network dislocations.

In the present study, no specific investigation of the network dislocation was made after irradiation. It is also not possible to separate the specific contributions from the different types of defects (black dots, Frank loops) to the radiation hardening, as the contribution of each type of defects is unknown.

The radiation hardening has been then calculated using Formula (4.5) and the α values from Table 4.2. The results are listed in Table 4.3 together with the experimental radiation hardening values, for comparison. A very large difference is observed between the experimental values and the calculated ones, at least for 1.0 dpa irradiated materials. Two assumptions can be made to understand this difference.

First, one may try to take into account the different defect types influencing the mechanical properties. In this context, the total change in yield strength has been calculated using Formula 4.7, by separating the contributions from black dots and Frank loops, and testing different α values for both black dots and Frank loops. The results are listed in Table 4.4. It seems that the best correspondence to the experimental yield strength values obtained for obstacle strengths of 0.1 for black dots and 0.15 for Frank loops in the case of AISI 304 and for obstacle strengths of 0.09 for black dots and 0.2 for Frank loops in the case of AISI 347.

Second, one may assume that other irradiation-induced features, apart from black dots and Frank loops, contribute to radiation hardening.

Then, the difference between the calculated and experimental results could be due to a different radiation hardening behaviour occurring at low doses. It is assumed that small clusters, which can not be detected by TEM, co-exist together with the observable irradiation-induced defects at small irradiation doses. One may assume that the non-observable defects have a different strength (α) than the visible ones and the lineal fit going through the origin then exhibits a different slope at low doses. The contributions to radiation hardening due to the invisible and visible defects are schematically shown in Figure 4.31, assuming that the contributions from each type of defects are combined in the form of [42]:

$$\Delta\sigma_{tot} = \sqrt{\Delta\sigma_{inv}^2 + \Delta\sigma_{vis}^2} \qquad\qquad (4.8)$$

where $\Delta\sigma_{tot}$ is the total radiation hardening, $\Delta\sigma_{inv}$ is the hardening due to invisible defects and $\Delta\sigma_{vis}$ is due to the visible defects.

On the basis of this idea, it can be seen that the radiation hardening increases more slowly at low doses, when the number density and size of the invisible defects increases. After reaching a critical dose, the number density and size of the invisible defects should become constant, as they become suddenly visible, while new small, invisible defects are created. The radiation hardening due to the visible defects then

superimposes with the radiation hardening produced by the invisible defects from the critical dose.

Table 4.3. Experimental and calculated radiation hardening values using
fit-determined α values for the test materials irradiated at 300°C to 0.3 and 1 dpa.

Material	Dose	Experimental $\Delta\sigma_y$, MPa	Calculated $\Delta\sigma_y$, MPa
AISI 304 $\alpha = 0.14$	0.3 dpa	275.50	272.62
	1.0 dpa	289.00	133.71
AISI 347 $\alpha = 0.19$	0.3 dpa	201.75	245.85
	1.0 dpa	317.00	254.06

Table 4.4. Calculated radiation hardening values using different α values for black
dots and Frank loops for the test materials irradiated at 300°C to 0.3 and 1 dpa.

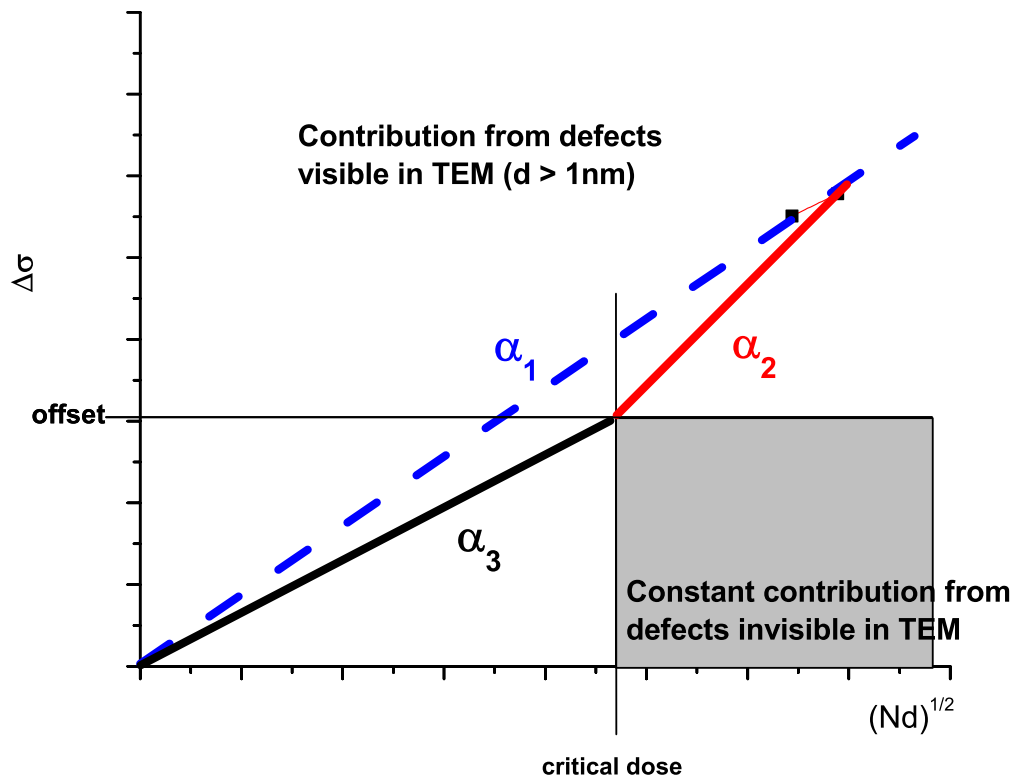| Dose	$\Delta\sigma_{tot}$, MPa	
	AISI 304	AISI 347
α = 0.1 for black dots and α = 0.2 for Frank loops		
0.3 dpa	368.94	247.95
1.0 dpa	370.03	283.90
α = 0.1 for black dots and α = 0.1 for Frank loops		
0.3 dpa	203.16	134.91
1.0 dpa	207.53	147.84
α = 0.09 for black dots and α = 0.2 for Frank loops		
0.3 dpa	366.45	246.49
1.0 dpa	367.00	283.13
α = 0.1 for black dots and α = 0.15 for Frank loops		
0.3 dpa	284.24	190.35
1.0 dpa	286.66	215.25

Figure 4.31. Schematic representation of the contribution to the radiation hardening due to the visible and invisible defects.

4.4 The INTERWELD Project

4.4.1 Residual stress measurements

The residual stresses induced by the welding process have been measured on the unirradiated and irradiated materials, using destructive (the ring-core technique) and non-destructive (neutron and X-ray diffraction) methods. Unirradiated welded plates were examined by FRAMATOME ANP using the ring-core technique, to determine the depth profiles of the local weld residual stresses, and the X-ray diffraction method. In PSI the neutron diffraction technique has been applied, using the POLDI (Pulse Over-Lap Diffraction) facility.

It was found that residual stresses are present in large welded pieces up to about 10 mm away from the weld centre, even the heat affected zone was approximated to 600 µm from the metallographic observations It was also found that weld residual stresses should be actually fully relaxed in the small specimens destined to tensile testing. This result indicates that the larger yield strength of the heat affected zone with respect to the yield strength of the base material, as measured in the present study, does not result from the presence of residual stresses in the heat affected zone. As mentioned before, such behaviour could arise from the higher dislocation density evidenced in the heat affected zone (produced by the residual stresses originally present in the welded materials), and/or the larger grain size in the heat affected zone, and/or a change in the chemical composition of the heat affected zone upon welding, and/or to the presence of the bcc ferritic phase in the heat affected zone.

4.4.2 Slow Strain Rate Tensile Tests

In order to evaluate the susceptibility of the welded test materials to stress corrosion cracking, SSRT tests have been performed on both unirradiated and 0.3 dpa irradiated test weld materials in CIEMAT. SSRT tests have been also performed on the in-service material in SCK-CEN.

The yield strength values obtained from the tensile tests performed the present study and the from SSRT tests performed in CIEMAT and SCK-CEN, have been plotted in Figure 4.32, as a function of the irradiation dose, together with the literature data [27]. A good agreement is observed between the results obtained either by tensile testing or SSRT tests and the literature data.
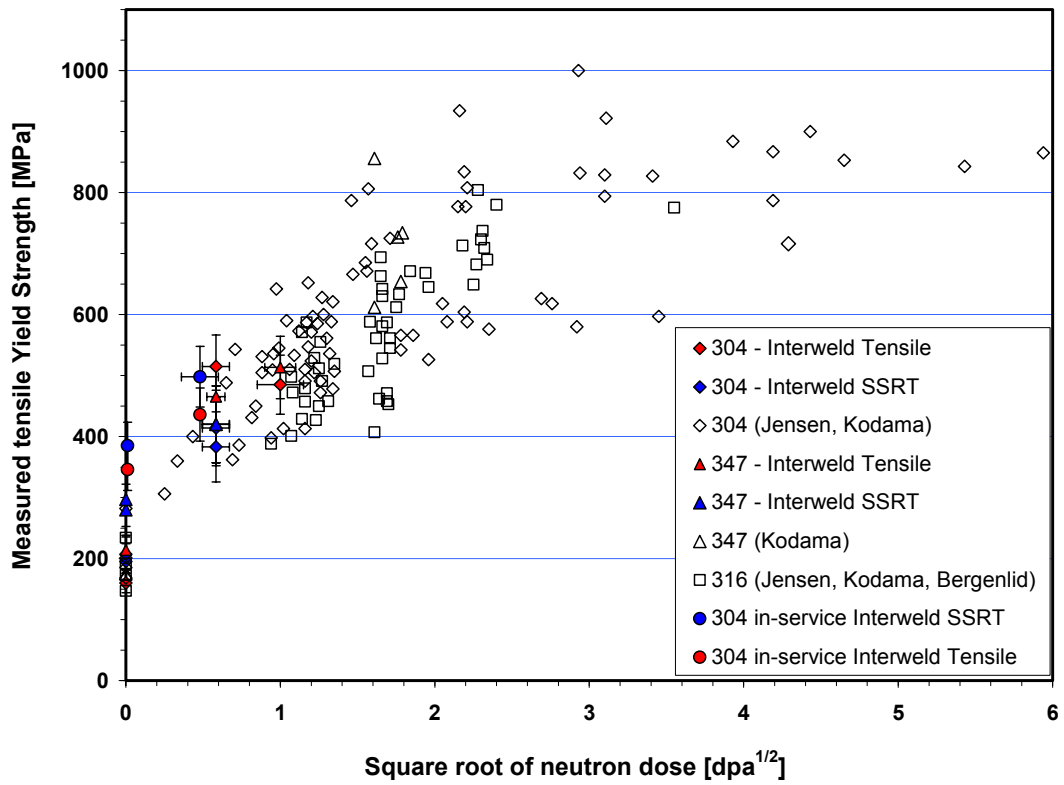
Figure 4.32. Yield strength as a function of dose in the case of neutron-irradiated austenitic stainless steels [27].

Conclusions

In metals and alloys subjected to irradiation, microchemical and microstructural changes may occur. The consequence of these modifications is an eventual alteration of their physical and mechanical properties.

Within this thesis, the effects of neutron irradiation on the microstructure and mechanical properties of welded joints made of austenitic stainless steels have been investigated. The materials were AISI 304 and AISI 347 welded by fusion welding process and irradiated with neutrons at 300°C to 0.3 and 1.0 dpa. An AISI 304 type from a decommissioned water reactor (in-service material), which had accumulated a maximum dose of 0.3 dpa at about 300°C, was also available. Studies of the mechanical properties and the microstructure of heat affected zones and base materials have been performed before and after irradiation.

Optical microscopy observations have shown that:
  - The grain size is significantly larger in the HAZ then in the BM.
  - The HAZ extends over around 600 µm on each side of the welded metal.

Tensile tests performed at 293 K and 573 K have shown that:
  - The heat affected zones of all studied materials (AISI 304, AISI 347, and AISI 304 in-service material) show higher yield strength and lower uniform elongation as compared to the base materials, at both testing temperatures (293 K and 573 K).
  - Neutron irradiation induces hardening and loss of ductility in all materials, at both testing temperatures. Radiation hardening clearly increases with irradiation dose.
  - Radiation hardening presents lower values for the HAZ as compared to the BM.
  - The loss of ductility is larger for the HAZ with respect to the BM.
  - The mechanical properties measured in the present study agree well with the literature data.

From transmission electron microscopy observations the following results were obtained:
  - The HAZ is composed of an austenite matrix containing a small amount of ferrite (3 %), resulting from the high temperatures reached during the welding process.
  - In the unirradiated test materials (AISI 304 and AISI 347), as well as in the low dose (10^{-4} dpa) in-service material the dislocation density was found to be higher in the HAZ as compared to the BM, due to the thermal cycles upon welding.
  - Irradiation-induced defects are small black dots which cannot be identified in TEM and Frank loops which can be of vacancy or interstitial type. No stacking fault tetrahedra were observed.
  - No irradiation-induced defects have been observed by TEM in the bcc ferrite present in the HAZ.
  - In the in-service material, the irradiation-induced defect density was found to be higher in the HAZ as compared to the BM.
  - The total defect density seem to increase with the irradiation dose, at least for the in-service material.

- o The higher defect density in the HAZ may be due to the larger grain size in the HAZ as compared to the BM, leaving less sinks (e.g. grain boundaries) for irradiation-induced defects annihilation.

Investigation of the deformation modes revealed that:
- o In the unirradiated materials tested at room temperature, twinning is the dominating deformation mode, while at high temperature dislocation motion prevails. The deformation mode does not depend on the distance from the fusion line.
- o In irradiated materials the deformation microstructure consists of a large amount of twins and stacking faults, independently on the position from the fusion line, the deformation temperature and the dose.
- o Based on the presence of radiation-induced defects inside the twins, it was concluded that no defect free channels form in austenitic stainless steels under deformation, at least under the conditions investigated here.

Correlation between the microstructure and the mechanical properties was established using the barrier hardening model. It was found that:
- o The irradiation-induced defects observed in TEM (black dots and Frank loops) are weak obstacles, with an obstacle strength coefficient of 0.2.
- o Radiation hardening cannot be explained only by the presence of the irradiation-induced defects observed in TEM. Apparently, smaller defects, not resolvable in TEM, also contribute to radiation hardening.

A good agreement was found between the data obtained in the present study and the data obtained by the other partners of the Interweld project.

As a general conclusion, although the irradiated HAZ contains a higher density of irradiation-induced defects as compared to the base material, the hardening of the HAZ is smaller than that of BM, which indicates that the HAZ present a better resistance to irradiation with neutrons. It seems that the negative effects of the irradiation on the alteration of mechanical properties of the HAZ may be more or less counterbalanced by its original microstructure, induced by the welding process, and including changes in the chemical composition, the presence of ferrite islands and a high dislocation density.

Suggestion for further research

The understanding of austenitic stainless steels behaviour under light water reactors operating conditions is still not well understood. Studies of the microstructure and the mechanical properties after irradiation at more locations in the heat affected zone would be needed in order to better understand the effects of the welding process. For the analysis of the small irradiation-induced defects, not resolvable in TEM, positron annihilation measurements would be useful. More detailed analyses of the grain boundaries segregation in the heat affected zone would be necessary to improve the understanding of the irradiation-assisted stress corrosion cracking process.

Further studies at higher irradiation doses should also be performed to confirm the present results.

References

1. P. Scott, J. Nucl. Mater. 211 (1994) 101–122.

2. O. Wachter, G. Bruemmer, Nucl. Eng. Des. 168 (1997) 35–52.

3. E.A. Kenik, R.H. Jones, G.E.C. Bell, J. Nucl. Mater. 212–215 (1994) 52–59.

4. P.L. Andresen et al., 4th International Symposium on Environmental Degradation on Materials in Nuclear Power Systems – Water Reactors (1990).

5. S.M. Bruemmer, 10th International Conference Environmental Degradation of Materials in Nuclear Power Systems – Water Reactors (2001).

6. http://www.nrg-nl.com/extranet/interweld/index.html

7. http://www.britannica.com/

8. Enrico Fermi, Nobel lecture, 1938.

9. http://www.alumni.ca/~chiuw3w/energy.html

10. http://www.euronuclear.org

11. J. Beddoes, J. Gordon Parr, Introduction to stainless steels, Materials Park: The Materials Information Society, 1999.

12. P. Marshall, Austenitic stainless steels, London; New York: Elsevier, 1984.

13. L.H. Van Vlack, Elements of materials science, Reading, Massachusetts: Addison–Wesley, 1964.

14. http://www.arconweld.com

15. David LeRoy Olson, Welding, Brazing, and Soldering, ASM Handbook, 1993.

16. K. Masubuchi, Analysis of welded structures, Oxford: Pergamon Press, 1980.

17. Welding Handbook, American Welding Society, 1976.

18. J.W. Elmer, T.A. Palmer, W. Zhang, B. Wood, T. DebRoy, Acta Mater. 51 (2003) 3333-3349.

19. J. F. Lancaster, Metallurgy of Welding, Cambridge: Abington Publishing, 1999.

20. W. Schilling, H. Ullmaier, in Materials Science and Technology, editors: R.W. Cahn, P. Haasen, E.J. Kramer, 1994.

21. G.J. Diens, G.H. Vineyard, Radiation effects in solids, New York: Interscience Publishers, 1957.

22. M.W. Thompson, Defects and radiation damage in metals, Cambridge: University Press, 1969.

23. D.S. Billington, J.H. Crawford Jr, Radiation damage in solids, Princeton, New Jersey: Princeton University Press, 1961.

24. G.H. Kinchin, R.S. Pease, Rep. Prog. Phys. 18 (1955), 1-15.

25. M.J. Norgett, M.T. Robinson, I.M. Torrens, Nucl. Eng. Des. 33 (1975) 50-54.

26. .J. Zinkle, B.N. Singh, J. Nucl. Mater. 199 (1993), 173-191.

27. S.M. Bruemmer, E.P. Simonen, P.M. Scott, P.L. Andresen, G.S. Was, J.L. Nelson, J. Nucl. Mater. 274 (1999), 299-314.

28. S.J. Zinkle, Y. Matsukawa, J. Nucl. Mater. 329–333 (2004) 88-96.

29. T.S. Byun, K. Farrell, E.H. Lee, J.D. Hunn, L.K. Mansur, J. Nucl. Mater. 298 (2001) 269-279.

30. M. Victoria, N. Baluc, C. Bailat, Y. Dai, M.I. Luppo, R. Schäublin, B.N. Singh, J. Nucl. Mater. 276 (2000) 114-122.

31. J. Gan, G.S. Was, J. Nucl. Mater. 297 (2001) 161-175.

32. N. Hashimoto, S.J. Zinkle, A.F. Rowcliffe, J.P. Robertson, S. Jitsukawa, J. Nucl. Mater. 283–287 (2000) 528-534.

33. N. Yoshida, J. Nucl. Mater. 174 (1990) 220-228.

34. D.J. Edwards, E.P. Simonen, F.A. Garner, L.R. Greenwood, B.M. Oliver, S.M. Bruemmer, J. Nucler. Mater. 317 (2003) 32–45.

35. D.J. Edwards, E.P. Simonen, S.M. Bruemmer, J. Nucler. Mater. 317 (2003)13-31.

36. G.S. Was, J.D. Busby, T. Allen, E.A. Kenik, A. Jenssen, S.B. Bruemmer, J. Gan, A.D. Edwards, P.M. Scott, P.L. Andersen, J. Nucl. Mater. 300 (2002) 198-216.

37. H. Wiedersich, P.R. Okamoto, N.Q. Lam, J. Nucl. Mater. 83 (1979)

98-108.

38. J.E. Pawel, A.F. Rowcliffe, D.J. Alexander, M.L. Grossbeck, K. Shiba, J. Nucl. Mater. 233–237 (1996) 202-206.

39. J.L. Brimhall, J.I. Cole, S.M. Bruemmer, Scripta Metall. Mater. 30 (1994) 1473-1478.

40. T. Onchi, K. Dohi, N. Soneda, J.R. Cowan, R.J. Scowen, M.L. Castano, J. Nucl. Mater. 320 (2003) 194-208.

41. A.L. Bement Jr. Second International Conference on Strength of Metals and Alloys, American Society for Metals, Metals Park, OH, 1970, 693-728.

42. G.E. Lucas, J. Nucl. Mater. 206 (1993), 287 – 305.

43. J.T Busby, M.C. Hash, G.S. Was, J. Nucl. Mater. 336 (2005), 267-278.

44. K. Farrell, T.S. Byun, N. Hashimoto, J. Nucl. Mater. 335 (2004) 471-486.

45. O. Wachter, U. Wesseling, J. Bruns, R. Kilian, VGB – Konferenz, 1995.

46. P.L. Andresen, J. Nucl. Mater. 274 (1999) 299-314.

47. J.T. Busby, G.S. Was, E.A. Kenik, J. Nucl. Mater. 302 (2002), 20-40.

48. J. Sutcliffe, Small Specimen Tensile Testing, PSI report, TEM-43-01-11, 2001.

49. M.L. Jenkins, M.A. Kirk, Characterisation of radiation damage by transmission electron microscopy, Institute of Physics Publishing Bristol and Philadelphia, 2001.

50. P. Hirsch, A. Howie, R. Nicholson, D.W. Pashley, M.J. Whelan, Electron Microscopy of Thin Crystals, 1977.

51. J.H. Spence, J.M. Zuo, Electron Microdiffraction, New York and London: Plenum Press, 1992.

52. N. Baluc, Doctoral thesis, Lausanne, EPFL, 1990.

53. J. W. Edington, Monographs in practical electron microscopy in materials science, London, Basingstoke: Macmillan, 1975.

54. R. Schäublin, P. Stadelmann, Mat. Sci. Eng. A 164 (1993) 373-378.

55. J. P. Hirth, J. Lothe, Theory of Dislocations, New York: McGraw Hill, 1968.

56. A. K. Head, P. Humble, L. M. Clarebrough, A. J. Morton, C. T. Forwood, Computed Electron Micrographs and Defect Identification, Amsterdam: North-Holland 1973.

57. Yong-Moo Cheong, J. H. Kim, J. H. Hong, H. K. Yung, 15th World Conference on Non-Destructive Testing Conference, Rome 2000.

58. D.J. Kotecki, T.A. Siewert, Welding Journal 71 (1992), 171-s-178-s.

59. J.M. Vitek, S.A. David, C.R. Hinman, Welding Journal 82 (2003) 10-s-17-s.

60. Erich Folkhard, Welding Metallurgy of Stainless Steels, Springer-Verlag 1984.

61. D. Hull, D.J. Bacon, Introduction to dislocations, Pergamon Press Ltd 1984.

62. T.S. Byun, N. Hashimoto, K. Farrell, Acta Mater. 52 (2004) 3889-3899.

63. T.S. Byun, E.H. Lee, J.D. Hunn, J. Nucl. Mater. 321 (2003) 29-39.

64. T.S. Byun, Acta Mater. 51(2003) 3063-3071.

65. C. Bailat, Doctoral thesis, EPFL, 1999.

66. X. Jia, Doctoral thesis, EPFL, 2003.

67. S.J. Zinkle, N. Hashimoto, D.T. Holezer, A.L. Quallas, T. Muroga, B.N. Singh, J. Nucl. Mater. 307 –311 (2002) 192-196.

68. Y. Dai, Doctoral thesis, EPFL, 1995.

69. P. Maziasz, J. Nucl. Mater. 205 (1993) 118-145.

70. E.H. Lee, J.D. Hunn, T.S. Byun, L.K. Mansur, J. Nucl. Mater. 280 (2000) 18-24.

71. E.H. Lee, J.D. Hunn, N. Hashimoto, L.K. Mansur, J. Nucl. Mater. 278 (2000) 266-272.

72. N. Hashimoto, E. Wakai, J.P. Robertson, J. Nucl. Mater. 273 (1999) 95-101.

73. M. Horiki, M. Kiritani, J. Nucl. Mater. 212–215 (1994) 246.

74. G.S. Was, J.T. Busby, Philos. Mag. 85 (2005) 443-465.

75. S.G. Song, J.I. Cole, S.M. Bruemmer, Acta Mater. 45 (1997) 501-511.

76. T.S. Byun, Acta Mater. 51 (2003) 3063-3071.

77. E.H. Lee, T.S. Byun, J.D. Hunn, K. Farrell, L.K. Mansur, J. Nucl. Mater. 296 (2001) 183-191.

78. T.S. Byun, K. Farrell, Acta Mater. 52 (2004) 1597-1608.

79. E.H. Lee, T.S. Byun, J.D. Hunn, M.H. Yoo, K. Farrell, L.K. Mansur, Acta Mater. 49 (2001) 3269-3276.

80. M. Niewczas, G. Saada, Philos. Mag. A 82 (2002) 167-191.

81. N. Baluc, Y. Dai, M. Victoria, 20th Risø International Symposium on Materials Science, 1999, 245-251.

82. R. Schäublin, D. Gelles, M. Victoria, J. Nucl. Mater. 307-311 (2002) 197-202.

83. S.J. Zinkle, J. Nucl. Mater. 150 (1987) 140-158.

84. S.J. Zinkle, P.J. Maziasz, R.E. Stoller, J. Nucl. Mater. 206 (1993) 266-286.

85. S.J. Zinkle, R.I. Sindelar, J. Nucl. Mater, 155–157 (1988) 1196-1200.

86. J. Silcox, P.B. Hirsch, Philos. Mag. 4 (1959) 72-89.

87. Z. Yao, Doctoral thesis, EPFL, 2005.

88. S.J. Zinkle, A. Horsewell, B.N. Singh, W.F. Sommer, J. Nucl. Mater. 212–215 (1994) 132-138.

89. R. Schäublin, Z. Yao, N. Baluc, M. Victoria, Philos. Mag. 85 (2005) 769-777.

90. R.E. Schramm, R.P. Reed, Metall. Trans. A 6 A (1975) 1345-1349.

91. S.J, Zinkle, private communications.

92. J. Chen, Y. Dai, F. Carsughi, W.F. Sommer, G.S. Bauer, H. Ullmaier, J. Nucl. Mater. 275 (1999) 115-118.

93. Unified Constitutive laws of plastic deformation, edited by A.S. Krausz, K. Krausz, Academic Press Inc 1996.

94. G. Bouche, J.L. Bechade, M.H. Mathon, L. Allais, A.F. Gourgues, L. Naze, J. Nucl. Mater. 277 (2000) 91-98.

95. K. Nakata, S. Ikeda, S. Hamada, A. Hishinuma, J. Nucl. Mater. 233–237 (1996) 192-196.

96. H. Shaikh, G. George, F. Schneider, K. Mummert, H.S. Khatak, Mater. Corros. 51 (2000) 719-727.

97. T. Nagasaka, N.J. Heo, T. Muroga, A. Nishimura, H. Watanabe, M. Narui, K. Shinozaki, J. Nucl. Mater. 329–333 (2004) 1539-1543.

98. X. Jia, Y. Dai, J. Nucl. Mater., to be published.

99. G. Maussner, L. Scharf, R. Langer, B. Gurovich, Nucl. Eng. Des. 193 (1999) 359-376.

100. M. Horiki, S. Arai, Y. Satoh, M. Kiritani, J. Nucl. Mater. 255 (1998) 165-173.

101. M. Eldrup, B.N. Singh, J. Nucl. Mater. 276 (2000) 269-277.

102. M. Eldrup, B.N. Singh, Mater. Sci. Forum 363–365 (2001) 79-81.

103. V. Muthupandi, P. Bala Srinivasan, S.K. Seshadri, S. Sundaresan, Mater. Sci. Eng. A 358 (2003) 9-16.

104. http://cimesg1.epfl.ch/CIOL/ems.html

105. E.O. Hall, Proc. Phys. Soc. B 64 (1951) 747-753.

Acknowledgments

My friends have always been there for me and made my life easier in difficult moments. I would like to thank my friends from Romania for whom the distance didn't matter: Mihaela, Lorelai, Vali, Alina, Simona, Andrei, Sorin. Piotr gave me a lot of understanding and support in the difficult moments of writing the thesis. My tribute goes to the best friends somebody can have: Jonut, Maria, Paul. Besides, I would like to thank all the other PSI PhD students or non-students which helped me to have fun: Zeljka, Ana, Anja, Dwane, Antonino, Paolo, Stefano, Stefan, Ahed, Stela, Bas and many, many others.

Last, but not least, I would like to thank Christoph for always believing in me.

CURRICULUM VITAE

Raluca STOENESCU

Born on 25th August 1974 in Bucharest, Romania
Nationality: Romanian

1998	University Politehnica Bucharest, Romania
	Masters degree in mechanical engineering
1998 – 2001	University Politehnica Bucharest, Romania
	Teaching assistant
2001 – 2005	Paul Scherrer Institute, Switzerland
	PhD Student